Development of Glass-Ceramic Composites by One-Step Synthesis Methods

A Thesis submitted to the College of Graduate and Postdoctoral Studies

In Partial Fulfillment of the Requirements for the Degree of Master of Science

In the Department of Chemistry University of Saskatchewan Saskatoon

By

Giovanni Donato

Permission to Use

In presenting this thesis in partial fulfillment of the requirements for a degree of Master from the University of Saskatchewan, I agree that the Libraries of this University may make it freely available for inspection. I further agree that permission for copying of this thesis in any manner, in whole or in part, for scholarly purposes may be granted by the professor or professors who supervised my thesis work or, in their absence, by the Head of the Department or the Dean of the College in which my thesis work was done. It is understood that any copying or publication or use of this thesis or parts thereof for financial gain shall not be allowed without my written permission. It is also understood that due recognition shall be given to me and to the University of Saskatchewan in any scholarly use which may be made of any material in my thesis. Requests for permission to copy or to make other uses of materials in this thesis in whole or part should be addressed to:

Head of the Department of Chemistry

University of Saskatchewan

Saskatoon, Saskatchewan S7N 5C9

Canada

OR

Dean

College of Graduate and Postdoctoral Studies

University of Saskatchewan

105 Administration Place

Saskatoon, Saskatchewan S7N 5A2

Canada

Acknowledgements

I would like to start of by thanking my family Jaclyn, Ace, and Blackey who helped me push through the difficult times with their love and support. I would also like to thank my parents and brothers. Finally, I would like to thank Dr. Bryan Koivisto for showing me how enjoyable it can be to spend all day in a lab.

I would like to extend my deepest gratitude to my supervisor, Dr. Andrew Grosvenor for all his guidance, patience, support, and passion. His revisions and comments on written material were extremely helpful in crafting manuscripts, reports, and this thesis. My studies at the University would not have been the same without Andrew. I would like to thank my advisory committee, Dr. Tim Kelly for his insightful comments. I would like to thank all my group members past and present for their guidance, especially Dr. Jeremiah C. Beam. I would like to thank Derek Holzscherer for his help with the experimental work presented in Chapter 2. The XANES spectra presented in Chapters 2 and 3 were collected with the help from Dr. Jeremiah C. Beam, Dr. Xiaoxuan (Vince) Guo, Farah Mahmood, Sarah McCaughtery, Rahin Sifat, Arthur Situm, and Dr Andrew Grosvenor. This thesis and the manuscripts that were used for the purpose of this thesis was written by Giovanni Donato with editing assistance provided by Dr. Andrew Grosvenor.

I would like to thank Mr Tom Bonli for his help in collecting the electron microprobe results presented in Chapter 2 as well his assistance in collecting powder X-ray diffraction patterns. Dr Lucia Zuin and Dr David Wang from the VLS-PGM beamline at the CLS are thanked for their help collecting the XANES spectra presented in Chapters 2 and 3 of this thesis. Dr Zou Finfrock, Dr Mathew Ward, and Mr Michael Pape at the 20BM at CLS@APS are thanked for their support in carrying out XANES experiments presented in Chapters 2 and 3 of this thesis. Mr. Ivan Barker and Mr. Bradley Kobe from Surface Science Western, University of Western Ontario are thanked for collecting the SEM images and EDX maps presented in Chapter 3 of this thesis.

I would like to thank the funding agencies that provided the funds used in completing this thesis. Funding for this project was received from a discovery grant awarded to Dr. Andrew P. Grosvenor from the Natural Sciences and Engineering Research Council (NSERC) of Canada. I would like to thank the University of Saskatchewan for financial support. The Canadian Foundation for Innovation is thanked for providing the fund used to purchase the PANalytical Empyrean Powder X-ray Diffractometer used in Chapters 2 and 3 of this thesis. The CLS is

supported by NSERC, the National Research Council of Canada, the Canadian Institutes of Health Research, the Province of Saskatchewan, Western Economic Diversification Canada, and the University of Saskatchewan. Sector 20 (CLS@APS) facilities at the Advanced Photon Source are supported by the US Department of Energy – Basic Energy Sciences, the Canadian Light Source and its funding partners, and the Advanced Photon Source. Use of the Advanced Photon Source, an Office of Science User Facility operated for the U.S. Department of Energy (DOE) Office of Science by Argonne National Laboratory, was supported by the U.S. DOE under Contract No. DE-AC02-06CH11357.

Abstract

High level nuclear waste can potentially be separated from the environment using glass-ceramic composite materials. These materials are usually synthesized using a two-step synthesis method where the ceramic and glass phases are made separately followed by mixing and annealing to form the composite material. This thesis work aims to investigate possible one-step synthesis methods (using both dry and wet chemical methods) where all precursors are mixed together and annealed only once. Additionally, the crystallization behaviour of a Pu surrogate (Ce) was investigated under different annealing temperatures, ceramic loading in the composite material, and oxidation state of the Ce precursor. Rare-earth phosphate-borosilicate glass composites were synthesized for this work and the local and long-range order was investigated as well as the morphology. This was performed using powder X-ray diffraction, X-ray absorption near-edge spectroscopy, and electron microscopy along with energy dispersive X-ray spectroscopy.

It was observed that the long-range order and local chemical environment of both glass forming ions and ceramic forming ions is similar in the one-step ceramic method to the two-step ceramic method. The shape and size of the crystallites were different depending on synthesis method and was attributed to the mechanism in which the crystallites form. Differences in solubility of $LaPO_4$ and YPO_4 in borosilicate glass was observed and suggested to be caused by the difference in the structural roles of La^{3+} and Y^{3+}. The one-step solution-based method was found to possess differences compared to the one-step ceramic method. These differences include the temperature at which the glass partially crystallized, the size of the crystallites, and the ordering of the Si network in the glass. These changes were all suggested to be caused by the intimate mixing of precursors the solution-based method provides. Finally, Ce was found to potentially crystalize as $CePO_4$, CeO_2, or $Na_3Ce(PO_4)_2$. The crystal phases present were dependant on the annealing temperature, ceramic loading, and oxidation state of the Ce precursor. Higher ceramic loading and higher annealing temperature are among the synthesis conditions which favoured the formation of $CePO_4$.

Contents

List of Tables

List of Schemes

List of Figures

List of Abbreviations

a	Cation-oxygen bond distance
APS	Advanced Photon Source
AVH	Atelier de Vitrification de La Hague
B	Full width at half maximum
BG	Borosilicate glass
BSE	Back scattered electron
cal	Calorie
CANDU	Canada deuterium uranium
CLS	Canadian Light Source
CN	Coordination number
d	Interplanar spacing
D	Crystallite size
EDX	Energy Dispersive X-ray Spectroscopy
eV	Electron volt
EXAFS	Extended X-ray Absorption Fine Structure
FS	Field strength
I_0	Intensity of incident X-ray beam
I_t	Intensity of transmitted X-ray beam through the sample
I_{ref}	Intensity of transmitted X-ray beam through the reference
k	Shape factor
n	Principal quantum number
N	Average number of Si around B

nmr	Nuclear magnetic resonance
Pa	Pascal
PUREX	Plutonium uranium extraction
RE	Rare-earth
SEM	Scanning Electron Microscopy
SYNROC	Synthetic rock
t	Sample thickness
TEY	Total electron yield
TFY	Total fluorescence yield
VLS-PGM	Variable Line Spacing-Plane Grating Monochromator
XANES	X-ray Absorption Near-Edge Spectroscopy
XAS	X-ray Absorption Spectroscopy
XRD	X-ray Diffraction
Z	Charge of an ion
ε	Microstrain
μ	Absorption coefficient
2θ	the diffraction angle
λ	Wavelength of X-rays

Chapter 1 Introduction

1.1 Nuclear Energy and Waste

Nuclear power has been proposed as a partial alternative to fossil fuels in order to reach the world's electricity demands.[1] The electricity produced by nuclear power is relatively clean with limited greenhouse gases released in the production of the energy.[2,3] Canada currently produces ~15% of its electricity from nuclear power using reactors mostly located in Ontario.[4]

Nuclear energy requires radioactive isotopes to produce energy.[4] As such the waste produced by the nuclear energy cycle can be categorized based on the radioactivity of the waste.[5] Low-level waste has low levels of radioactivity and is contaminated equipment such as papers and used tools.[5] The radioactivity is mostly short lived.[5] Intermediate-level waste has higher radioactivity than low-level waste.[5] Intermediate-level waste can be resins or sludges as well as contaminated materials from the primary circuit of the reactor.[6] High-level waste is comprised of minor actinides and lanthanides as well as other fission products.[7–9] High-level waste is the smallest volume fraction of nuclear waste but contains the majority of the radioactivity.[1] As such, high-level waste needs to be removed from the environment for a long period of time.[9] Spent nuclear fuel is an example of high-level waste.[5]

The fuel used to produce nuclear energy is typically reliant on ^{235}U as a fissile isotope.[4] The fuel is enriched with this radioactive isotope before being made into the fuel material (typically UO_2).[4] In CANDU reactors little to no enrichment is required as the 0.7% natural abundance of ^{235}U can be used.[4] After the fuel has spent a prespecified amount of time (1-3 years) in the nuclear reactor it is removed and placed in wet storage for 5-10 years to help cool it and wait for some of the radioactivity to decrease.[5] This spent fuel, now considered nuclear waste, still contains ^{235}U but it also contains fission products and minor actinides.[5] The exact composition of this nuclear waste can change depending on the type of reactor or fuel source used.[9] Once the nuclear waste has cooled, it is either sent for reprocessing (in a closed nuclear fuel cycle) or sequestration (in an open nuclear cycle).[4]

When reprocessing the fuel, the leftover U and potentially Pu is collected in order to make more fuel material.[10] Plutonium uranium extraction (PUREX) is the most widely used reprocessing

method.[11] The PUREX method relies on a series of extractions using nitric acid and tributyl phosphate in an organic diluent for the aqueous and organic phases respectively.[11] Plutonium, uranium, and other metal ions which were dissolved by nitric acid are solvated by the phosphoryl groups of tributyl phosphate leading to these ions being present in the organic phase.[12]

After reprocessing (if it is performed), the waste stream is ready to be incorporated into a waste form. The AVH (Atelier de Vitrification de La Hague) process developed in France is an example of a method used to make a waste form.[1] This process uses glass as a waste form for non-separated nuclear waste.[1] In this process, powders of liquid high-level waste is obtained by evaporating the solvent at 500 ^{o}C.[1] This process produces oxides and nitrates of the waste elements.[1] Following this, the dry powder is mixed with a glass frit and melted at 1150 ^{o}C.[1] The melted glass is then poured into a stainless-steel canister and sealed[1]. This canister can then be placed in a geological repository.[1]

1.2 Nuclear Waste Forms

A proposed method to sequester nuclear waste involves incorporating the waste elements into a waste form, placing the waste form in a canister, and placing the canister deep underground in a geological repository.[1,9,13] Prior to incorporation of the waste elements into a waste form, the waste stream can also be separated in order to use waste forms that are optimized for certain elements such as Cs or the rare-earths and actinides.[1] Glasses, ceramics, and glass-ceramic composites have been proposed to sequester high level nuclear waste.[2,14–16]

Glasses are able to incorporate a large variety of elements into the amorphous structure characteristic of a glass.[2] Being an amorphous material, glass lacks long-range order and is not thermodynamically stable.[17] The amorphous network is composed of network forming ions linked together through bridging oxygen ions.[1,18] Typically, network forming cations have low coordination numbers (3-4) and are only connected at corners of the network former-oxygen polyhedra.[1,18] The 3D network of network forming cations can be broken up by the introduction of non-bridging oxygen anions.[1,18] Non-bridging oxygen anions do not link network formers together and are created through the introduction of network modifiers.[1,18] Network modifiers have higher coordination numbers and ionically bond to O^{2-}.[1,18] It is worth noting that while the coordination number of network formers and modifiers can change, the O^{2-}, whether bridging or non-bridging, must have a maximum coordination number of two.[18] A third type of cation can

exist in glass which is called a network intermediate.[1,18] These cations can behave as a network former or as a network modifier depending on the glass composition.[1,18] High-level nuclear waste elements are typically network modifiers or intermediates due to their large size.[1]

The main advantage of using glass as a waste form is that the glass can accommodate the entire composition of the waste stream to some degree.[2] Another advantage is that glass has been made in industry for decades and as such a large knowledge base is available for this technology.[1] Despite these advantages, glass can only accommodate a few weight % of minor actinides present in high-level waste and crystallization can mean failure for this waste form.[19,20] Crystalline SiO_2 undergoes phase changes at relatively low temperatures (270 ^oC) which is accompanied by a change in volume.[19,21,20] This can cause swelling and cracking as well as change the composition of the residual glass.[19,20] The volatility of the glass melt must also be considered and be suppressed as much as possible when making a glass.[1]

Ceramics are non-metallic, non-molecular, inorganic solids.[22] They are crystalline materials made up of a lattice of atoms/ions and are either thermodynamically stable or metastable.[1] These materials possess long-range order that comes from the arrangement of the elements in a repeating crystal structure.[7] The long-range order of ceramics is dependent on the size and charge of the elements present.[23] As such, crystal structures can only accommodate elements that meet those requirements.[23]

Ceramics as a waste form have a much higher waste loading ability than glasses, but they are limited in the variety of waste elements that can be incorporated.[23] The higher waste loading ability of ceramics is due to the higher thermal stability and density of ceramics when compared to glass as well as being able to incorporate the waste elements into specific crystallographic sites that can accommodate the large waste elements.[24] Waste forms such as SYNROC (synthetic rock) which contain multiple ceramic phases are being developed to overcome the limitation of the waste elements that can be incorporated.[25] Multiphase ceramic waste forms contain a larger variety of crystallographic sites with different charge and size restrictions than single phase ceramics.[25] This allows for more of the waste stream elements to be sequestered.[25] The higher thermal stability and waste loading also decreases the cost associated with placing the waste in a deep geological repository since the volume of the waste form that needs to be stored decreases.[24] The processing

conditions of ceramic waste forms are not as simple as glass processing since they can involve multiple cycles of grinding and annealing.[26]

Glass-ceramic composite materials contain ceramic crystallites dispersed in a glass matrix.[27] Glass-ceramic composites are able to capitalize on the strengths of pure glass and ceramics.[2,28] The large waste elements (such as actinides) can be incorporated into the ceramic crystallites giving the waste form a high waste loading capacity and allows the glass to act as a secondary barrier.[2,9,29] Smaller waste elements that have a higher solubility in glass can also be incorporated directly into the glass.[2,9,29] Additionally, glass-ceramic composites can be made using glass producing technology.[30] Glass-ceramic composite materials represent a relatively simple to produce waste form that has high waste loading of non-separated high-level waste as well as possessing improved mechanical properties when compared to glass alone.[31,32]

1.3 Introduction to Glass-Ceramic composites

Glass-ceramic composites are heterogenous materials that consist of ceramic crystallites dispersed in a glass matrix.[27] By synthesizing a material that contains both crystalline ceramic and amorphous glass, the final material can possess properties that are greater than the sum of its parts.[31,32] This class of materials was serendipitously discovered by Stookey in 1957.[33] Stookey, who worked for Corning Glass Works, accidentally annealed a piece of Li_2O-SiO_2 glass at a temperature that was 300 ^oC higher than intended.[34] This caused lithium disilicate crystallites to form within the glass and the material became a glass-ceramic composite.[35] The glass-ceramic composite material that was accidentally synthesized by Stookey was investigated and developed into the commercial product Pyroceram.[34] Ceramic crystallites formed within the glass in a controlled manner and resulted in the formation of the glass-ceramic composite material.[33] Controlled crystallization ensures that the distribution and sizes of the ceramic crystallites is as homogenous as possible which leads to a fine-grained microstructure.[36,37] This microstructure is desirable as it improves the mechanical properties of a glass material such as durability.[34,36,37] Uncontrolled crystallization can lead to a coarse microstructure with a few large crystallites which leads to undesirable properties.[36,37] Controlled crystallization became a novel tool to synthesize new and useful materials since it allowed for a homogenous microstructure and reproduceable properties.[34] This allowed glass-ceramic composite materials to be tailored for specific applications.[34]

1.4 Applications of Glass-Ceramic Composites

Glass-ceramic composite materials have found a wide range of uses by changing the composition of the glass or ceramic phases. One such application is bone implants. Bioglass® 45S5 is a unique glass-ceramic composite where the targeted crystalline phase is hydroxy apatite ($Ca_{10}(PO_4)_6(OH)_2$) with the composition of the entire material being 45 wt% SiO_2, 24.5 wt% Na_2O, 24.5 wt% CaO, and 6 wt% P_2O_5.[38] This glass-ceramic composite material is unique because the targeted $Ca_{10}(PO_4)_6(OH)_2$ crystallites form when exposed to bodily fluids.[38] The targeted crystal phase is hydroxy apatite ($Ca_{10}(PO_4)_6(OH)_2$) which is the main constituent in bone. [38] This harmony between the ceramic phase and the human body allows this material to be used as biologically stable implants and the glass phase can be used for drug delivery.[38] Another application is in cookware. Glass-ceramic composite materials can be made transparent by keeping the size of the crystallites on the nanometer scale.[39] Glass and ceramic materials can be combined to form a composite material that can have a net zero thermal expansion coefficient.[34] The thermal expansion coefficient of the material can be tuned to the desired value by varying the ratio between the glass and ceramic phases.[34] This is an important property when synthesizing materials for cookware and the aerospace industry since there can be a large temperature range during the use of these materials.[34] Glass-ceramic composites are also used as luminescent materials.[40] These materials take advantage of the sharp absorption in UV wavelengths and emissions in visible wavelengths of ceramics and combine it with the low self-quenching property of the glass.[40] Finally, glass-ceramic composites have also been proposed as a nuclear waste form.[1,41–45] Using a glass-ceramic composite as a nuclear waste form combines the ability of the glass to incorporate a large variety of elements with the higher stability of the ceramic crystallites.[2] The ceramic phase can be targeted to produce crystallites that can incorporate waste elements that have low solubility in glass.[2]

1.5 Glass-Ceramic Composite Materials for Nuclear Waste Sequestration

Various glass-ceramic composite materials have been investigated as waste forms for nuclear waste sequestration in the past. One glass-ceramic system that has been studied in the past is glass containing pyrochlore ($Gd_2Ti_2O_7$) crystallites.[2] Pyrochlore crystallites were chosen because they are able to incorporate a large amount of actinides with up to 30 wt% UO_2 found in natural samples.[2] In a study by Aluri et. al, the radiation stability of glass-ceramic composites containing pyrochlore was investigated.[2] Radiation stability is an important property to study in a potential

nuclear waste form as any structural changes due to the radioactive decay of waste elements can affect the chemical durability of the material over the long-term.[2] Radiation damage can be simulated by bombarding the material with high energy ions.[2] This bypasses the need to handle the actual radioactive elements and this also bypasses the need to wait for the radioactive decay to occur naturally. The simulated radiation damage was achieved by bombarding the sample with high-energy Au^- ions to simulate radiation damage from α-decay.[2] The radiation stability of the glass-ceramic composite material containing pyrochlore was observed to be similar to the radiation stability of the pyrochlore material.[2]

Glass ceramic composite materials consisting of brannerite ($CeTi_2O_6$) or zirconolite ($CaZrTi_2O_7$) dispersed in a borosilicate glass matrix were investigated in the past by Paknahad et al.[29] It was observed that the ceramic crystallites dissolved in the glass matrix at 1100 ^oC but this solubility was reduced when the composite material was formed at 750 ^oC.[29] The lower annealing temperature favoured crystallization of the glass, however, crystallization was minimized through the addition of Al to the glass composition, which reduces the mobility of alkali ions.[29] A deeper discussion of the role of Al_2O_3 in glass can be found in Section 1.7. Brannerite and zirconolite containing glass-ceramic composites were found to behave similarly under similar synthesis conditions.[29]

The effect of radiation damage was also investigated on Nd silicate apatite ($Ca_2Nd_8(SiO_4)_6O_2$) containing glass-ceramic composites by once again simulating the radiation damage using ion implantation.[46] The apatite crystallites closest to the surface became completely amorphous under radiation damage.[46] Changes in the glass phase in the glass-ceramic composite materials were observed through Raman spectroscopy. [46] It was suggested that the changes in the glass were caused by BO_3 units forming at the expense of the already formed BO_4 units.[46] Network modifiers that acted as a charge balance for BO_4 units were released into the borosilicate glass matrix and form non-bridging oxygens. This can decrease the chemical durability of the waste form as the ionic bonds that are formed by the network modifier and the non-bridging oxygens are more easily dissolved by water than the covalent bonds that hold the network formers together.[47] The stress in the glass caused by amorphization of the apatite crystallites was able to relax during the simulation of radiation damage causing no cracks to form regardless of crystallite size.[46] Previous studies which showed amorphization of the ceramic crystallites caused swelling of the crystallites leading

to cracks in the glass-ceramic composite waste form.[46] Cracks in a nuclear waste form increase the surface area of the waste form which leads to an increased leaching rate of waste elements when in contact with water.[48]

A study by Maddrell et al focused on how changes in the glass composition can affect the crystallization of zirconolite glass-ceramics.[44] This study was performed because it was found that the glass composition can have an affect on the identity of the ceramic crystallites that form even if the ratio of elements present in the ceramic phase are not changed.[44] The B:Al ratio in the glass was varied in this study.[44] It was found that lower Al content favoured the formation of secondary crystal phases such as zircon ($ZrSiO_4$), sphene ($CaTiSiO_5$), and rutile (TiO_2) at the expense of zirconolite ($CaZrTi_2O_7$).[44] Based on this, an equilibrium was suggested: $CaZrTi_2O_7 + 2SiO_2 \rightleftharpoons CaTiSiO_5 + ZrSiO_4 + TiO_2$.[44] The authors suggested that this equilibrium shifted to the right at lower Al content due to an increase in the effective concentration of silica within the glass based on thermodynamic calculations.[44]

Nagelschmidtite ($Ca_{7-x}Na_x(PO_4)_{2+x}(SiO_4)_{2-x}$) containing glass-ceramics prepared by Stefanovsky et al showed how this material has potential as a nuclear waste form.[49] Nagelschmidtite is hexagonal with the space group $P6_1$. It is composed of 4 chains along the c axis. Two of the chains only contain Na and Ca which are 6-, 7-, and 8-coordinate. The other two chains alternate between Na/Ca polyhedral and SiO_4/PO_4 tetrahedra. The sequence in the mixed columns is Na/Ca, SiO_4/PO_4, Na/Ca, SiO_4/PO_4, Na/Ca for the first column and Na/Ca, SiO_4/PO_4, Na/Ca, vacancy, SiO_4/PO_4, Na/Ca in the second column. Nagelschmidtite was able to incorporate U into the ceramic crystallites of glass-ceramic composite materials that were synthesized.[49] Various substitutions in the nagelschmidtite structure were also targeted and the limits of these substitutions were determined in this study.[49] Substitutions involving Nd^{3+}, Eu^{2+}, and U^{4+} were all shown to be possible in the nagelschmidtite structure by substituting into the Na and Ca sites.[49] This study showed the versatility in sequestering many of the different waste form elements into glass-ceramic composite materials containing nagelschmidtite.

Glass-ceramic composite materials consisting of rare-earth phosphate ($REPO_4$) crystallites dispersed in a glass matrix have also been studied as a potential nuclear waste form. A more in-depth description of rare-earth phosphates can be found below in Section 1.7. Previous work has reported that a Ca doped $CePO_4$ having the formula $Ca_{0.2}Ce_{0.8}PO_4$ as the crystalline phase can

allow for a greater degree of substitution of waste elements into the crystal lattice.[50] Ce exists as both Ce^{3+} and Ce^{4+} in the solid solution.[50] This versatile crystalline phase allowed various elements to be substituted into the lattice including Ag, Cs, Zr, and rare-earths.[50]

Other studies focused on the effect of CeO_2 addition on the formation of $REPO_4$ and the crystallization of the glass matrix. It was found that the addition of CeO_2 to an iron phosphate glass can promote the formation of $FePO_4$ crystallites after the CeO_2 crystallizes as $CePO_4$ when the glass was quenched.[51] CeO_2 promoted the formation of iron phosphate crystallites before $CePO_4$ formed when the glass was slow cooled.[32] Ce ions in a glass reorders the glass structure to satisfy its' own high coordination requirements.[32,51] This reordering helped to decrease the stability of the iron phosphate glass and made it easier for the glass to partially crystallize.[32,51] Quenching the glass from a high temperature can help to decrease the ability of a glass to crystallize; however, $CePO_4$ crystallites can help to provide a surface for nucleation and crystal growth to occur by providing heterogeneous nucleation sites. [23,26,27,51] Slow cooling a glass from a high temperature gives the glass more time to reorder into an equilibrium state and crystallize.[23,26,27] This can help to explain why the difference in cooling rates affected the crystallization of the material.

1.6 Rare-Earth Phosphates

Natural rare-earth phosphates ($REPO_4$) have been found to incorporate U and Th while remaining crystalline over geological timescales.[13,54] Anhydrous rare-earth phosphates can adopt the monazite or xenotime structures which are shown in Figure 1.1.[55–57] The monazite structure is formed by the light rare-earth elements (La-Gd) and is monoclinic with the space group $P2_1/n$.[14,54,58] The rare earth ion in monazite is 9-coordinate while P is 4-coordinate.[14,54,58] The xenotime structure is formed by the heavy rare-earth elements (Dy-Lu, and Y) and is tetragonal with the space group $I4_1/amd$.[14,54,59] The rare earth ion in xenotime is 8-coordinate while P is also 4-coordinate in this structure.[14,54,59] Monazite and xenotime have been shown to be able to recover their long-range order after simulated radiation damage through reannealing at low temperatures.[14] Decay of the radioactive elements produces heat which can raise the temperature within the material to be high enough for this recovery to occur.[14,24] Monazite and xenotime have also been shown to be more resistant to leaching in water when compared to glass which is an important property for waste forms as they may encounter ground water while in a geological repository.[48]

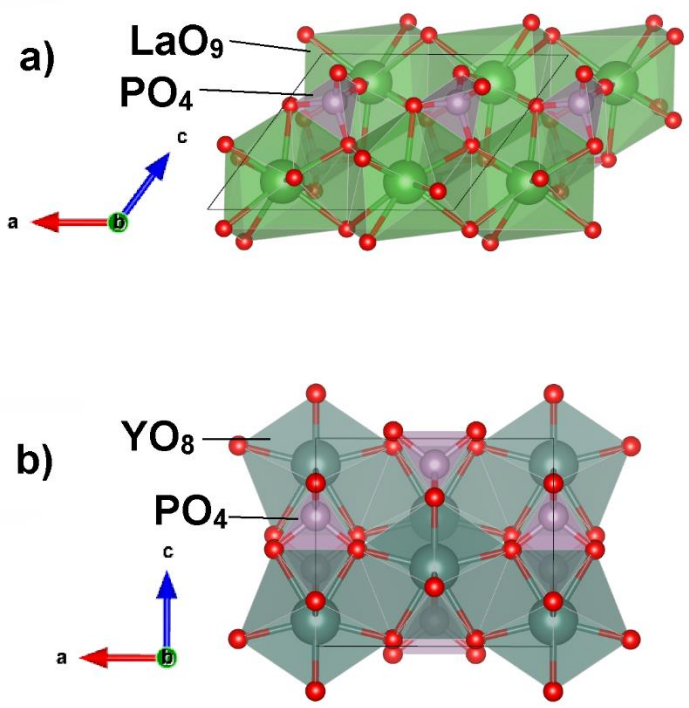

Figure 1.1: Crystal structure of a) $LaPO_4$ adopting the monazite structure and b) YPO_4 adopting the xenotime structure.[60,61]

The monazite structure is made of 2 columns of alternating REO_9 polyhedra and PO_4 tetrahedra along the [0 0 1] direction.[54,62] The 2 columns are connected by edge sharing REO_9 polyhedra.[54,62] This structure has highly distorted PO_4 tetrahedra leading to 9 different RE-O bond lengths and monazite can incorporate many different elements since the size restriction on this crystallographic site is not severe due to the distortion of the polyhedra.[54,62] Monazite was found to be stable across complete solid solutions of light rare-earth elements for La-Eu, La-Gd, and Gd-Eu systems.[54] The lattice constants for these solid solutions varied linearly from one end-member to the other.[54] Cerium can be tetravalent as well as trivalent. This allows for coupled substitutions in $CePO_4$ with divalent cations such as Ca.[54] This leads to compositions such as $Ce^{3+}_{1-2x}Ce^{4+}_{x}Ca_xPO_4$.[54] Xenotime has a more symmetrical structure than monazite.[40,42] This is because the heavier rare-earths present in xenotime are smaller than those found in monazite and, as a result, do not distort the PO_4 tetrahedra as strongly.[42] Chains of edge connected ReO_8 and PO_4 polyhedra form along the [0 0 1] direction in xenotime.[42]

Monazite and xenotime are related to each other by an offset between two tetrahedra in adjacent chains along the [0 1 0] direction as well as a slight rotation about the [0 0 1] direction in the monazite structure compared to xenotime.[42] The synthesis conditions that determine whether a rare-earth phosphate adopts the monazite or xenotime structure has been found to include the size of the rare-earth cation, annealing temperature, and pressure.[54] The light rare-earths are too large to fit in the REO_8 polyhedra in the xenotime structure and need to distort the REO_x and PO_4 polyhedra and occupy the void space that is present in the xenotime structure.[62] High annealing temperatures were observed to increase solubility of heavy rare-earths, such as Y, in the monazite structure.[54] Annealing temperature can affect the final structure of the rare-earth phosphates by starting with a hydrous version of the rare-earth phosphate.[54] The hydrated rare-earth phosphate, rhabdophane $REPO_4 \cdot 0.5H_2O$, can be synthesized by precipitating the rare-earth phosphate from a solution followed by low temperature annealing.[59] High temperature annealing can then be used to induce a phase transition from rhabdophane to monazite or xenotime depending on the rare-earth present since rhabdophane is only metastable and is not stable at high temperatures.[59] Heavy rare-earths were observed to adopt a mixture of the monazite and xenotime structures depending on the annealing temperature used.[59] Xenotime-type $GdPO_4$ can be made by starting with rhabdophane even though it typically adopts the monazite structure.[54] Monazite-type $TbPO_4$ and $DyPO_4$ can be made by starting with rhabdophane even though it typically adopts the xenotime structure.[54] These phase transformations take place due to the metastable nature of rhabdophane and the ionic size of the rare-earths being at the boundary between monazite and xenotime.[54] High pressure can be used during the synthesis of $Ce_{1-x}Y_xPO_4$ to increase the solubility of Y in $CePO_4$.[54] Additionally, a reversible phase transition from xenotime to monazite was observed in YPO_4 and $ErPO_4$ systems at high pressures (17.3-19.7 GPa).[54] High pressure synthesis techniques such as hot isostatic pressing can take advantage of this increase in solubility to synthesize ceramic waste forms with higher wt% of nuclear waste.[43]

1.7 Borosilicate Glass

Although the glass composition can be optimized for maximum solubility for different waste streams, the amount of waste that can be loaded into the waste form remains limited to a few weight %.[3] The most popular types of glasses being considered/used are silicate glass and phosphate glass. [63] One type of silicate glass being considered/used is borosilicate glass (BG) due to the high durability and the well characterized structure of this glass type.[1] The glass network of

borosilicate glass containing alkali and alkaline-earth elements are generally composed of SiO_4 and BO_4 tetrahedra, as well as trigonal planer BO_3.[1] The alkali ions preferentially charge balance BO_4 structural units before starting to partition into the rest of the glass network in large amounts making non-bridging oxygens.[64] The extent of the BO_3 that is transformed into BO_4 is dependent on the Na_2O:B_2O_3 and SiO_2:B_2O_3 ratios.[65] Bonds between two BO_4 units is energetically unfavourable due to a local accumulation of charge.[66] The composition where Na_2O begins to partition into the rest of the glass network in large amounts corresponds to:

$$\frac{[Na_2O]}{[B_2O_3]} = 0.5 + \frac{[SiO_2]}{2N[B_2O_3]} \quad (1.1)$$

where N is a constant that represents the average number of Si that is around B and equals between 5 and 6.[65] The addition of boron to silicate glass increases the chemical stability, lowers the processing temperature, and allows the glass to possess a relatively large neutron capture cross section which are all useful properties for synthesizing a nuclear waste form.[9]

Alkali and alkaline-earth elements can help to lower the processing temperature and increase the solubility of nuclear waste elements such as lanthanides.[67] These properties are achieved due to non-bridging oxygens that form when alkali and alkaline-earth elements are added. The non-bridging oxygens, which breaks up the glass network, decreases the viscosity allowing lower temperatures to be used since the glass transition temperature is dependant on viscosity.[68] When heating a glass, the viscosity increases very slowly until a temperature is reached where the viscosity is able to increase continuously.[68] This temperature is the glass transition temperature.[68] As the glass transition temperature is based on the viscosity of the glass melt, lowering the viscosity would allow the formation of the glass at a lower temperature.[18,68] These non-bridging oxygens also help rare-earth ions dissolve in the glass network by charge balancing the lanthanide-oxygen structural units.[67] These structural units consist of lanthanides surrounded by 6-8 non-bridging oxygens.[67] Alumina can be added to suppress crystallization of SiO_2 and improve the leaching resistance of the glass in alkali silicate glasses since it strongly couples to the alkali.[1] This is caused by negatively charged AlO_4 units forming within the glass which require a positively charged network modifier to charge balance it.[1] Al reduces the mobility of a network modifier by coupling with that modifier.[1] By reducing the mobility, the structural rearrangement that is

required to happen for crystallization of the glass to occur as well as the dissolution of the network modifiers is stopped.[1] This is an important effect since crystallization of the glass can lead to cracking and failure of the waste form. ZnO and ZrO_2 also serve to couple with the network modifiers to suppress crystallization and improve leech resistance in the same way as Al_2O_3.[1] A current nuclear glass composition that utilizes the glass chemistry of these elements to produce a nuclear waste form is the French R7T7 material composed of (in wt%): 45.12 SiO_2, 13.92 B_2O_3, 10.06 Na_2O, 4.92Al_2O_3, 4.01 CaO, 2.49 ZnO, and 1.01 ZrO_2.[1]

1.8 Chemistry of Actinide and Actinide Surrogates in Waste Forms

The chemistry of actinides can be studied using actinide surrogates which partially mimics the chemistry of the actinides.[28,32,69–73] This is done in order to avoid working with radioactive isotopes. By using actinide surrogates, researchers can study materials that are proposed to contain radioisotopes of actinides.[28,32,69–73] These materials can thus be characterized in a safe manner before having to use actinides in a validation study.[74] Typically, rare-earth elements are used as the surrogate due to similar electronic structures and ionic radii.[28,32,69–73] For instance, Gd^{3+} has been used as an actinide surrogate for Am^{3+} and Cm^{3+} while Sm^{3+} has been used as an actinide surrogate for Np^{3+}.[74,75] Cerium is a commonly used surrogate for plutonium.[28,32,69–73] The ionic radii of Ce and Pu are similar for a given coordination number (Table 1.1) and Ce is stable as Ce^{3+} and Ce^{4+} which partially mimics the oxidations states of Pu.[76]

Table 1.1: Ionic radii of $Ce^{3+/4+}$ and $Pu^{3+/4+}$ with specific coordination numbers.[76]

	Oxidation State	Coordination Number	Ionic Radius [Å]
Ce	+3	6	1.01
Ce	+4	6	0.87
Ce	+4	8	0.97
Pu	+3	6	1.00
Pu	+4	6	0.86
Pu	+4	8	0.96

1.9 Wet and Dry Synthesis Methods

Several methods to synthesize glasses and ceramics have been established in the literature. Among these are the ceramic and coprecipitation methods.[77] The ceramic method is a standard solid-state synthesis method that involves the mixing and annealing of dry powders to obtain a desired product.[77-79] Annealing at high temperature (>1000 ^{o}C) is often required using this method due to the low mobility of the ions in the solid state.[77-79] This slow diffusion of the ions is compounded by long diffusion distances leading to long reaction times on the order of days.[77-79] The reaction proceeds at the interface between the precursor powders and as such the diffusion distance the ions are required to travel increases as the reaction progresses.[80] The precursor powder can be compressed to form a pellet to shorten diffusion distances and the material can be ground and mixed intermittently during the reaction to expose new surfaces to speed up the reaction.[80] When there is a melt at the annealing temperature, such as in the case of glass, the reaction can proceed much more quickly due to the faster diffusion rate.[81]

The coprecipitation method is performed by dissolving the precursors in a solution.[77] Following this, the precursors are precipitated out of the solution (typically as hydroxides under basic conditions).[77,78] Once this is achieved, the precursor powder can be pressed into a pellet and annealed. The advantage to this method is the more intimate mixing of the precursors.[49] This lowers the diffusion distance the ions need to travel for the reaction to take place which allows lower annealing temperatures to be used to synthesize materials.[49] Using synthesis conditions to precipitate all cations in the solution is crucial to maintain stoichiometry.[77] The coprecipitation method can offer advantages compared to the ceramic method for synthesizing nuclear waste forms. This is due to the fact that high-level nuclear waste may already be in a liquid state.[82] This allows for an opportunity to use the coprecipitation method without requiring extra synthetic steps. The benefits of this could potentially be the formation of the waste form with less processing steps and using less energy.

1.10 Synthesis of Glass-Ceramic Composites

Glass-ceramic composite materials can be synthesized using a variety of methods.[23] The first method used to synthesize glass-ceramic composite materials was developed by Stookey.[33] This method transforms a premade homogenous glass into a glass-ceramic composite by nucleating and

growing ceramic crystallites.[33] This transformation from a homogenous glass into a glass-ceramic composite is accomplished through the use of heat treatments.[33] After making the homogenous glass with the desired composition, nucleating agents such as TiO_2 or CeO_2 can be added during the heat treatments to aid in growing the desired crystalline phase.[33] These nucleating agents, which have low solubility in the glass, provides heterogenous nucleating sites within the glass which allows a lower activation energy for crystallization to be reached.[33] The temperature required for the heat treatments is determined by the glass composition.[1] By changing the glass composition, the temperature range for crystallite nucleation and maximum crystallite growth can be varied.[1] Two heat treatments are necessary if the temperature ranges for nucleation and growth are well separated, one for nucleation and a second for crystal growth.[1] If the temperature ranges for nucleation and growth are not separated only one heat treatment is required as nucleation and growth can both occur.[1] This synthesis method possesses several advantages over the other methods.[52] One advantage is that since the homogenous glass is made first followed by transformation into a glass-ceramic composite through crystallite nucleation and growth within it, the glass-ceramic composite material can be made with little to no porosity.[52] This is because the original pore-free glass can be transformed into a glass-ceramic composite without the formation of bubbles.[83] This is done by limiting the microstructure to small crystallites and smaller volume % of crystallites.[83] The bubbles form due to the crystalline phases not being able to dissolve as much gases as the glass phase.[83] As the amount of glass is reduced when transforming a glass into a glass-ceramic some gases will not be able to stay dissolved in the material and bubbles will form.[83] This can be very important in areas such as microelectronics where the acceptable number of defects within the material is extremely low.[52] Another advantage of this synthesis method is the option to shape the homogenous glass before any heat treatments take place.[52] This is quite useful as the heat treatments do not affect the shape of the glass.[52] Shaping a glass is much easier than shaping a ceramic or a glass-ceramic composite so this is a very important advantage for this synthesis method in the application of glass-ceramic composite materials.[52] The number and size of the crystallites can be controlled by changing the temperature or annealing time of the heat treatments.[52] A disadvantage to this method is a consequence of first making a homogenous glass; the targeted ceramic phases are strongly dependant on the glass composition.[84] This limits the possible number of glass compositions and ceramic combinations.[84]

A modification of the synthesis method developed by Stookey uses a crushed glass powder instead of uncrushed glass.[34] After the homogenous glass is made, it is crushed to form a powder.[34] The glass powder (or glass frit) is then compacted into a desired shape followed by heat treatments.[34] The heat treatments, again, serve to nucleate and grow ceramic crystallites.[34] The heat treatments serve an additional process when transforming a powdered glass into a glass-ceramic composite, which is to remove/minimize the porosity that was created as a by-product from compacting the powders.[34] The shape and size of the final glass-ceramic composite may change due to the heat treatments even though the glass powder can be made into a desired shape before the heat treatments.[52] The advantages of this synthesis method over the previous synthesis method that did not crush the homogenous glass into a powder prior to heat treatments is that lower temperatures for the heat treatment(s) can be used, and no nucleating agents are necessary.[34,52] These advantages can be achieved because the interfaces in the compacted powder can serve as heterogenous nucleating sites to nucleate and grow the ceramic crystallites.[34,52]

Another modification of the method Stookey developed to transform a homogenous glass into a glass-ceramic composite involves slow cooling the glass melt instead of quenching it.[23,26,27] The slower cooling rate allows more time for nucleation and growth of the ceramic crystallites to occur when compared to quenching the glass, which preserves the amorphous structure.[23,26,27] A homogenous glass melt may undergo phase separation as a glass is cooled.[85] This phase separation can take the form of small glass beads dispersed in a continuous glass matrix as seen in Figure 1.2.[85] While both the glass matrix and glass beads are amorphous they have distinct compositions and distinct properties from each other and the material cannot be described as having a constant composition throughout the material.[85] As the glass cools further, the glass beads can crystallize leading to a microstructure of ceramic crystallites dispersed in a glass matrix.[85] Since the ceramic crystallites form from the phase separated glass spheres the identity of the ceramic(s) is dependant on the composition of the glass spheres.[85] While this method is the easiest synthesis method to use, the microstructure of a composite material synthesized in this way can cause a large variance in the size and shape of the crystallites.[85]

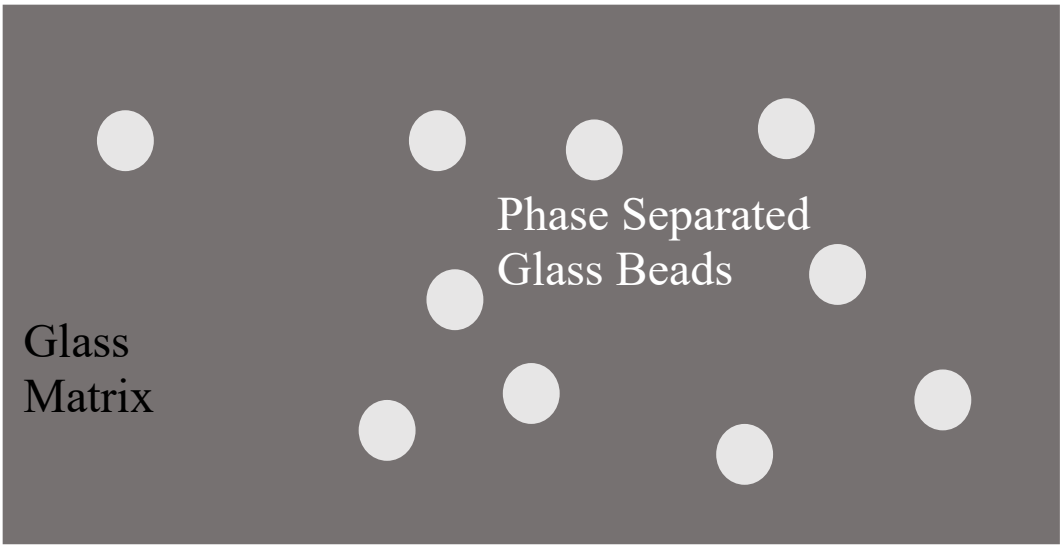

Figure 1.2: Microstructure of a phase separated glass. The glass matrix and glass beads possess distinct compositions.

A final synthesis method to produce glass-ceramic composites does not transform a homogenous glass into a glass-ceramic composite. The first step of this synthesis method makes the glass and ceramic phases separately followed by a second step which combines the two powdered phases together and anneals it to produce a glass-ceramic composite material.[2,29] Making the two phases separately allows for some advantages over the other synthesis methods. This method does not require any knowledge of the temperatures for nucleation and growth as the ceramic phase is initially made separately from the glass. The number of possible combinations of glass and ceramic compositions is potentially greater than what is possible using the method that Stookey developed or the modifications thereof since the glass and ceramic phases are made separately.[84] This means the ceramic phase would not be required to be soluble in the glass or melt at the temperature used to make the glass.[84] A disadvantage of this synthesis method is that the processing methods used to make single-phase ceramics can be more difficult than the processing methods used to make glass.[1]

1.11 Characterization Methods

Glass ceramic composite materials consisting of rare-earth phosphate crystallites dispersed within a glass matrix were synthesized for this work. The long-range order was studied using X-ray diffraction; the morphology was studied using electron microscopy; and the local chemical

environment of glass or ceramic forming cations were studied using X-ray absorption spectroscopy.

1.11.1 X-ray Diffraction (XRD)

X-ray diffraction is a technique that analyses a special case of scattering known as diffraction. In X-ray diffraction the incident X-rays scatter off the elements' electrons.[86] The elements are located in lattice planes within crystalline materials.[86] The scattered X-rays interfere constructively and destructively.[87] This constructive and destructive interference is called diffraction.[87] Diffraction requires long-range order to occur and, as such, amorphous materials, which lack long-range order, do not diffract strongly.[87] The path length difference between the X-rays needs to be different by a distance of nλ for the X-rays to constructively interfere where n is an integer number (Figure 1.3).[86] This relationship can be quantified using Bragg's Law:

$$n\lambda = 2d\sin(\theta) \tag{1.2}$$

where n = 1, 2, 3, etc., d is the distance between lattice planes, and θ is half of the diffraction angle.[87]

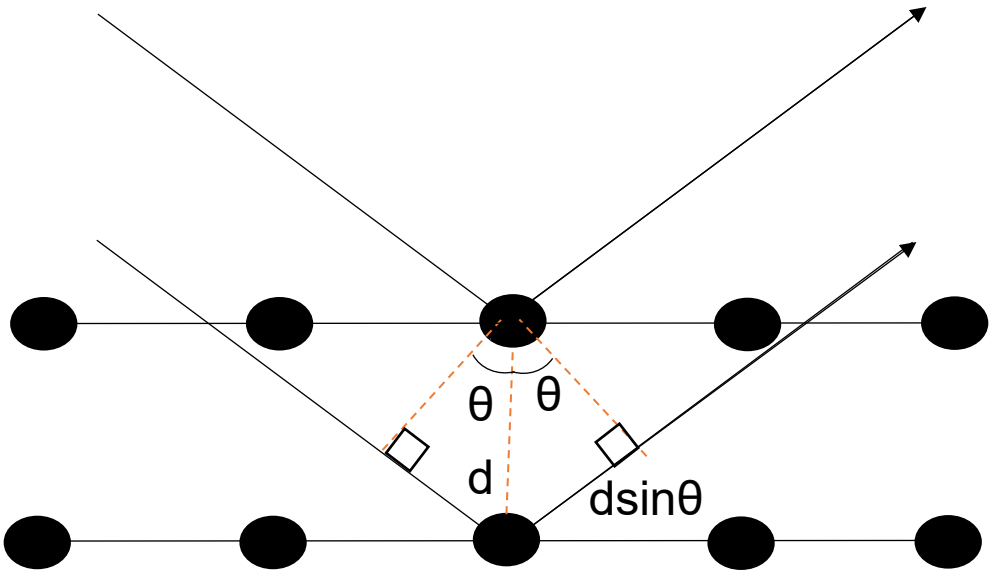

Figure 1.3: Lattice plains diffracting X-rays.

By collecting data at different angles, different lattice planes would satisfy the conditions for diffraction and an X-ray diffraction pattern can be obtained by plotting the intensity against 2θ.[87] The position and relative intensity of the peaks in these patterns gives information on the identity and composition of the crystalline phases present.[86] A shift in the 2θ values of the peaks can result from a change in the spacing between the lattice planes.[86] A shift to higher 2θ values can indicate a smaller unit cell, whereas a shift to lower 2θ values can indicate a larger unit cell.[86] This can be inferred in Bragg's Law by d and 2θ having an inverse relationship. A change in composition can affect the size of the unit cell and change the relative intensity of the observed peaks.[86] Information is obtained from XRD patterns through the comparison of experimental patterns to patterns calculated from crystal structures found in databases.[86] The calculated pattern is refined to match the experimental pattern. The background, lattice constants, peak shape**,** thermal parameter, and atomic positions are among the variables that can be refined.[86] The intensity of the observed peak is proportional to the electron density in that lattice plane and, therefore, the number of electrons on an atom in that plane.

Peak broadening can be caused by small crystallite sizes or by microstrain.[86] Smaller crystallites do not diffract as strongly since there is less long-range order available to cause constructive and destructive interference of the X-rays.[86] Peak broadening caused by small crystallite sizes can be modeled using the Scherrer equation:

$$D = \frac{k\lambda}{B\cos(\theta)} \tag{1.3}$$

where *D* is the crystallite size, *k* is a constant and the value changes depending on the shape of the particle, λ is the X-ray wavelength, *B* is the full width at half maximum of the diffraction peak after correction for instrumental broadening, and θ is half of the diffraction angle.[86] Microstrain is caused by defects within the lattice such as dislocations and leads to broader peaks. The effect of strain on an XRD pattern can be modelled using:

$$B = 4\varepsilon \frac{\sin(\theta)}{\cos(\theta)} \tag{1.4}$$

where *B* is the full width at half maximum of the diffraction peak after correction for instrumental broadening, ε is the microstrain, and θ is half of the diffraction angle.[86] The crystallite size and

microstrain can be calculated for a variety of peaks to determine the cause of broad diffraction peaks.[86] A Williamson-Hall plot can be used to separate the contributions from these two effects using:

$$B\cos(\theta) = 4\varepsilon \sin(\theta) + \frac{k\lambda}{D} \quad (1.5)$$

The slope of this plot gives information regarding the strain while the intercept gives information about the crystallite size.[86]

1.11.2 Electron Microscopy

Electron microscopy is a collection of techniques that uses an electron beam to image a sample. This irradiation can produce back-scattered electrons, secondary electrons, auger electrons, and fluorescence photons which can provide elemental and morphological information.[88] The main draw to using electron microscopy, specifically scanning electron microscopy and electron microprobe, as a characterization technique is the extremely high resolution which can measure a sample on the nm scale.

Scanning electron microscopy and electron microprobe are two examples of electron microscopy. The difference in these instruments is minimal and are largely found in their history.[88] The scanning electron microscope was envisioned to use electrons as the signal to collect morphological information on the sample while the electron microprobe was created to quantify the X-ray fluorescence.[88] As time went on these techniques converged and now both can collect a range of signals using various detectors.[88] Figure 1.4 shows a diagram of an electron microscope. The electron gun is the source of electron beam (electron beam is the black arrow originating from the electron gun in Figure 1.4). The condenser lenses are magnetic lens to help focus the electron beam. The objective lens is the most powerful magnetic lens and is the last lens in line before the beam interacts with sample.[88] The detectors can be present within the objective lens or outside of it.[88] Scanning electron microscopy experiments are performed by rastering the electron beam over the sample and collecting data at each spot in order to construct an image using each spot as a pixel.

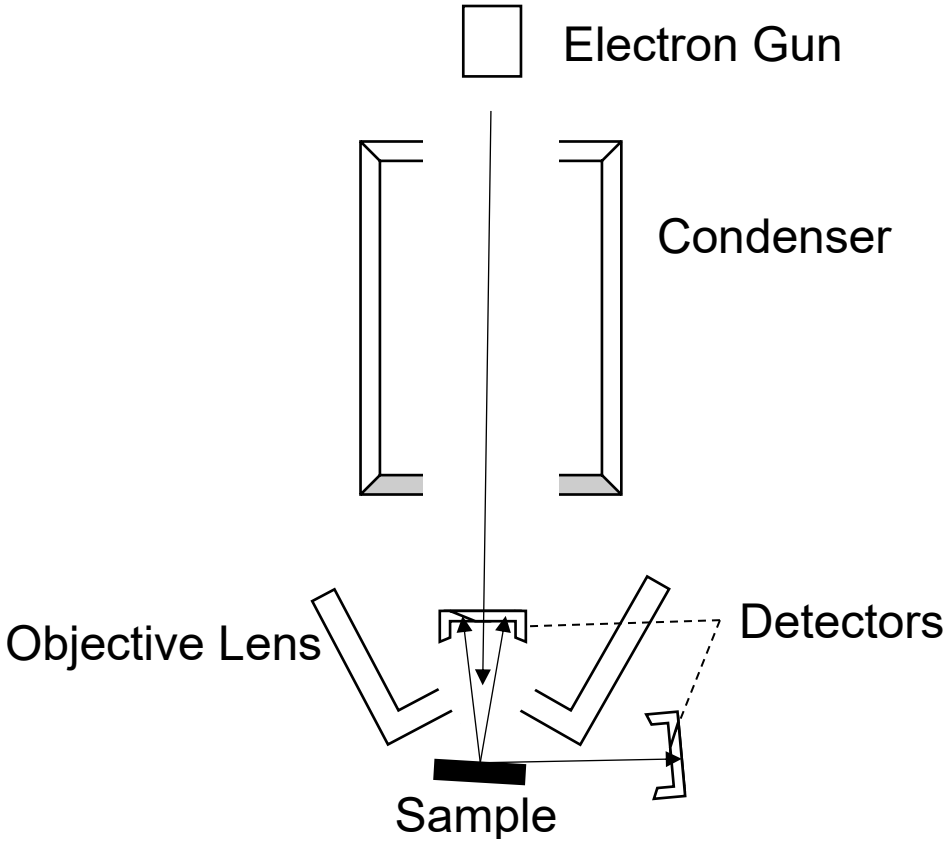

Figure 1.4: Schematic of a scanning electron microscope.

Secondary electrons, back scattered electrons, and fluorescence are three signals that can provide complimentary information (the three black arrows originating from the sample in Figure 1.4). Secondary electrons are caused by electrons being ejected from the top layer of the sample.[88] Only the secondary electrons created close to the surface can be detected as secondary electrons created in the bulk of the material can not travel enough distance to escape from the surface.[88] As a result of this, topological information of the sample can be gathered by detecting secondary electrons.[88] Back scattered electrons are created through elastic collisions with the electrons within the sample.[88] The back scattered electrons are scattered back in the direction the electron beam came from.[88] The higher the atomic number of the element in the sample, the more electrons are present, and the more back scattered electrons are observed.[88] This leads to a dependence of the intensity of a signal on the atomic number of the elements present in that location.[88] Detecting fluorescence uses an energy dispersive X-ray spectroscopy detector and can be used to either map out the elemental distribution of a material or collect spectra from individual spots. These two

collection techniques can either show the distribution of a single element at a time or show all the elements present at a spot in a sample.[88] X-ray fluorescence occurs due to the electron beam exciting core electrons within the sample.[88] Characteristic X-ray photons are produced when the electrons relax back to the ground state and can be detected.[88]

1.11.3 X-ray Absorption Spectroscopy (XAS)

X-ray absorption spectroscopy uses X-rays to probe elements within a material. When X-rays of a specific energy strike an element there is a chance of an absorption event.[89] This absorption event excites a core electron into unoccupied conduction states.[89] The absorption follows the dipole selection rules where $\Delta l = \pm 1$.[89] This technique is element specific since the excitation of core electrons occur only when there is a photon with a specific energy.[89] The absorption events in XAS collected in transmission mode follows Beer's Law:

$$I_t = I_0 e^{-\mu t} \tag{1.6}$$

where I_t is the intensity of the X-ray beam after absorption, I_0 is the initial intensity, t is the thickness of the sample and μ is the absorptivity of the sample.[90] When t is not held constant, equation 1.6 can be rearranged to give equation 1.7.[89]

$$\mu t = \ln \frac{I_0}{I_t} \tag{1.7}$$

The spectra can be presented by plotting μt vs. energy. An XAS spectrum is labeled by the element and absorption edge that was collected. An absorption edge is the part of the spectrum where a sharp rise in μt is observed.[89] This rise in intensity is caused by the energy of the X-ray matching the energy of the transition.[89] The transition is labelled by which orbital the core electron was excited from.[90] The principal quantum number, n, is the first part of the label.[90] The value of n is assigned a letter starting with K when $n = 0$ and continues to L, M, and so on as n increases.[90] The second part of the label is determined by the angular momentum quantum number. A transition from the 2s orbital ($n = 2$; $l = 0$) is called the L_1-edge, where as a transition from the 2p ($n = 2$; $l = 1$) orbital is called the $L_{2,3}$-edge.[90] As there is a loss of degeneracy in the 2p orbitals due to spin-orbit coupling after excitation occurs, there are two transitions that are observable in the $L_{2,3}$-edge spectrum which are the L_2- and L_3-edges.[89] XAS is able to give information on the local chemical

environment of an element; however, the resulting spectrum would be an average of all the different environments the element is present in within the sample.[89]

An XAS spectrum consists of two parts (Figure 1.5).[89] The first is the near-edge region while the second is the extended fine structure region commonly referred to as XANES and EXAFS, respectively.[91] In the X-ray absorption near edge spectroscopy (XANES) region, the area of the spectrum proceeding the edge is the pre-edge region while the area following the edge is the main-edge region (up to about 50 eV).[90] The extended X-ray absorption fine structure (EXAFS) region begins after the main-edge XANES region and can extend to hundreds of electron volts above the edge.[90]

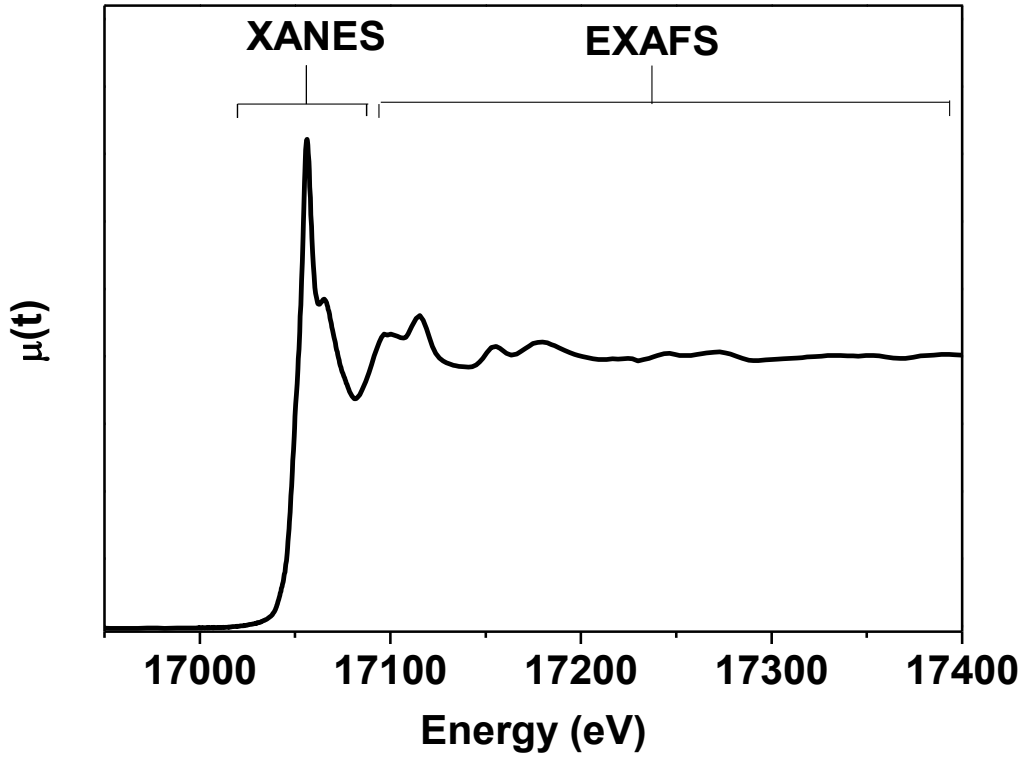

Figure 1.5: Example of an Y K-edge X-ray absorption spectroscopy (XAS) spectra.

The X-ray absorption near edge spectroscopy (XANES) region can contain multiple features.[89] The first is the absorption energy of the edge.[91] The energy of the edge can increase or decrease depending on the oxidation state of the cation and the bond characteristics of the anion-cation bonds.[91] When the ion is more oxidized there is less shielding and therefore more of an attractive force from the nucleus on the electrons.[89] This increases the energy of the edge as more

energy is needed to excite the core electron.[89] The same principle applies to bond character, when a bond withdraws more electron density away from the absorbing element, the core electron is attracted to the nucleus due to less shielding of the core electron and the edge shifts to a higher energy.[89] The energy of the edge can therefore give information on the average oxidation state of the ion and character of the bond.[89]

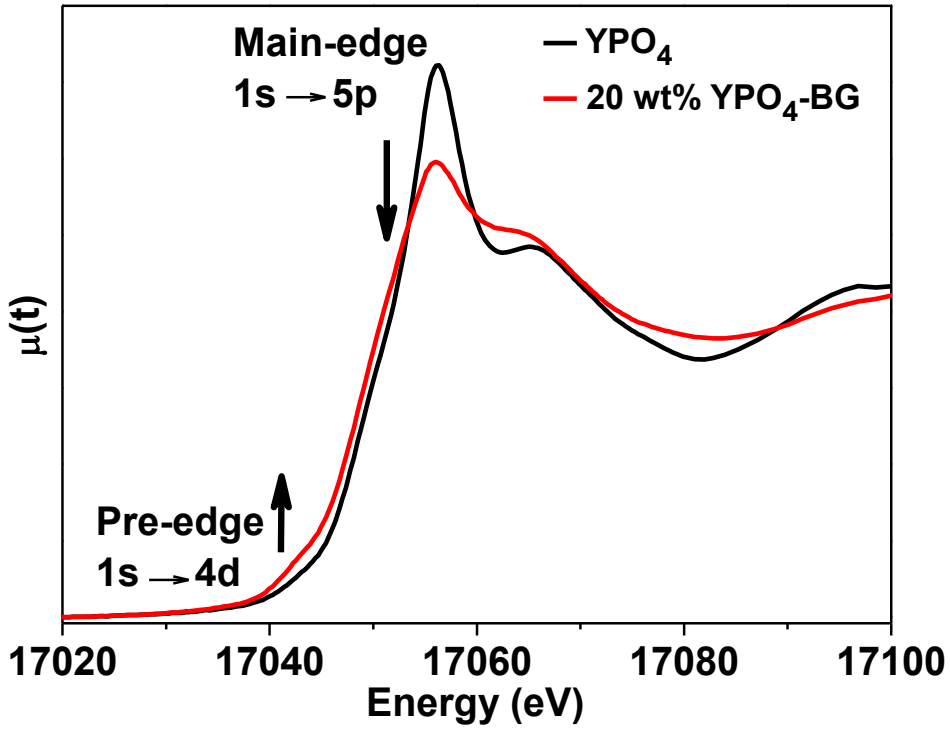

Figure 1.6: Example of Y K-edge XANES spectra that demonstrates how a change in the coordination environment can affect the spectra.

The main-edge region represents a dipolar transition while the pre-edge typically is caused from a quadrupolar transition with mixed dipolar character due to overlap of the p and d orbitals.[89] Multiple pre-edge peaks may be present in the spectrum.[89] More overlap of the orbitals occurs when there is no centre of symmetry.[89] Thus, a four-coordinate metal tetrahedron will have more orbital overlap of the p and d orbitals than the same metal that is six-coordinate with an octahedral geometry.[89] This affects the spectrum by increasing the intensity of the pre-edge and decreasing the intensity of the main-edge.[89] Figure 1.6 shows this effect by comparing a rare-earth phosphate (YPO_4) to a glass-ceramic composite containing a rare-earth phosphate (20 wt% YPO_4-BG) where some YPO_4 is dissolved in the glass. Changes in the Y K-edge XANES spectra can be observed since the coordination number of Y in YPO_4 is larger than the coordination number of Y when it

is dissolved in glass (Figure 1.6). Changes in the coordination number of the ion can therefore be observed in XANES spectra.[89] The XANES spectra are normalized in order to compare spectra of the same edge to each other.[89]

Extended X-ray absorption fine structure (EXAFS) spectra are characterized by the oscillations that can be observed at energies above the XANES region (Figure1.5).[90] By collecting the XAS spectrum at energies above the XANES region, a core electron can receive energy greater than the binding energy and become a photoelectron.[90] In order to explain the oscillations the outgoing photoelectron can be treated as a wave.[80] The photoelectron can be backscattered by electrons on neighbouring elements.[80] This produces a phase shifted wave which then interferes with the original wave.[80] The interaction between the backscattered photoelectron and the outgoing photoelectron leads to an interference pattern which affects μ.[80] The interference pattern is the source of the oscillations that are observed (Figure 1.5).[80] The interference pattern can be plotted in real space to observe up to three coordination shells of the element.[90] A model structure, which is used to simulate the scattering, is needed to interpret these spectra.[90] The simulated scattering can be refined in order to match the experimental spectrum.[90] Coordination number and bond distances can be determined by performing this analysis.[90]

The vast majority of XAS experiments are performed at a synchrotron facility using synchrotron radiation.[92] Synchrotron radiation is a focused, tuneable, and highly polarized and intense beam of light.[80] The Canadian Light Source (CLS) located in Saskatoon, Saskatchewan is an example of a synchrotron facility.[93] The X-ray photons in a synchrotron are produced through bending the path of high energy electrons that are traveling at relativistic speeds.[94] The electrons are produced in the electron gun.[94] Electrons are typically thermally ejected from a source and enter a linear accelerator.[94] The linear accelerator uses radio frequency cavities to accelerate the electrons which can reach an energy of 100 MeV.[94] The electrons move into the booster ring from the linear accelerator.[94] The electrons circulate in the booster ring until the energy reaches 2.9 GeV.[93] After the electrons reach this energy, they are transferred to the storage ring.[94] The storage ring is where the photons in a synchrotron are produced.[94] The CLS storage ring is composed of 12 straight sections with bending magnets at the end of each section and insertion devices in the straight sections. The electrons travel in a circular path from the use of the bending magnets.[94]

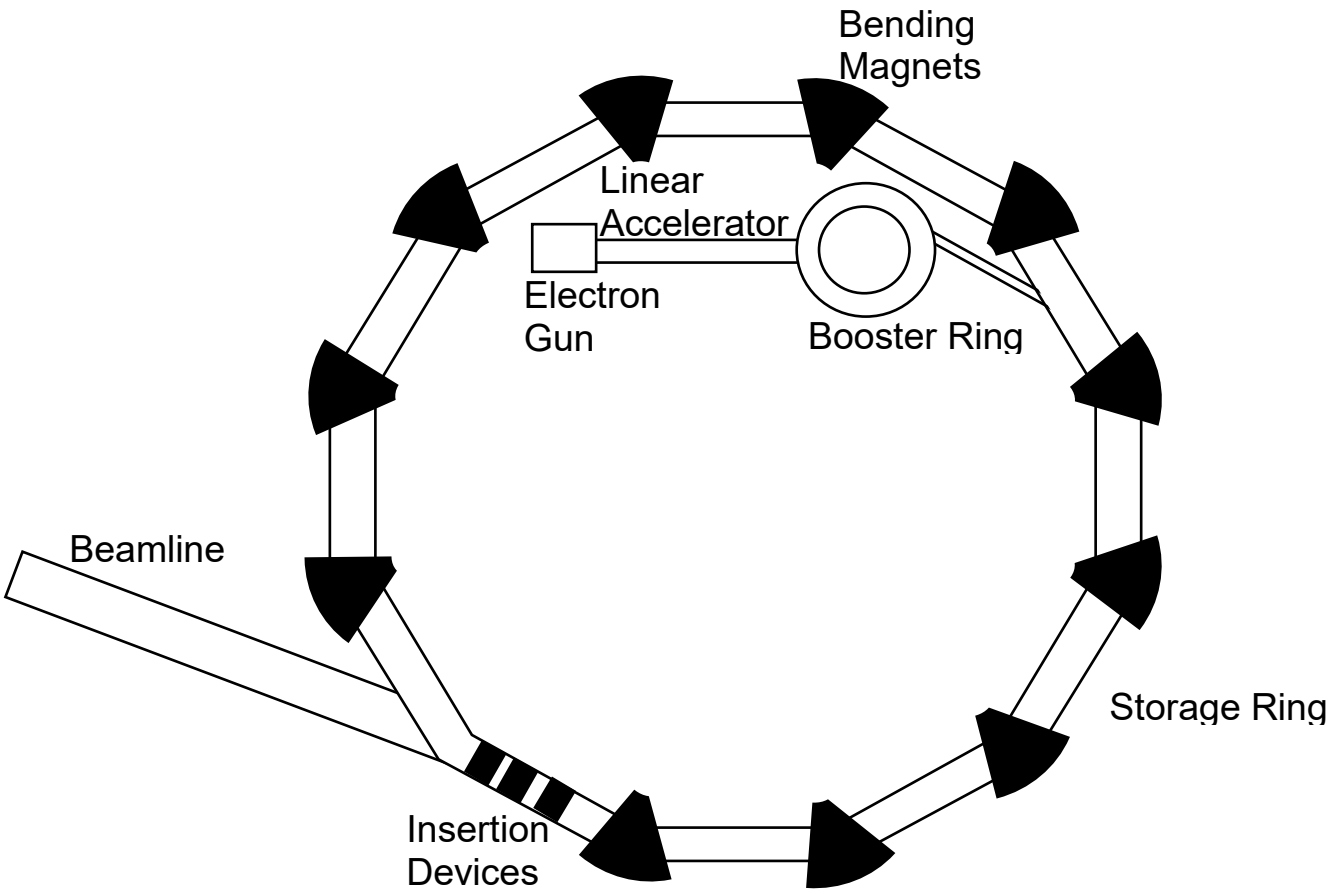

Figure 1.7: Schematic of a Synchrotron.

Electrons give off energy in the form of photons when they change direction.[94] These photons can have energies anywhere between infrared radiation to X-rays.[94] Insertion devices are magnets within the straight section of the storage ring.[94] These move the electrons back and forth while it travels in the straight sections.[94] The effect of the insertion devices can either be higher energy X-rays or higher photon flux at a specific energy.[94] The photons travel in a beam along a path that is tangential to the circular path of the electron.[94] This beam travels through a beamline where it reaches the experimental end station.[94] The beamlines are composed of optics that select a desired wavelength and an end-station where the experiment using synchrotron radiation takes place.[94] XAS spectra can be collected in transmission, fluorescence, and total electron yield modes.[89] In hard X-ray experiments performed in transmission and fluorescence mode (Figure 1.8), the photon beam is passed through an ionization chamber containing an inert gas.[90] The current caused by the ionization of the gas is measured and used to calculate the flux (I_o).[90]

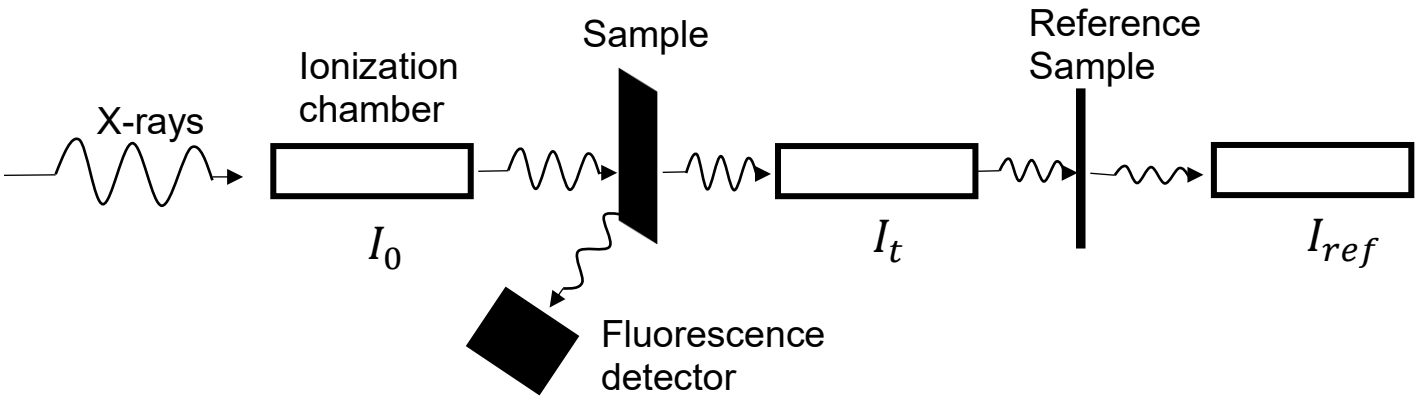

Figure 1.8: Hard X-ray experimental set-up.

This allows the flux to be measured after it interacts with a sample (I_t).[90] A calibration spectrum is able to be collected at the same time by a placing a reference sample plate and another ionization chamber after the second ionization chamber (I_{ref}).[90] Transmission experiments are normally collected in air for hard X-ray experiments and collected in ultra-high vacuum in soft X-ray experiments.[90] The reason for this is attenuation of the beam due to absorption by O and N at lower X-Ray energies.[90] In fluorescence mode, a detector is located perpendicular to the photon path at the sample holder.[90] Fluorescence can be the preferred detection mode over transmission when the element that is being probed is in low concentration and for samples that are too thin/thick.[89,90] Total electron yield is a measure of the total amount of electrons that are ejected from a sample including photoelectrons, auger electrons, and secondary electrons.[90] Total electron yield is surface sensitive since the interaction between the electrons and the sample will cause scattering of the electrons resulting in only the electrons originating close to the surface to be detected.[89]

1.12 Thesis Objectives

The two-step method for synthesizing glass-ceramic composite materials is currently the most appropriate method to synthesize nuclear waste forms; however, the separate synthesis of the ceramic and glass phases makes this method take days to complete and requires repeated exposure to the nuclear waste.[32] A suitable substitute synthesis method for glass-ceramic composite materials should therefore be as simple as possible so that the nuclear waste does not need to be handled multiple times and be chemically comparable to glass-ceramic composite materials synthesized by the two-step method. The main objectives of this thesis work were to synthesize,

analyze, and compare glass-ceramic composites synthesized using one-step methods. The materials synthesized for this work are rare-earth phosphate-borosilicate glass composites.

The primary objective of Chapter 2 was to synthesize rare-earth phosphate-borosilicate glass ($REPO_4$-BG) composite materials by a one-step ceramic method. Glass-ceramic composite materials synthesized by the two-step ceramic method were compared to composite materials synthesized by the one-step ceramic method. The targeted crystal phase was either $LaPO_4$ or YPO_4 which allowed the study of both monazite and xenotime crystal structures when they are incorporated into a glass matrix. The annealing temperature in the one-step ceramic method was lowered while keeping the annealing time at 3 days until partial crystallization of the glass was observed to have a significant effect on the glass structure. The annealing time was lowered while keeping the annealing temperature at 1100 ^oC to demonstrate the shorter annealing times that are possible using the one-step ceramic method.

The primary objective in Chapter 3 was to develop a one-step coprecipitation method for the synthesis of glass-ceramic composite materials. This would be useful as a solution-based method would be compatible with a liquid waste stream. This was achieved by synthesizing $LaPO_4$-BG and $CePO_4$-BG composite materials. The effect of annealing temperature on the formation of the $LaPO_4$-BG and $CePO_4$-BG composite materials was also investigated.

The glass-ceramic composite materials were analyzed using a combination of powder X-ray diffraction, electron microscopy, and X-ray absorption spectroscopy. Powder X-ray diffraction allowed for the identification and analysis of crystalline phases present within the composite materials. Electron microscopy was used to observe the morphology and elemental distribution of the composite materials. X-ray absorption spectroscopy was used to probe the local chemical environment of La/Y, P, and Si as well as the relative amounts of Ce oxidation states in the composite materials.

Chapter 2 A One-Step Synthesis of Rare-Earth Phosphate-Borosilicate Glass Composites[1]

2.1 Introduction

Three potential material classes that have attracted attention for the sequestration of high-level nuclear waste are: glasses; ceramics; and glass-ceramic composites.[2,14–16] Glass-ceramic composites capitalize on the advantages of both the glass and ceramic.[2,29] The ceramic crystallites can incorporate actinides into the crystal structure giving the material a high waste loading potential as well as a high chemical resistance and the glass acts as a secondary barrier for the actinides while also being able to accommodate smaller fission products.[2,9,29]

Glass-ceramic composites containing rare-earth phosphates in a glass matrix have been proposed as a potential waste form to sequester high level nuclear waste.[32,95] Borosilicate glass (BG) is one proposed type of glass to be used for this application because of the chemical durability of this material and the prospect of recycling glass from other industries.[96] Natural rare-earth phosphates ($REPO_4$) have been found to incorporate U and Th while remaining crystalline over geological timescales.[13,54] Anhydrous rare-earth phosphates can adopt the monazite or xenotime structures which are described in Section 1.6.[55–57]

Glass-ceramic composite materials are normally synthesized using a multistep process. One type of synthesis involves a two-step method where the ceramic and glass phases are synthesized separately before being mixed and then annealed to form a composite material.[2,19,29,41,50,97,98] The high level waste stream would be added during the production of the ceramic phase which would ensure all the minor actinides would be partitioned into the ceramic phase.[41] A one-step method is investigated here where all precursors are mixed together from the beginning followed by annealing. A one-step method would have various advantages over a two-step method. For example, a one-step method would save on fabrication costs and be compatible with already existing glass producing infrastructure due to being able to form the glass-ceramic composite by the same melt-quench technique used to make glass.[30] Additionally, the production

[1] Reprinted in part from RSC Advances, G. Donato, D. Holzcherer, J. C. Beam, A. P. Grosvenor. *RSC Adv.*, 2018, **8**, 39053-39065

of glass-ceramic composite waste forms by this method would be safer since the high-level waste would not need to be handled for as long a period. The partitioning of a complex waste stream into the ceramic and glass phases is outside the scope of this chapter; however, it is envisioned that the high-level waste stream would be incorporated during the single step reaction similar to the process used to make a glass waste form.[82] The partitioning of the rare-earths in this simplified system can be inferred by looking at the solubility of the ceramic crystallites. Glass-ceramic composites containing $LaPO_4$ (monazite-type, space group $P2_1/n$, see section 1.6) or YPO_4 (xenotime-type, space group $I4_1/amd$, see section 1.6) crystallites dispersed in a borosilicate glass matrix were studied using powder X-ray diffraction (XRD), electron microprobe, and X-ray absorption near edge spectroscopy (XANES) to study the long-range order, morphology, and local chemical environment, respectively.

2.2 Experimental

2.2.1 Synthesis

The general synthesis strategies for synthesizing $LaPO_4$-BG composites made by the one- and two-step methods are shown in Scheme 1.

2.2.1.1 Two-Step Glass-Ceramic Composite Synthesis

2.2.1.1.1 $REPO_4$

$LaPO_4$ (monazite) was prepared using the ceramic method. La_2O_3 (Alfa Aesar; 99.9%) and $NH_4H_2PO_4$ (Alfa Aesar; 99.9%) were ground and mixed stoichiometrically before being pressed into a pellet and annealed at 1100 ^oC for 6 days in an alumina crucible with grinding and pelleting occurring in 3-day intervals followed by quench cooling in air. In order to obtain pure phase xenotime, YPO_4 (xenotime) was synthesized using a wet chemical method that was described previously by Kijkowska et al.[99] Powdered Y_2O_3 (Alfa Aesar 99.9%) was added to 13.7 mL of 85 vol% H_3PO_4 and stirred to make a solution with a mole ratio of 1:100 (Y_2O_3:PO_4^{3-}). The solution was then diluted by adding 100 mL of distilled water. After the water was added, the solution was refluxed at 130 ^oC for 2 hours and the precipitate was filtered and washed using distilled water. The precipitate was dried in a fumehood overnight before being pressed into a pellet and annealed at 1100 ^oC for 3 days in an alumina crucible followed by quench cooling in air.

Scheme 2.1: General synthesis of $LaPO_4$-BG composites using one- and two-step synthesis methods**.**

2-Step Method

1st step

$$La_2O_{3(s)} + 2NH_4H_2PO_{4(s)} \xrightarrow[6\ days]{1100\ ^oC} 2LaPO_{4(s)}$$

$$SiO_{2(s)} + B_2O_{3(s)} + Na_2O_{(s)} + CaO_{(s)} \xrightarrow[1\ hr]{1100\ ^oC} BG_{(s)}$$

2nd step

$$LaPO_{4(s)} + BG_{(s)} \xrightarrow[3\ days]{1100\ ^oC} LaPO_4\text{-}BG_{(s)}$$

1-Step Method

$$La_2O_{3(s)} + NH_4H_2PO_{4(s)} + SiO_{2(s)} + B_2O_{3(s)} + Na_2O_{(s)} + CaO_{(s)} \xrightarrow[1\ -\ 3\ days]{1100\ ^oC} LaPO_4\text{-}BG_{(s)}$$

2.2.1.1.2 Borosilicate glass

Borosilicate glass was also made by the ceramic method. The mole percentage was as follows: 63.5% SiO_2 (EMD Millipore), 16.9% B_2O_3 (Alfa Aesar; 99.98%), 16.5% Na_2O (Alfa Aesar), and 3.1% CaO (Acros Organics; 97+%). The oxide powders were ground and mixed using a mortar and pestle, pressed into a pellet at 6 MPa, and annealed in 5% Au/ 95% Pt crucibles, to avoid the glass sticking to the crucible, at 1100 ^oC for 1 hour followed by quench cooling in water. The glass-containing materials were quenched in water to achieve high cooling rates that favour glass formation.[38]

2.2.1.1.3 $REPO_4$-BG composite

The two-step glass-ceramic composites were formed by grinding and mixing the pure ceramic and glass with 20, 40 or 50 wt% ceramic loading to make $LaPO_4$-BG or YPO_4-BG composite materials. The 20 and 40 wt% ceramic composites were annealed in 5% Au/ 95% Pt crucibles at 1100 ^oC for 3 days followed by quench cooling in water. The 50 wt% ceramic $LaPO_4$-BG composite made by the two-step method was annealed for 1 hour at 1100 ^oC after grinding and mixing the pure ceramic and glass followed by quench cooing in water. The total synthesis time of $REPO_4$-BG composites by the two-step method was 6-9 days (6 and 3 days for the synthesis of $LaPO_4$ and YPO_4, respectively, plus 3 days to form the composite) The glass-ceramic composite materials made by the two-step method are described in Table 2.1.

2.2.1.2 One-Step Glass-ceramic Composite Synthesis

The one-step glass-ceramic composite materials were synthesized using the ceramic method and the same precursors for the $REPO_4$ and BG phases as for the two-step synthesis method (see Section 2.1.1). The precursors were proportioned to give the glass-ceramic composite a theoretical ceramic loading of 20, 40, or 50 wt%. The stoichiometry of the glass forming and glass modifying oxides were the same as the pure glass made in the two-step synthesis (mole percentage was 63.5% SiO_2, 16.9% B_2O_3, 16.5% Na_2O, 3.1% CaO). The reagents were ground, mixed and annealed in 5% Au/ 95% Pt crucibles for 1-3 days at annealing temperatures ranging from 900 to 1100 ^oC followed by quench cooling in water. The total synthesis time of the one-step method was between 1-3 days. The glass-ceramic composite materials made by the one-step method are also described in Table 2.1.

Table 2.1: Sample names and compositions of the glass-ceramic composites studied.

Sample Name	Composition (RE = La, Y)	Synthesis Method	Annealing Time	Annealing Temperature (°C)
20% 2-step	20 wt% ceramic $REPO_4$-BG	two-step	3 days	1100
40% 2-step	40 wt% ceramic $REPO_4$-BG	two-step	3 days	1100
50% 2-step	50 wt% ceramic $REPO_4$-BG	two-step	1 hour	1100
20%1-step	20 wt% ceramic REPO4-BG	one-step	3 days	1100
40% 1-step	40 wt% ceramic REPO4-BG	one-step	3 days	1100
50% 1-step	50 wt% ceramic REPO4-BG	one-step	3 days	1100
1100 C	40 wt% ceramic REPO4-BG	one-step	3 days	1100
1000 C	40 wt% ceramic REPO4-BG	one-step	3 days	1000
900 C	40 wt% ceramic REPO4-BG	one-step	3 days	900
3 days	40 wt% ceramic REPO4-BG	one-step	3 days	1100
2 days	40 wt% ceramic REPO4-BG	one-step	2 days	1100
1 day	40 wt% ceramic REPO4-BG	one-step	1 day	1100

2.2.2 Powder X-ray Diffraction

Powder X-ray diffraction patterns were collected using a PANalytical Empyrean instrument equipped with a Co or Cu $K\alpha_{1,2}$ source or a Rigaku instrument equipped with a Cu $K\alpha_{1,2}$ source. The patterns collected using the Co X-ray source were converted to the equivalent 2θ if a Cu source was used using the Bragg equation for consistency. Patterns were analyzed using the Powder Cell for Windows (PCW) software program.[100]

2.2.3 Electron Microprobe

Electron microprobe images were collected from the 50 wt% ceramic $LaPO_4$-BG composites synthesized by the 1 and two-step methods as well as the 40 wt% ceramic YPO_4-BG composites synthesized by the 1 and two-step methods. Backscattered electron (BSE) images and electron dispersive X-ray spectroscopy (EDX) maps as well as EDX spectra were collected using a JEOL 8600 electron microprobe instrument. The samples were prepared by polishing the surface using diamond paste and were coated in carbon to reduce charging effects. The images and maps were collected using a magnification of 1000X.

2.2.4 XANES

2.2.4.1 La L_{1-} and Y K-edge XANES Spectra

The La L_{1-} and Y K-edge XANES spectra were collected using the Sector 20 bending magnet (20BM) beamline located at the Advanced Photon Source (APS), Argonne National Laboratory.[101] The La L_{1-}edge XANES spectra were collected from $LaPO_4$ and the glass-ceramic composites synthesized by the one and two-step methods having a 20, 40 and 50 wt% ceramic loading. The Y K-edge XANES spectra were collected from YPO_4 and the one- and two-step glass-ceramic composites with ceramic loadings of 20 and 40 wt%. Samples were prepared by brushing finely ground powders on Kapton tape followed by folding the tape to produce multiple layers. The thickness was varied to maximize the absorption edge by adding or removing layers. Spectra were collected in transmission mode using a Si (111) double crystal monochromator, which provides a photon flux of ~10^{11} photons per second.[101] The spectral resolution of the La L_{1-}edge XANES spectra was 0.6 eV at 6266 eV and the spectral resolution of the Y K-edge XANES spectra was 2.0 eV at 17038 eV.[101] The La L_{1-}edge XANES spectra were collected using a step size of 0.15 eV through the absorption edge. The ratio of He:N_2 in the ionization chambers during collection of the La L_{1-}edge XANES spectra was 70% He:30% N_2 in the I_0 chamber and 100% N_2

in the I_t and I_{ref} chambers. The La L_1-edge XANES spectra were calibrated by collecting a Cr K-edge XANES spectrum from Cr metal foil and setting the first derivative of the absorption edge to 5989 eV.[102] The Y K-edge XANES spectra were collected using a step size of 0.3 eV through the absorption edge. The ratio of Ar:N_2 in the ionization chambers during the collection of the Y K-edge spectra was 100% N_2 in I_0 and 50% Ar: 50% N_2 in I_t and I_{ref}. The Y K-edge XANES spectra were calibrated by collecting a Zr K-edge XANES spectrum from Zr metal foil and setting the first derivative of the absorption edge to 17998 eV.[102] All XANES spectra were normalized, calibrated, and analysed using the Athena software program.[103]

2.2.4.2 P and Si $L_{2,3}$-edge XANES Spectra

The P and Si $L_{2,3}$-edge XANES spectra were collected using the Variable Line Spacing-Plane Grating Monochromator (VLS-PGM) beamline located at the Canadian Light Source (CLS).[93] The P and Si $L_{2,3}$-edge XANES spectra were collected from $LaPO_4$-BG and YPO_4-BG composite materials containing 20 and 40 wt% ceramic and synthesized using either the one-step or two-step method. P $L_{2,3}$-edge XANES spectra were also collected from the pure $LaPO_4$ and YPO_4 ceramics while Si $L_{2,3}$-edge XANES spectra were collected from the pure BG material. Samples were prepared by brushing finely ground powder on carbon tape. Spectra were measured under ultra-high vacuum in total fluorescence yield (TFY) mode using a step size of 0.05 eV through the absorption edge. The high energy grating monochromator was used to collect both spectra. The spectral resolution of the P $L_{2,3}$- and Si $L_{2,3}$-edge XANES spectra is 0.01 eV.[93] The P $L_{2,3}$-edge spectra were calibrated by collecting a P $L_{2,3}$-edge spectrum from red phosphorous and setting the first derivative of the absorption edge to 130 eV.[102] The Si $L_{2,3}$-edge spectra were calibrated by collecting a Si $L_{2,3}$-edge spectrum from elemental Si powder and setting the first derivative of the absorption edge to 100 eV.[102]

2.3 Results and Discussion

2.3.1 Formation of $REPO_4$-BG Composite Materials

2.3.1.1 $LaPO_4$-BG Composites

Powder XRD was used to characterize any crystalline phases present in the glass-ceramic composites made by the one- or two-step method. These materials consist of a glass matrix and ceramic crystallites; as such some powder XRD patterns were observed to contain broad humps representative of the glass phase in the glass-ceramic composite materials.

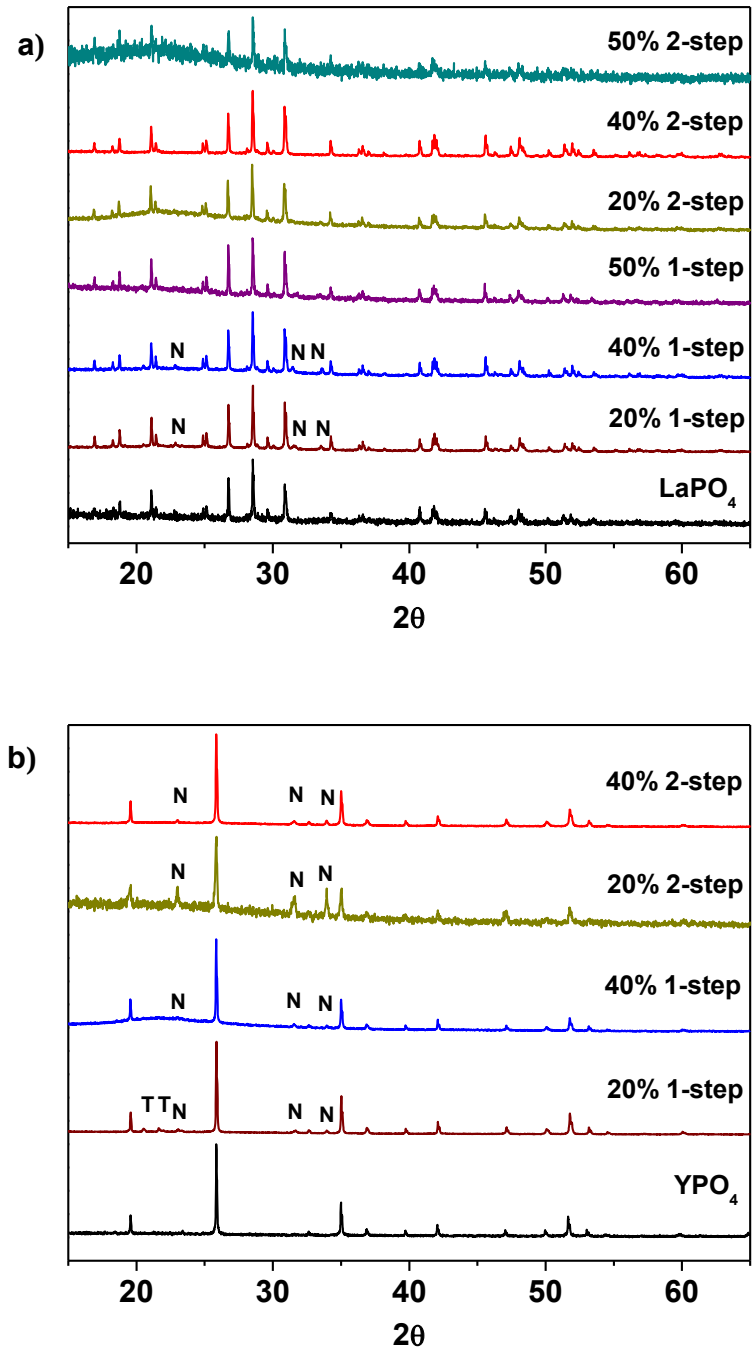

Figure 2.1: XRD patterns from (a) one- and two-step $LaPO_4$-BG composites with 20, 40 and 50 wt% ceramic and (b) one- and two-step YPO_4-BG composites with 20 and 40 wt% ceramic. T = tridymite peaks, N = nagelschmidtite phase peaks.

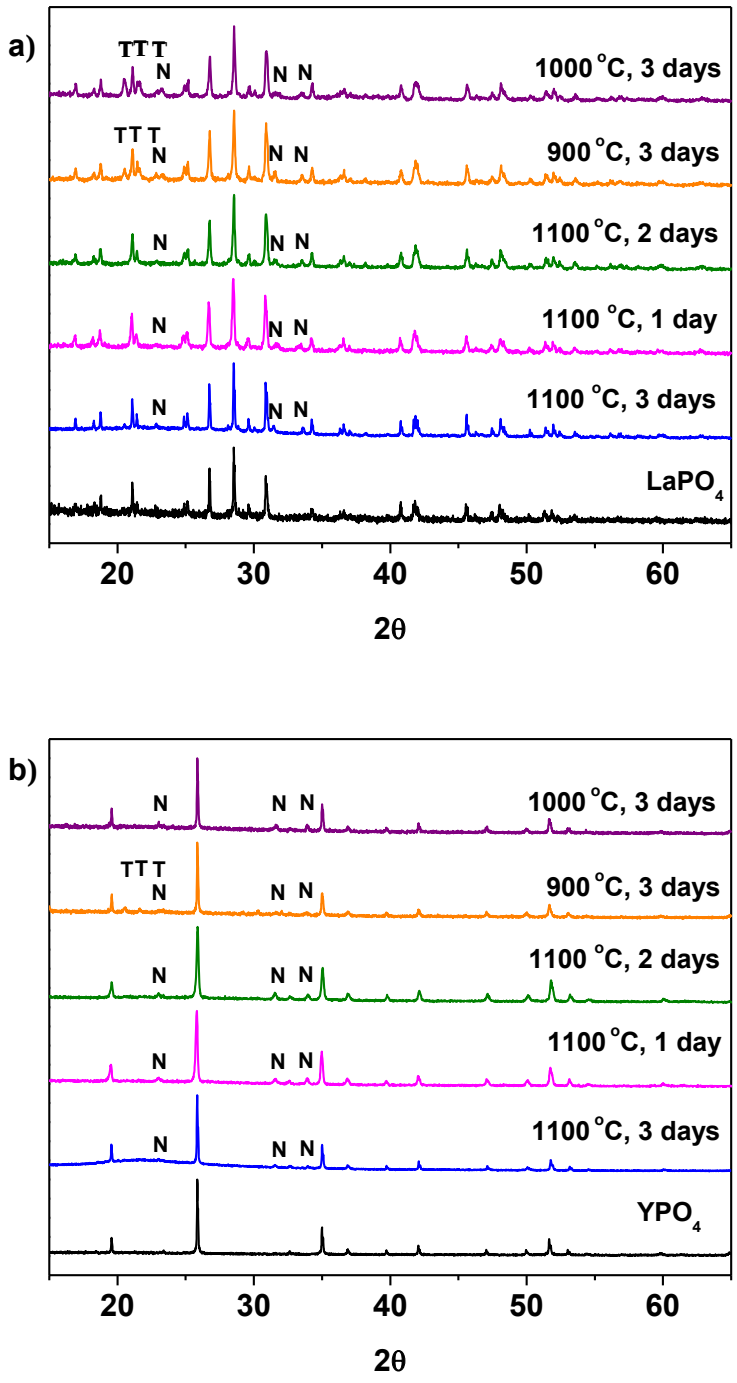

Figure 2.2: XRD patterns from (a) one-step $LaPO_4$-BG composites annealed at 900-1100 ºC and one-3 days and (b) one-step YPO_4-BG composites annealed at 900-1100 ºC and 1-3 days. T = tridymite peaks, N = nagelschmidtite peaks.

The powder XRD patterns from the $LaPO_4$-BG composites containing a 20, 40 or 50 wt% ceramic loading and made by the one- and two-step methods followed by annealing at 1100 ^oC are presented in Figure 2.1a. The major crystal phase present in all $LaPO_4$-BG composites was $LaPO_4$.[105] This demonstrates that in the one-step synthesis, La^{3+} and PO_4^{3-} formed a ceramic phase (at least primarily) instead of being incorporated into the glass matrix. Nagelschmidtite ($Ca_{7-x}Na_x(PO_4)_{2+x}(SiO_4)_{2-x}$) was also observed to be present in the powder XRD patterns from the 20 and 40 wt% ceramic composites that were synthesized using the one-step synthesis method and was caused by the glass partially crystallizing. Nagelschmidtite, however, was not observed in the powder XRD pattern from the 50 wt% $LaPO_4$-BG composite made by the one-step method, which is likely a result of the high ceramic loading of this material and the expected low concentration of nagelschmidtite.

The effect of changing the annealing temperature and annealing time on the crystal structure of the ceramic phase(s) was also investigated. The composites made by the one-step method were synthesized at 1100 ^oC for 1, 2 and 3 days to observe how the structure changed depending on the annealing time. Figure 2.2a shows the powder XRD patterns from the 40% $LaPO_4$-BG composites annealed for 1, 2, and 3 days. Annealing for 1, 2, and 3 days at 1100 ^oC forms a composite which contains $LaPO_4$ as the major phase and nagelschmidtite as the minor phase. An annealing time of one day is a much shorter time period to form monazite when compared to the 6 days it typically takes to form the pure ceramic at this temperature using the ceramic method.[14] The decrease in time can be attributed to the glass being in a liquid phase at this temperature.[105] This increases the mobility of the RE^{3+} and PO_4^{3-} ions and allows them to diffuse through the sample and form monazite in a much shorter time.

The effect of annealing temperature on the formation of the glass-ceramic composites was also investigated by synthesizing glass-ceramic composites using annealing temperatures of 1100, 1000, and 900 ^oC for 3 days. Below 1100 ^oC, $LaPO_4$, tridymite (crystalline SiO_2), and nagelschmidtite were observed to form (Figure 2.2a). The presence of crystalline SiO_2 is unwanted in a waste form and should be avoided because crystalline SiO_2 can undergo phase transformations at low temperatures, which leads to volume changes and the possibility of the waste form cracking.[19,20] No changes in the 2θ positions of the diffraction peaks or changes in the intensity

ratios of the diffraction peaks were observed, which suggests that little to no glass precursors were incorporated in the ceramic phase.

2.3.1.2 YPO_4-BG Composites

Powder XRD patterns from the one- and two-step YPO_4-BG composites containing 20 and 40 wt% ceramic showed that the major crystal phase was YPO_4 (Figure 2.1b).[62] Nagelschmidtite was also observed to form. The powder XRD pattern from the 40 wt% YPO_4-BG composite made by the one-step method also contained a very small amount of tridymite. Figure 2.2b shows powder XRD patterns of YPO_4-BG glass-ceramic composites annealed at 1100 ^oC for 1, 2, and 3 days. YPO_4 was observed to form after annealing for only one day along with nagelschmidtite. Lowering the annealing temperature (1100 ^oC – 900 ^oC) when synthesizing the YPO_4-BG composites (Figure 2.2b) resulted in the formation of tridymite at 900 ^oC but not at 1000 or 1100 ^oC. Tridymite can form when glass-ceramic composites are annealed below the melting point of crystalline SiO_2, which is what was observed when the annealing temperature was lowered when synthesizing both the $LaPO_4$-BG and YPO_4-BG composite materials.[106] Once again there were no changes in the 2θ positions of the diffraction peaks or changes in the intensity ratios of the diffraction peaks observed suggesting that little to no glass precursors were incorporated in the ceramic phase.

2.3.2 Morphology and Elemental Distribution

2.3.2.1 $LaPO_4$-BG Composites

Backscattered electron (BSE) microprobe images were collected from the 50 wt% ceramic $LaPO_4$-BG one- and two-step glass-ceramic composites (Figures 2.3a and 2.3e, respectively). Two distinct regions can be observed in the micrographs of the glass-ceramic composites made by the one- and two-step methods: a dark matrix that represents the borosilicate glass and bright areas that represent the $LaPO_4$ crystallites There is an additional grey area in the micrograph from the glass-ceramic composite made by the one-step method which may represent nagelschmidtite; however, this phase was not observed in the powder XRD pattern from the 50% $LaPO_4$-BG composite made by the one-step method (Figure 2.1a). The crystallites were observed to be dispersed in the glass matrix in both glass-ceramic composites (i.e., one-step vs. two-step).

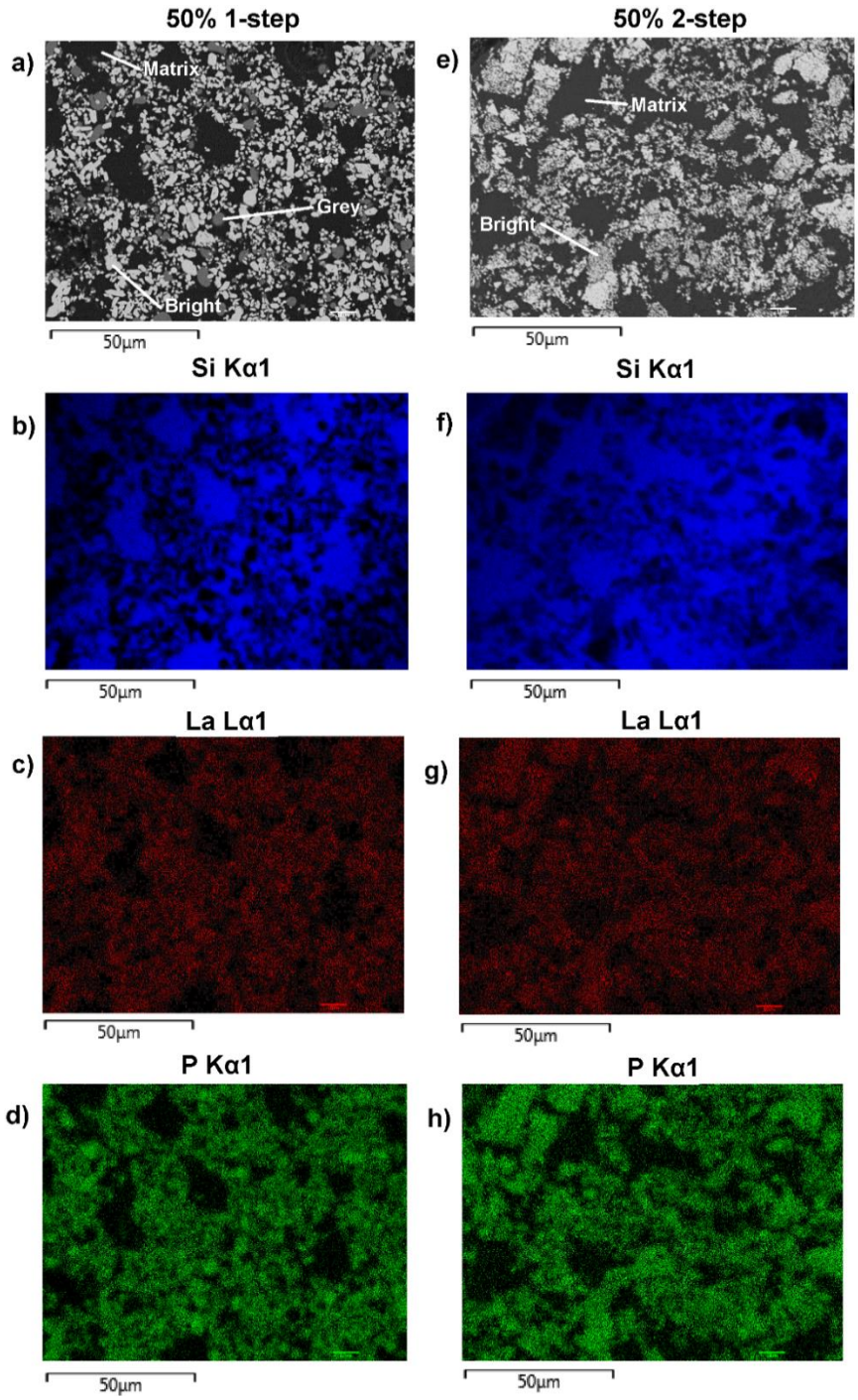

Figure 2.3: (a) Backscattered electron image of 50 wt% ceramic $LaPO_4$-BG composites synthesized by the one-step method, (b) Si EDX map of composites made by the one-step method, (c) La EDX map of composites made by the one-step method (d) P EDX map of composites made by the one-step method, (e) Backscattered electron image of 50 wt% ceramic $LaPO_4$-BG composites synthesized by the two-step method, (f) Si EDX map of composite made by the two-step method, (g) La EDX map of composite made by the two-step method (h) P EDX map of composite made by the two-step method.

A difference in crystallite size and shape between the one- and two-step glass-ceramic composites was observed, which can be explained by how the crystallites formed in the glass-ceramic composites. In the one-step method, the crystallites are formed in the glass while in the two-step method, the pure ceramic is already formed and is mechanically ground before being mixed with the glass followed by annealing. In addition, the composite made by the two-step method was only annealed for 1 hour which would not be expected to be sufficient for aggregation and crystallite growth to occur.[107]

Energy dispersive X-ray fluorescence (EDX) maps (Figure 2.3) were also collected from 50 wt% $LaPO_4$-BG composites annealed for 1 hour at 1100 ^oC to observe the elemental distribution in the different regions of the composite materials. The EDX maps from the composite material made by the one-step method showed distinct regions containing high concentrations of P and La that correspond with the bright spots observed in the BSE image (Figures 2.3d and 2.3c, respectively) while the matrix present in the BSE images showed a high concentration of Si in the corresponding EDX map (Figure 2.3b), which corresponds to borosilicate glass. The EDX maps show discrete regions containing Si or La/P, respectively, indicating that there was very little, if any, La and P dissolved in the glass matrix. The EDX maps from the composite material made by the two-step method also showed discrete regions containing La/P or and Si (Figure 2.3). The La and P EDX maps correlated with each other and correspond to the bright spots in the BSE image (cf., Figures 2.3e, 2.3g, and 2.3h). The Si EDX map correspond to the matrix in the BSE image (cf., Figures 2.3e and 2.3f). These results are similar to the results from the composite made by the one-step method and further shows the similarity in the one- and two-step glass-ceramic composites despite the different synthesis methods.

2.3.2.2 YPO_4-BG Composites

Figures 2.4a and 2.4e show BSE images from the 40 wt% YPO_4-BG composite materials made by the one- and two-step methods, respectively. These images were similar to the $LaPO_4$-BG images in that there are crystallites dispersed in a glass matrix and that the shape and size of the crystallites was observed to change depending on if the one- or two-step synthesis method was used. Three regions were observed in the micrographs: a dark matrix, grey areas, and bright areas. The matrix represents the borosilicate glass, the grey areas are likely nagelschmidtite, while the bright areas are YPO_4.

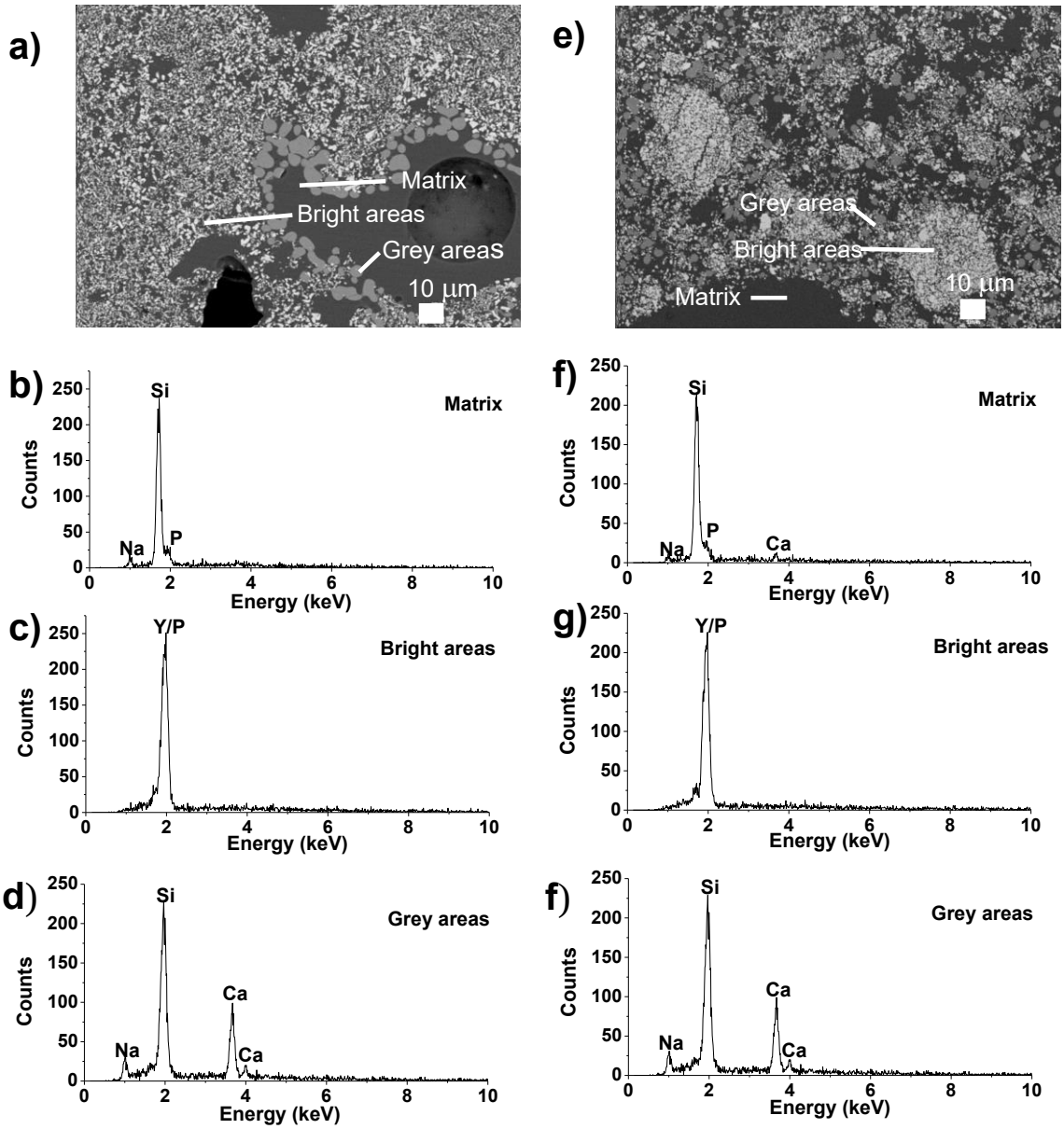

Figure 2.4: (a) Backscattered electron image of 40 wt% ceramic YPO_4-BG composites synthesized by the one-step method, (b) EDX spectra taken of the matrix in the composites made by the one-step method, (c) EDX spectra taken of the bright particles (YPO_4) in the composites made by the one-step method, (d) EDX spectra taken of the grey particles (minor crystal phase) in the composites made by the one-step method, **(**e) backscattered electron image of 40 wt% ceramic YPO_4-BG composites synthesized by the two-step method, (f) EDX spectra taken of the matrix in the composite made by the two-step method, (g) EDX spectra taken of the bright particles (YPO_4) in the composite made by the two-step method, (h) EDX spectra taken of the grey particles (minor crystal phase) in the composite made by the two-step method.

The absence of P in the spectra is surprising given the general formula of nagelshmidtite, $Ca_{7-x}Na_x(PO_4)_{2+x}(SiO_4)_{2-x}$.[108] Rare-earth elements (e.g. Nd) have also been found to stabilize the nagelshmidtite structure with higher silicon concentrations giving the general formula $Ca_{7-x}Nd_x(PO_4)_{2-x}(SiO_4)_{2+x}$ ($0 \leq x \leq 1$).[49]

A low intensity P signal in the EDX spectra could be overlapped by the large Si signal due to the proximity of the peaks and the resolution of the EDX detector used. The EDX spectra from the borosilicate glass (matrix; Figures 2.4b and 2.4f) indicate the presence of Si, Na, P (and Ca in the case of the composite material synthesized by the two-step method). This indicates that only a small amount of Ca did not crystallize into nagelschmidtite in the YPO_4-BG composite material made by the one-step method. The fluorescence signal from Y could be overlapped by the signal from P and Si in the EDX spectrum from the matrix (Figures 2.4b and 2.4f) due to the similarity in energy of the peaks and the resolution of the detector. SEM and EDX maps were also collected from the 40 wt% YPO_4-BG composite materials made by the one- and two-step methods from different spots on the samples (Figure A-1 in Appendix A). These maps suggest the presence of P and Y in the nagelschmidtite crystallite as well as the dissolution of YPO_4 in the glass matrix.

2.3.3 Local Chemical Environment

2.3.3.1 La L_1-edge XANES Spectra

The local chemical environments of the rare-earth elements in the $LaPO_4$-BG composites were examined and compared to pure $LaPO_4$ by collecting La L_1-edge XANES spectra (Figure 2.5). The La L_1-edge XANES spectrum has been shown to consist of 2 features, a pre-edge feature and a main-edge feature. The pre-edge feature occurs due to a quadrupolar, 2s → 5d transition while the main-edge feature is caused by a dipolar, 2s → 6p transition.[110] Figure 2.5a shows the La L_1-edge XANES spectra for the pure ceramic and the glass-ceramic composites with 20, 40, and 50 wt% ceramic made by the one- and two-step synthesis methods. The spectra from the glass-ceramic composites overlap with the spectrum of the pure $LaPO_4$ ceramic, indicating that La in the glass-ceramic composites is in a similar chemical environment as La found in the pure-phase ceramic. This observation is consistent with the EDX maps from these materials (Figure 2.3). The spectrum from the 20 wt% ceramic two-step glass-ceramic composite showed slight changes when compared to the rest of the spectra. These changes in the La L_1-edge XANES spectrum are likely caused by data collection/normalization issues since there is a low concentration of La in this

particular sample and that the glass-ceramic composites made by the one- and two-step methods have been observed to be very similar when comparing the results from the other characterization techniques used in this study.

The La L_1-edge XANES spectra from the glass-ceramic composite materials annealed for 1-3 days at 1100 ^oC and 1100–900 ^oC for 3 days are presented in Figure 2.5b and Figure 2.5c, respectively. All of the spectra were observed to be identical to the spectrum from the pure $LaPO_4$ ceramic. Comparison of the La L_1-edge XANES spectra (Figure 2.5) and the powder XRD patterns (Figure 2.1a and Figure 2.2a) indicate that monazite can form within the composite materials using lower annealing temperatures than are generally used to form pure $LaPO_4$ by the ceramic method and can form in as little as 1 day with little to no impact to the long-range order or local chemical environment of the $LaPO_4$ monazite structure.

2.3.3.2 Y K-edge XANES Spectra

The local chemical environment of YPO_4-BG composites was analyzed by collecting Y K-edge XANES spectra (Figure 2.6). A Y K-edge XANES spectrum consists of a pre-edge feature and a main-edge feature. The pre-edge is due to a quadrupolar, 1s → 4d transition while the main edge is a result of a dipolar, 1s → 5p transition.[110] An increase in intensity of the pre-edge along with a decrease in intensity in the main edge is indicative of a decrease in the coordination number of Y.[111] Overlap of the 4d and 5p orbitals increases when the coordination number decreases, which increases the dipolar character of the transition.[112,113,114] Figure 2.6 shows the Y K-edge XANES spectra from the glass-ceramic composites having a 20 and 40 wt% ceramic loading and made by the one- and two-step synthesis methods and are compared to the spectrum from pure YPO_4. Yttrium has been shown to have a lower coordination number when it is dissolved in a glass matrix than in the xenotime-type structure.[62,115]

The intensity of the main edge feature in the YPO_4-BG composite materials (Figure 2.6) increases while the pre-edge feature decreases in intensity as the ceramic loading increases. The Y K-edge XANES spectra were observed to overlap when comparing glass-ceramic composites formed by the one- and two-step methods having the same ceramic loading. This shows that while the intensities of the features in the XANES spectra (and as a result the local chemical environment of Y) are dependent on ceramic loading, they are independent of synthesis method.

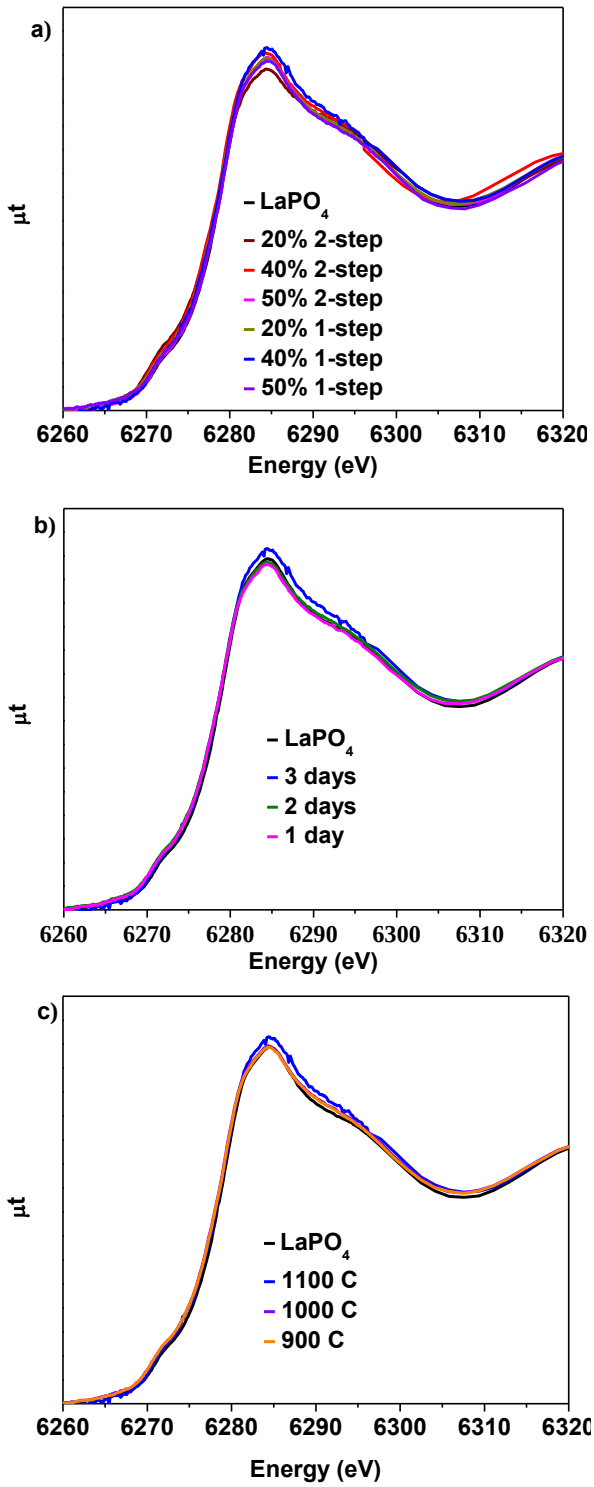

Figure 2.5: (a) La L_1-edge XANES spectra taken from one- and two-step $LaPO_4$-BG composites with 20, 40 and 50 wt% ceramic as well as pure $LaPO_4$, La L_1-edge XANES spectra taken from 40 wt% ceramic one-step $LaPO_4$-BG composites annealed at (b) 1-3 days at 1100 ^oC and (c) 900-1100 ^oC for 3 days.

The Y K-edge XANES spectra from all glass-ceramic composite materials show changes when compared to the spectrum from YPO_4, which indicates that Y adopted a lower average coordination number in these composite materials. This suggests that Y dissolved in the borosilicate glass under all conditions. The proportionate amount of Y dissolved in the glass is greater in the 20 wt% ceramic than in the 40 wt% ceramic, which indicates that YPO_4 will only dissolve and be incorporated into the borosilicate glass up to a point, with the remaining Y being found in YPO_4. More of the crystalline phase will therefore be observed when more YPO_4 is loaded into the composite material.

The difference in solubility of the rare-earth phosphates in the glass matrix between the $LaPO_4$-BG composites and the YPO_4-BG composites can be explained by examining the structural roles and field strength of the rare earth elements. Field strength is based on the theory of coulombic fields and can help predict and explain how the different cations interact with each other in glass.[116] This is done by looking at how the cations interact with and compete for O^{2-} in order to satisfy their own local chemical requirements.[116] The field strength is calculated by dividing the charge of the cation by the square of the cation-oxygen bond distance ($FS = z/a^2$).[64,117–119] Cations in a glass can be categorized as a network former, which makes up the glass network with bridging oxygen anions, a network modifier, which breaks up the network by introducing non-bridging oxygen anions, and network intermediates, which can act as either network formers or network modifiers depending on the glass composition.[120] The category a cation falls into is largely based on the field strength and the bond strength between the cation and oxygen.[1,119] Network modifiers have a general range in field strength from 0.1 to 0.4 and a typical bond strength of 10-50 kcal/mol whereas network intermediates have a field strength range of 0.5 to 1.0 and a typical bond strength of 50-70 kcal/mol while network formers have a field strength of >1.0 and bond strengths of >70 kcal/mol.[1,119]

The rare-earth ions La^{3+} and Y^{3+} have field strengths of 0.50 and 0.57, respectively, and bond strengths of 58 kcal/mol (La-O) and 50 kcal/mol (Y-O).[118,119,120] Y^{3+} has a higher field strength (0.57) than La^{3+} (0.50) due to the smaller ionic radius of Y^{3+}.[118] La^{3+} is on the edge of the field strength range between network modifiers and network intermediates and can act as a network modifier.[118]

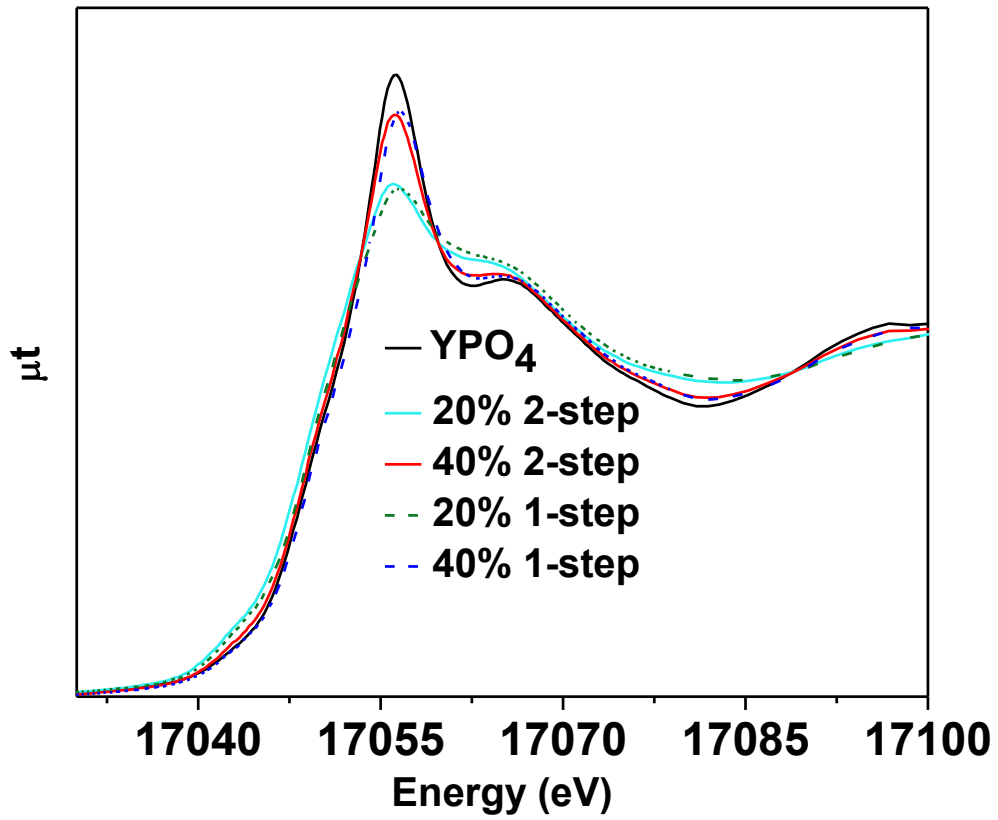

Figure 2.6: Y K-edge XANES spectra taken from one- and two-step YPO_4-BG composites with 20 and 40 wt% ceramic as well as pure YPO_4.

Y^{3+} has been shown to break up the glass network or strengthen it in silicate glasses depending on composition and therefore it has been suggested that Y^{3+} can be classified as a network intermediate.[115,122] This was also suggested to be true by Malchukova et al for Gd^{3+}, which has a similar field strength to Y^{3+} (0.55).[96] In that study, Gd was doped into aluminoborosilicate glass (0-4.4 wt% of Gd_2O_3) and exposed to radiation in order to determine how these conditions effects the potential waste form.[96] Of the amount of Gd^{3+} that was homogenously dissolved in the glass, the ratio of Gd^{3+} ions that acted as a network former and network modifier remained the same from 0.9-4.4 wt% of Gd_2O_3.[96]

By having a higher field strength, Y^{3+} is able to compete for O^{2-} more successfully than La^{3+} and behave as a network intermediate, leading to a higher degree of incorporation into the glass structure and a higher solubility in borosilicate glass. It has also been shown that crystallization is more difficult to induce in rare-earth doped borosilicate glass when Y^{3+} is the rare earth compared to when La^{3+} is present, indicating a higher stability of Y in the glass matrix caused by the difference in structural roles.[115]

2.3.3.3 P $L_{2,3}$-edge XANES Spectra

P $L_{2,3}$-edge XANES spectra were collected to study how the local chemical environment of P changed in the composite materials compared to the pure-phase ceramics. The P $L_{2,3}$-edge XANES spectra can be used to study next nearest neighbour effects in the crystallites due to distortions in the PO_4 tetrahedra affecting the spectra.[59,123] These effects can be observed due to the lifetime of the core-hole created after the excitation. The core-hole in this spectrum has a longer lifetime than the core-hole in the La L_1- and Y K-edge XANES spectra, resulting in a higher resolution.[58] The features observed in P $L_{2,3}$-edge XANES spectra result from 2p → 3s and 2p → 3d excitations. The 3s and 3d orbitals overlap in energy producing complicated transitions and spectra containing many features.[58]

2.3.3.3.1 $LaPO_4$-BG Composites

The P $L_{2,3}$-edge XANES spectra from the $LaPO_4$-BG composites and pure $LaPO_4$ are shown in Figure 2.7 and were collected to observe any changes in the local chemical environment of P in the composite materials vs. the pure-phase ceramic.

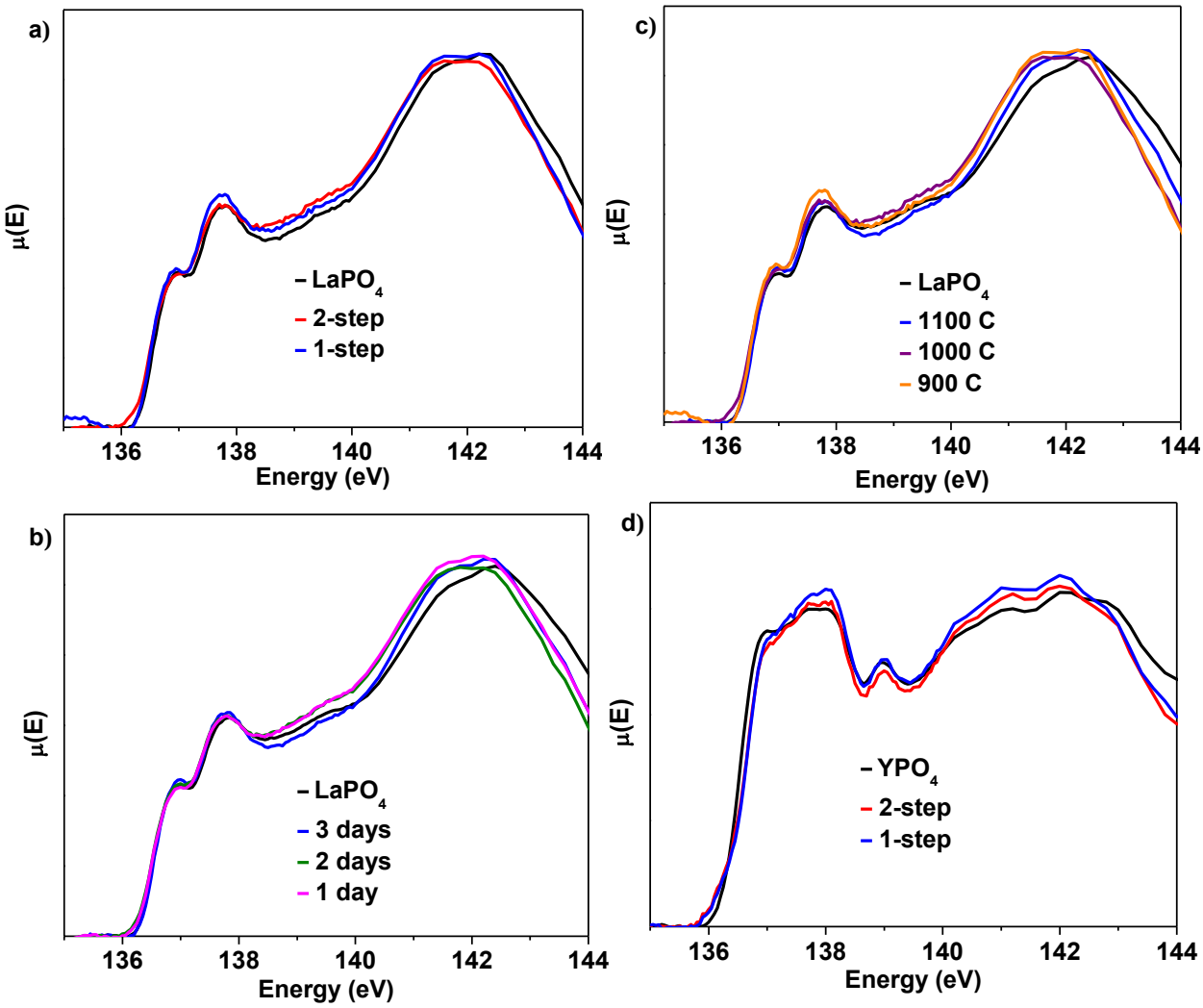

Figure 2.7: P $L_{2,3}$-edge XANES spectra of (a) one- and two-step 40 wt% ceramic $LaPO_4$-BG composites, one-step $LaPO_4$-BG composites annealed at (b) 900-1100 ^oC for 3 days, (c) 1-3 days at 1100 ^oC as well as pure $LaPO_4$ and (d) one- and two-step YPO_4-BG composites with 20 and 40 wt% ceramic as well as pure YPO_4.

The P $L_{2,3}$-edge XANES spectra from all $LaPO_4$-BG composites and $LaPO_4$ were observed to overlap, which suggests no change in the local chemical environment of P regardless of synthesis method, annealing temperature, or annealing time used to form the composite materials. Comparison of the La L_1-edge and P $L_{2,3}$-edge XANES spectra indicate that the local environment of La and P remain the same in the composite materials compared to pure $LaPO_4$. This being said, this suggestion could be questioned when the P $L_{2,3}$-edge XANES results from the YPO_4-BG composites are considered (*vide infra*).

2.3.3.3.2 YPO_4-BG Composites

The P $L_{2,3}$-edge XANES spectra from the YPO_4-BG samples (Figure 2.7d) indicate little to no change when compared to the spectrum from the pure-phase YPO_4 ceramic. This is in contrast to the results from EDX spectra (Figure 2.4) and Y K-edge XANES spectra (Figure 2.6) from the YPO_4-BG composite materials. Based on those results, some YPO_4 was concluded to be dissolved in the glass matrix from the composite materials vs. the pure phase ceramic. The similarity between the P $L_{2,3}$-edge XANES spectra despite whether P is located in the glass or ceramic phases in the composite materials suggests that the chemical environment of P is similar in the glass and ceramic phases. The examination of P $L_{2,3}$-edge XANES spectra alone is therefore not appropriate for analysis of $REPO_4$-BG composites and should be paired with other characterization techniques when analyzing $REPO_4$-BG systems.

2.3.3.4 Si $L_{2,3}$-edge XANES Spectra

Si $L_{2,3}$-edge XANES spectra were collected to examine how the synthesis conditions can affect the local structure of the glass matrix. The Si $L_{2,3}$-edge XANES spectrum is comprised of two main features. The lower energy feature results (primarily) from 2p → 3s transitions while the higher energy feature results (primarily) from 2p → 3d transitions.[124,125] Crystallization of the glass and next nearest neighbour effects are among the changes that can be observed in this spectrum.[124] When going from amorphous to crystalline SiO_2, the spectrum becomes sharper and shifts to higher energy. This is because the long-range order in crystalline SiO_2 causes the final states to be more degenerate.[2] These spectra also become narrower when metal cations are present in the glass matrix.[124] The narrowing of the spectra is caused by next nearest neighbour effects in the Si-O-M bond. The metal cation affects the bond length and covalency of the Si-O bond and will affect the spectrum as a result.[29]

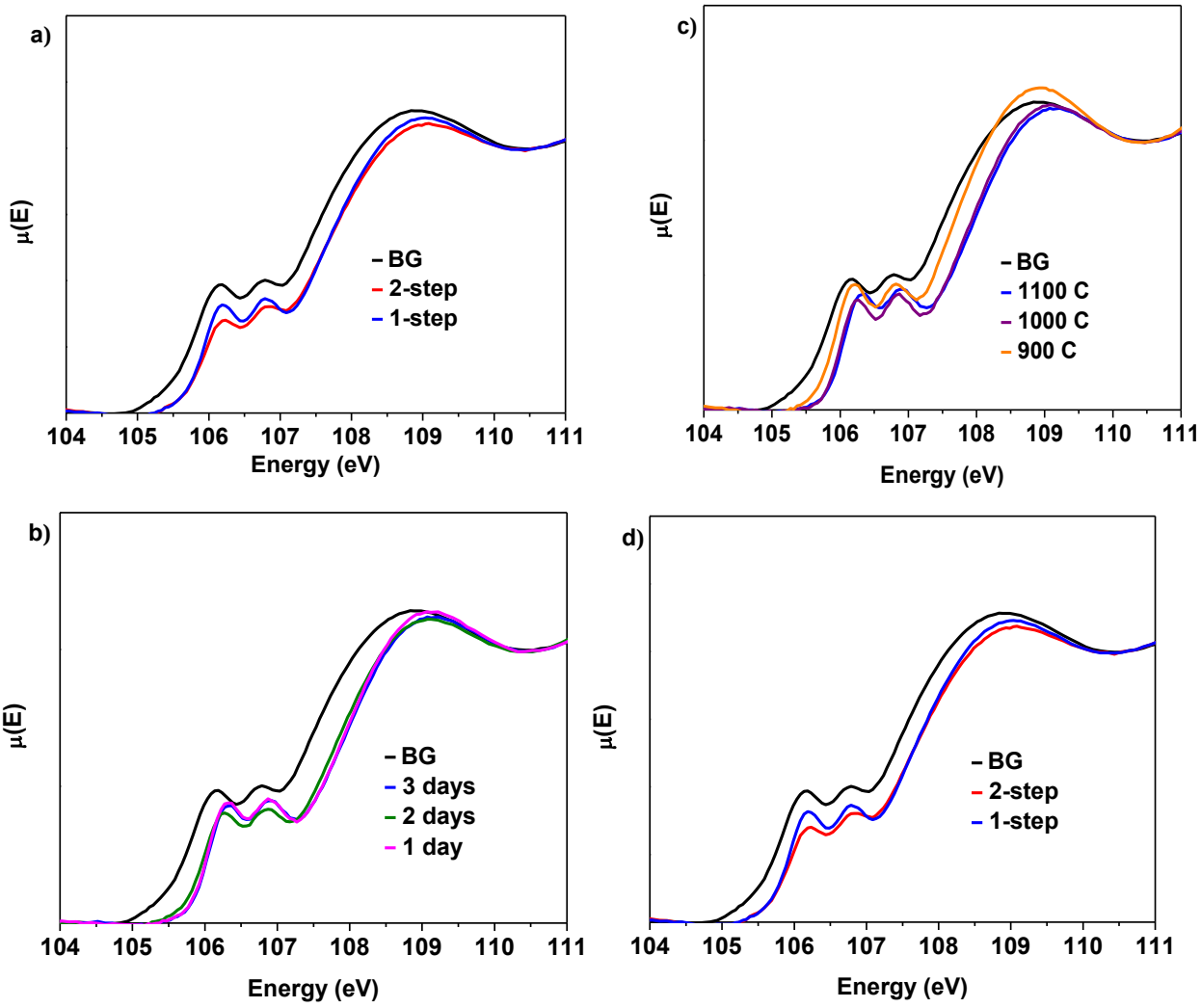

Figure 2.8: Si $L_{2,3}$-edge XANES spectra of (a) one- and two-step 40 wt% ceramic $LaPO_4$-BG composites, one-step $LaPO_4$-BG composites annealed at (b) 900-1100 ^oC for 3 days, (c) 1-3 days at 1100 ^oC and (d) one- and two-step YPO_4-BG composites with 20 and 40 wt% ceramic as well as pure BG.

2.3.3.4.1 $LaPO_4$-BG Composites

The Si $L_{2,3}$-edge XANES spectra from the $LaPO_4$-BG composites are presented in Figure 2.8. Figure 2.8a compares the spectra from $LaPO_4$-BG composites synthesized using the one- and two-step methods. The intensity ratio of the L_2 and L_3-edges change depending on the synthesis method used. These changes have been attributed to changes in the ordering of the glass.[28] The Si $L_{2,3}$-edge XANES spectra presented in Figure 2.8b overlap each other showing no significant changes in the local chemical environment of Si regardless of annealing time. The spectra presented in Figures 9a and 9b from the glass-ceramic composites are narrower and higher in energy than the spectra from borosilicate glass. The changes in the spectra between the glass-ceramic composite materials and borosilicate glass are a result of next nearest neighbour effects caused by the presence of metal cations. Figure 2.8c shows spectra from $LaPO_4$-BG composites annealed at 1100, 1000, and 900 ^oC. The Si $L_{2,3}$-edge XANES spectra from the composite materials become sharper with decreasing annealing temperature. The sharpening of the spectra is indictive of partial crystallization in the glass.[124] Powder XRD patterns from these glass-ceramic composites showed the presence of crystalline SiO_2 when they were annealed for 3 days at 1000 and 900 ^oC (Figure 2.2a). Analysis of the Si $L_{2,3}$-edge XANES spectra suggest that the amount of crystallization that occurred at 1000 ^oC was minor and did not affect the overall structure of the amorphous glass matrix in a significant way while analysis of the spectrum from the composite annealed at 900 ^oC suggested that the crystallization of SiO_2 impacted the Si network to a much greater extent.

2.3.3.4.2 YPO_4-BG Composites

The Si $L_{2,3}$-edge XANES spectra of YPO4-BG composites made by the one- and two-step synthesis methods are narrower to higher energy than the spectrum from pure borosilicate glass. These changes, like in $LaPO_4$-BG composites, are a result of next nearest neighbour effects caused by the metal cation in the Si-O-M bond except in these cases it is from Si-O-Y. When compared to each other, YPO_4-BG glass-ceramic composite materials synthesized by the one- and two-step methods show the same changes observed in the $LaPO_4$-BG composites (Section 2.3.4.1) in that the intensity ratio of the L_2 and L_3 edges changed depending on the synthesis method. The cause of the change in the glass ordering in these materials seems to be linked to the synthesis method itself and not by how much ceramic dissolves in the glass. This is because the amount of ceramic

dissolved in the glass was the same regardless of synthesis method and also this change in relative intensities was observed in the Si $L_{2,3}$-edge XANES spectra from $LaPO_4$-BG composite materials, where no dissolution took place.

2.4 Conclusions

Composite materials of rare-earth phosphate crystallites dispersed in borosilicate glass made by the one- and two-step methods were synthesized. Powder XRD, electron microprobe, and XANES have been utilized to examine the long-range order, morphology, chemical distribution, and local environment of glass-ceramic composites formed using either a one- or two-step method. Glass-ceramics composite materials made by the one- and two-step method showed either $LaPO_4$ or YPO_4 as the major crystal phase depending on the rare earth oxide used. All other characterization techniques showed one- and two-step composites containing the same rare-earth ion were similar to each other except by Si $L_{2,3}$-edge XANES. The change in the relative intensities of the Si L_2 and L_3-edge are indicative of a change in the ordering in the glass as a result of the new synthesis method (i.e., one-step).

Glass-ceramic composite materials were also able to be synthesized in 1 day at 1100 ^oC and in 3 days at 1000 ^oC without any significant change in the glass or ceramic phases relative to the composite material synthesized for 3 days at 1100 ^oC. Different solubilities of $LaPO_4$ and YPO_4 in borosilicate glass were observed due to the different field strength of the rare earth ion present in the composite material. This difference in field strength lead to a difference in structural roles of La^{3+} (network modifier) and Y^{3+} (network intermediate). Ceramic crystallites dissolving in the glass matrix within a glass-ceramic composite waste form would minimize the inherent strengths of this class of waste form such as increased chemical stability and a double barrier (ceramic+glass). Consideration of the field strength of the ions used must be accounted for when synthesizing this system for nuclear waste sequestration applications. The one-step synthesis method has shown potential as a synthetic strategy to prepare glass-ceramic nuclear waste forms.

Chapter 3 Crystallization of Rare-Earth Phosphate-Borosilicate Glass Composites Synthesized by a One-Step Coprecipitation Method

3.1 Introduction

Chapter 2 demonstrated that it is possible to synthesize $REPO_4$-BG composite materials by a one-step ceramic method at annealing temperatures as low as 1000 ^oC while being chemically similar to composite materials synthesized by a two-step method. The natural progression of this research is to develop a one-step coprecipitation synthesis method to reach even lower annealing temperatures and account for high-level nuclear waste that can be in a liquid state. Synthesizing $REPO_4$-BG composite materials by a coprecipitation method would also allow the versatility of the one-step method to be analyzed by comparing the results of this chapter to the results from Chapter 2.

Composite materials consisting of rare-earth phosphates dispersed in a glass matrix have been proposed as a nuclear waste form and have been studied in the past.[32,95,126] Borosilicate glass (BG) is able to incorporate a large variety of waste elements into its amorphous structure.[25,51] Borosilicate glass is also more thermally stable and less soluble in aqueous conditions than other prospective glasses (see Section 1.7).[25,51] These properties make it a useful glass matrix in composite waste form materials and borosilicate glass has also been adopted as the benchmark glass waste form.[50,96] Monazite ($REPO_4$; RE = La – Gd) has been proposed as a suitable structure for the sequestration of actinides and rare-earth elements found in high-level nuclear waste.[14,24,95] This is due to natural samples being found with 15 wt% of U while still remaining crystalline over geological time scales.[13,54,96] See section 1.6 for a description of the monazite crystal structure. Another important property of a potential waste form is the solubility of the material in water.[48] Monazite has been shown to be chemically durable in aqueous environments with a low normalized leech rate and little to no changes in the local or long-range structure of the material even after prolonged exposure.[48]

Glass-ceramic composite materials can be made using the standard ceramic method where the dry precursor powders are ground together, pressed into a pellet, and annealed at high

temperatures.[127] Glass-ceramic composite materials can also be made using the coprecipitation method where the precursors are dissolved in a solvent followed by precipitation and annealing.[128] The coprecipitation method mixes the precursors more intimately which lowers the diffusion distance of the ions and allows for lower annealing temperatures to be used when compared to the ceramic method.[78]

The objective of this chapter was to synthesize $REPO_4$-BG composite materials (discussion on $REPO_4$ and BG materials can be found in Sections 1.6 and 1.7) using a one-step coprecipitation method and to investigate the effect of different synthesis conditions on the structure and morphology of the materials. This included: the rare-earth element used (La or Ce); annealing temperature; ceramic loading; and oxidation state of the Ce precursor. The chemistry of actinides (a major component of high-level waste) such as Pu can be studied using actinide surrogates such as Ce.[71,128] The crystallization, morphology, local chemical environment, and differences in the oxidation states were all able to be observed by use of powder X-Ray diffraction, scanning electron microscopy, energy dispersive X-Ray spectroscopy, and X-Ray absorption near-edge spectroscopy.

3.2 Experimental

3.2.1 Synthesis

3.2.1.1 $REPO_4$

Rare-earth phosphates were synthesized using a coprecipitation method. $La(NO_3)_3 \cdot 6H_2O$ (Alfa Aesar 99.9%) was used as the source of La^{3+} to make $LaPO_4$. $Ce(NO_3)_3 \cdot 6H_2O$ (Alfa Aesar 99.5%) was used as a Ce^{3+} precursor to make $CePO_4$ [Ce(III)] and $(NH_4)_2Ce(NO_3)_6$ (Alfa Aesar 99.5%) was used as a Ce^{4+} precursor to make $CePO_4$ [Ce(IV)]. (The label in square brackets indicate the oxidation state of the Ce precursor used.) The appropriate rare-earth nitrate and $NH_4H_2PO_4$ (Alfa Aesar 99.9%) were dissolved in distilled water followed by mixing. A precipitate immediately formed following mixing. The precipitate was filtered using ashless filter paper followed by heating at 650 ^oC to burn off the filter paper. The resulting powders were pressed into a pellet at 6 MPa and annealed at either 1100 ^oC or 700 ^oC in an alumina crucible followed by quench cooling in air.

3.2.1.2 Borosilicate Glass (BG)

Borosilicate glass was synthesized using a coprecipitation synthesis method. Tetraethyl orthosilicate (Alfa Aesar 99.9%), H_3BO_3 (Alfa Aesar 99+%), Na_2O (Alfa Aesar), and $Ca(NO_3)_2 \cdot 4H_2O$ (Sigma-Aldrich $\geq$99.0%) were dissolved in 15 mL of distilled water mixed with 5 mL of ethanol and mixed. The molar ratio of precursors for the borosilicate glass was 63.5% SiO_2, 16.9% B_2O_3, 16.5% Na_2O, and 3.1% CaO. $NH_4OH_{(aq)}$ was added following mixing to raise the pH of the solution to ~10 which caused a precipitate to form. The mixed powder was obtained by evaporating the solvent at 120 ^oC. The homogenous powder was heated in an alumina crucible at 500 ^oC for 2 hours to ensure there were no nitrates present in the sample before high-temperature annealing. The precursor powder was then pressed into a pellet at 6 MPa and heated from 600 to 1100 ^oC at 100 ^oC/hour and held at 1100 ^oC for one hour in a 5%Au/95%Pt crucible. The glass was quenched in water to ensure rapid cooling so as to prevent crystallization.

3.2.1.3 $REPO_4$-BG glass-ceramic composites

Rare-earth phosphate-borosilicate glass ($REPO_4$-BG) composites were synthesized in one-step using a coprecipitation method. $La(NO_3)_3 \cdot 6H_2O$ was used as the source of La^{3+} to make $LaPO_4$-BG composites, $Ce(NO_3)_3 \cdot 6H_2O$ was used as a Ce^{3+} precursor to make $CePO_4$-BG [Ce(III)] composites, and $(NH_4)_2Ce(NO_3)_6$ was used as a Ce^{4+} precursor to make $CePO_4$-BG [Ce(IV)] composites. $NH_4H_2PO_4$, tetraethyl orthosilicate, H_3BO_3, Na_2O, $Ca(NO_3)_2 \cdot 4H_2O$ and the appropriate rare-earth nitrate were dissolved in 15mL of distilled water mixed with 5mL of ethanol and mixed. The ratio in which the precursors were added was such that the glass-ceramic composite material would have either 20 wt% $REPO_4$ and 80 wt% glass or 40 wt% $REPO_4$ and 60 wt% glass. The glass composition was the same as the borosilicate glass composition described in Section 3.2.1.2. A precipitate was observed following mixing and more precipitate formed after addition of NH4OH(aq) to raise the pH of the solution. A mixture of all precursors was obtained by evaporating the solvent at 120 ^oC. The powder was heated in an alumina crucible at 500 ^oC for 2 hours to ensure there were no nitrates present in the sample before high-temperature annealing. The precursor powder was then pressed into a pellet at 6 MPa and annealed for 3 days at temperatures ranging from 700 to 1100 ^oC in a 5%Au/95%Pt crucible.

Table 3.1: Compositions and annealing temperatures of all $REPO_4$-BG composite materials presented.

Composition/Label	RE Precursor	Annealing Temperature (ºC)
40 wt% $LaPO_4$-BG	La^{3+}	1100
20 wt% $LaPO_4$-BG	La^{3+}	1100
40 wt% $LaPO_4$-BG	La^{3+}	900
40 wt% $LaPO_4$-BG	La^{3+}	800
40 wt% $LaPO_4$-BG	La^{3+}	700
20 wt% $LaPO_4$-BG	La^{3+}	700
40 wt% $CePO_4$-BG [Ce(III)]	Ce^{3+}	1100
20 wt% $CePO_4$-BG [Ce(III)]	Ce^{3+}	1100
40 wt% $CePO_4$-BG [Ce(III)]	Ce^{3+}	1000
40 wt% $CePO_4$-BG [Ce(III)]	Ce^{3+}	900
40 wt% $CePO_4$-BG [Ce(III)]	Ce^{3+}	800
40 wt% $CePO_4$-BG [Ce(III)]	Ce^{3+}	700
20 wt% $CePO_4$-BG [Ce(III)]	Ce^{3+}	700
40 wt% $CePO_4$-BG [Ce(IV)]	Ce^{4+}	1100
20 wt% $CePO_4$-BG [Ce(IV)]	Ce^{4+}	1100
40 wt% $CePO_4$-BG [Ce(IV)]	Ce^{4+}	1000
40 wt% $CePO_4$-BG [Ce(IV)]	Ce^{4+}	900
40 wt% $CePO_4$-BG [Ce(IV)]	Ce^{4+}	800
40 wt% $CePO_4$-BG [Ce(IV)]	Ce^{4+}	700
20 wt% $CePO_4$-BG [Ce(IV)]	Ce^{4+}	700

All glass-ceramic composite materials were quenched in water to ensure rapid cooling so as to limit crystallization of the glass. Table 3.1 presents the compositions of the glass-ceramic composite materials studied and the synthesis conditions used to form them.

3.2.2 Powder X-Ray Diffraction

Powder X-ray diffraction patterns were collected using a PANalytical Empyrean instrument or a Rigaku instrument. Both instruments used a Cu $K\alpha_{1,2}$ X-ray source. The powder patterns were analyzed using the HighScore Plus and PowderCell for Windows (PCW) software programs.[100,130]

3.2.3 SEM/EDX

The morphologies of the 40 wt% $LaPO_4$-BG samples annealed at 1100 and 700 ^oC as well as the 40 wt% $CePO_4$-BG [Ce(III)] and 40 wt% $CePO_4$-BG [Ce(IV)] samples annealed at 1100 ^oC were studied by SEM and EDX analysis. The samples were mounted in epoxy resin, polished using 1 µm diamond paste, and coated with Cr metal prior to data collection. The composite materials were analyzed using a Hitachi SU3500 variable pressure scanning electron microscope (SEM) equipped with an Oxford Aztec X-Max50 SDD energy dispersive X-Ray (EDX) detector. Both $CePO_4$-BG composite materials were analyzed in variable pressure mode with a pressure of 30 Pa to minimize charging affects, which were present even after being coated with Cr. Backscattered electron images were collected from the polished surfaces using a magnification of 1,000X and an accelerating voltage of 15 kV. EDX maps of P, Si, Na, Ca, and La or Ce were collected from each material to study the distribution of these elements.

3.2.4 X-Ray Absorption Near-Edge Spectroscopy (XANES)

3.2.4.1 La L_1-, Ce L_1-, and Ce L_3-edge XANES

The La L_1-, Ce L_1-, and Ce L_3-edge XANES spectra were collected using the Sector 20 bending magnet (20BM) beamline located at the Advanced Photon Source (APS), Argonne National Laboratory.[101] The La L_1-edge XANES spectra were collected from $LaPO_4$ annealed at 1100 and 700 ^oC as well as from the 40 wt% $LaPO_4$-BG composite materials annealed at 1100, 800, and 700 ^oC. The Ce L_1-edge XANES spectra were collected from: $CePO_4$ [Ce(III)] and $CePO_4$ [Ce(IV)] annealed at 1100 ^oC; the 40 wt% $CePO_4$-BG [Ce(III)] and 40 wt% $CePO_4$-BG [Ce(IV)] composite materials annealed at 1100, 1000, 900, 800, and 700 ^oC; and the 20 wt% $CePO_4$-BG

[Ce(III)] and 20 wt% $CePO_4$-BG [Ce(IV)] composite materials annealed at 1100 and 700 ^oC. Sample preparation and experimental parameters for the collection of the La L_1-, Ce L_1-, and Ce L_3-edge were identical and is explained in Section 2.2.4.1. The spectral resolution of the La and Ce L_1-edge XANES spectra was 0.6 eV at 6266 eV and 0.7 eV at 6549 eV, respectively, while the spectral resolution of the Ce L_3-edge XANES spectra was 0.6 eV at 5723 eV.[101] The La and Ce L_1-edge XANES spectra were calibrated by collecting a Mn K-edge XANES spectrum from Mn metal foil and setting the first derivative of the absorption edge to 6539 eV.[101] The Ce L_3-edge XANES spectra were calibrated by collecting a Cr K-edge XANES spectrum from Cr metal foil and setting the first derivative of the absorption edge to 5989 eV.[101] All XANES spectra were normalized, calibrated, and analyzed using the Athena software program.[103]

The Ce L_1- and Ce L_3-edge XANES spectra were fitted using a linear combination fitting (LCF) method and a combination of Ce standards so as to determine the ratio of Ce oxidation states present in the glass-ceramic composite materials. The energy range of the fit was set to -20 eV to +28 eV relative to the Ce L_1 absorption edge and -20 eV to +18 eV relative to the Ce L_3 absorption edge. This method is able to provide percent compositions of Ce^{3+} and Ce^{4+} present in the composite material.[71] The standards used to fit the Ce L_1- and L_3-edge XANES spectra were $CePO_4$ [Ce(III)] and CeO_2.

3.2.4.2 P $L_{2,3}$- and Si $L_{2,3}$-edge XANES

The P and Si $L_{2,3}$-edge XANES spectra were collected using the Variable Line Spacing-Plane Grating Monochromator (VLS-PGM) beamline located at the Canadian Light Source (CLS).[94] The P $L_{2,3}$- and Si $L_{2,3}$-edge XANES spectra were collected from 40 wt% $LaPO_4$–BG, $CePO_4$–BG [Ce(III)] and $CePO_4$–BG [Ce(IV)] composite materials annealed at 1100, 900, and 700 ^oC. P $L_{2,3}$- and Si $L_{2,3}$-edge XANES spectra were collected from 20 wt% $CePO_4$-BG [Ce(III)] and $CePO_4$–BG [Ce(IV)] composite materials annealed at 1100 and 700 ^oC. P $L_{2,3}$-edge XANES spectra were also collected from the $LaPO_4$, $CePO_4$ [Ce(III)], and $CePO_4$ [Ce(IV)] ceramics while Si $L_{2,3}$-edge XANES spectra were collected from the BG material. Sample preparation and experimental parameters for the collection of the P $L_{2,3}$- and Si $L_{2,3}$-edge is explained in Section 2.2.4.2.

3.3 Results

3.3.1 Formation of $REPO_4$-BG Composite Materials

3.3.1.1 $LaPO_4$-BG

Powder X-Ray diffraction patterns were collected to determine the identity of any crystalline phases within the glass-ceramic composite materials. Figure 3.1 shows XRD patterns from: 20 and 40 wt% $LaPO_4$-BG composite materials annealed at 1100 and 700 ^oC; 40 wt% $LaPO_4$-BG composite materials annealed at 900 and 800 ^oC; and $LaPO_4$ annealed at 1100 and 700 ^oC. The major crystal phase observed in all diffraction patterns shown in Figure 3.1 was $LaPO_4$, which adopts the monazite crystal structure. Quartz (a polymorph of SiO_2) was also observed in the XRD patterns from the 20 and 40 wt% $LaPO_4$-BG composites annealed at 700 ^oC (Figure 3.1). The calculated lattice constants from these materials are presented in Table B-1. There were no observable changes in the $LaPO_4$ lattice constants or intensity ratios of the diffraction peaks belonging to $LaPO_4$ in any of these materials.

Powder XRD patterns from 20 and 40 wt% $LaPO_4$-BG composite materials annealed at 700 ^oC as well as $LaPO_4$ annealed at 700 ^oC were observed to possess broader diffraction peaks than those annealed at higher temperatures (Figure 3.1). Size or strain effects can cause broad peaks in a powder XRD pattern.[131] The size and strain for the 20 and 40 wt% $LaPO_4$-BG composite material annealed at 700 ^oC were calculated independently using the Scherrer equation and the strain equation.[132] It was observed that the size values remained similar (27-37 nm) while the strain values varied greatly and were small (0.33-0.86%) (Table B-2). As such, the broad peaks were determined to be primarily caused by small crystallites being present in the materials annealed at 700 ^oC.

A phase analysis was performed to quantify the relative amounts of the different crystalline phases observed in the XRD patterns from the 20 and 40 wt% $LaPO_4$-BG composite materials annealed at 700 ^oC (Table B-3). The XRD pattern from the 20 wt% $LaPO_4$-BG composite material annealed at 700 ^oC contained 15 wt% quartz and 85 wt% $LaPO_4$. The XRD pattern from the 40 wt% $LaPO_4$-BG composite material annealed at 700 ^oC contained 16 wt% quartz and 84% $LaPO_4$. All other $LaPO_4$-BG composite materials studied by powder XRD were determined to only contain $LaPO_4$.

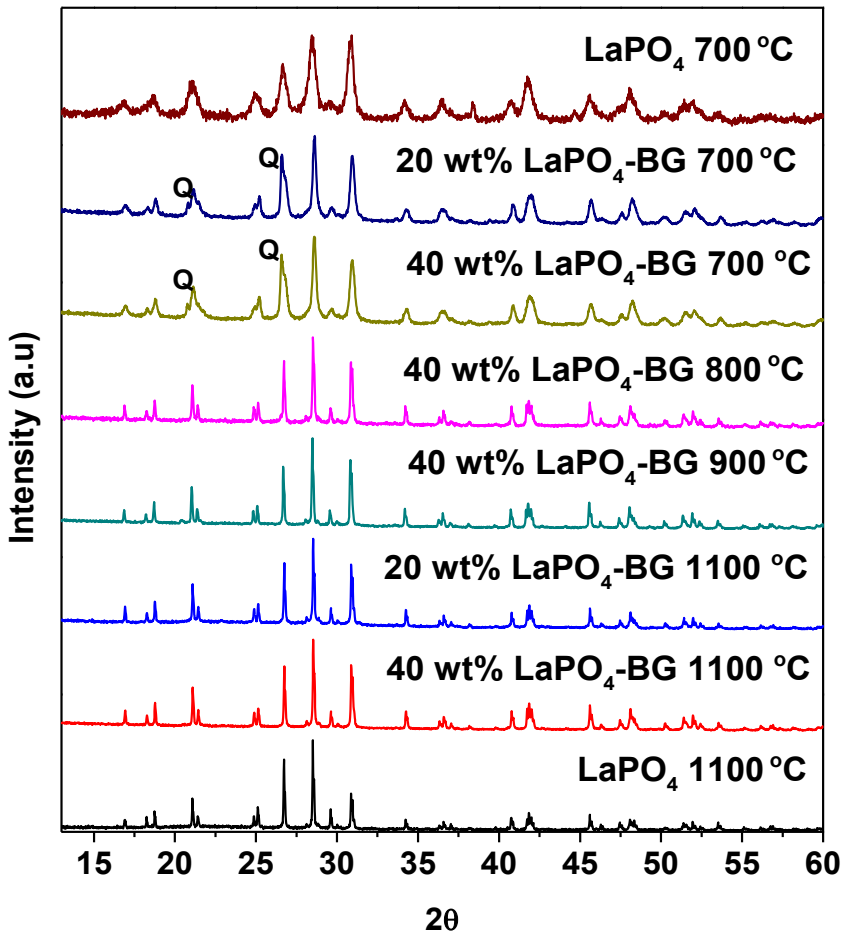

Figure 3.1: XRD patterns from $LaPO_4$, 20 wt% $LaPO_4$-BG annealed at 1100 ^oC and 700 ^oC, 40 wt% $LaPO_4$-BG annealed at 1100, 900, and 700 ^oC. Q = quartz.

3.3.1.2 $CePO_4$-BG [Ce(III)]

Figure 3.2 shows powder XRD patterns from: 20 and 40 wt% $CePO_4$-BG [Ce(III)] composite materials annealed at 1100 and 700 ^oC; 40 wt% $CePO_4$-BG [Ce(III)] composite materials annealed at 1000, 900, and 800 ^oC; and $CePO_4$ [Ce(III)]. $CePO_4$ adopting the monazite crystal structure was the only major crystal phase observed in the diffraction patterns from the 20 and 40 wt% $CePO_4$-BG composite materials annealed at 1100 ^oC (Figure 3.2).[62] $CePO_4$, CeO_2, and crystalline SiO_2 (tridymite, quartz, and cristobalite) was observed in the diffraction patterns (Figure 3.2) from the 40 wt% $CePO_4$-BG [Ce(III)] composite materials annealed at 1000, 900, 800, and 700 ^oC. Crystalline SiO_2 (tridymite, quartz, and cristobalite), CeO_2, and vitusite ($Na_3Ce(PO_4)_2$) formed in the 20 wt% $CePO_4$-BG [Ce(III)] composite material annealed at 700 ^oC; however, no $CePO_4$ was observed in the powder XRD pattern from this material (Figure 3.2). It was observed in the powder XRD patterns from the $CePO_4$-BG [Ce(III)] composite materials that crystalline SiO_2 adopted the tridymite structure when the annealing temperature was high (1000 ^oC) and the quartz structure when the annealing temperature was low (900-700 ^oC) (Figure 3.2). A small amount of cristobalite (another polymorph of SiO_2) was also observed in the powder XRD pattern from the 20 wt% composite material annealed at 700 ^oC (Figure 3.2). This is consistent with previous reports that showed that quartz is the favoured polymorph of SiO_2 at lower temperatures and tridymite is favoured at higher temperatures.[21] Nagelschmidtite ($Ca_{7-x}Na_x(PO_4)_{2+x}(SiO_4)_{2-x}$) was observed as a minor crystal phase in all patterns from the composite materials presented in Figure 3.2. There were no observable changes in the intensity ratios of the diffraction peaks or lattice constants of Ce containing crystal phases (Table B-4).

A phase analysis was performed on the powder XRD patterns presented in Figure 3.2 to obtain relative weight percentages of the crystalline phases (Table B-5). The amount of crystalline SiO_2 was observed to generally increase with decreasing annealing temperature in the $CePO_4$-BG [Ce(III)] composite materials. This follows the known tendency of a glass to crystallize more at lower annealing temperatures due to being below the melting point of the glass.[106] Mole percentages of the crystalline phases (Table B-6) were calculated from the relative weight percentages obtained by the phase analysis. This was done since no apparent changes in the composition of these phases was observed in the powder XRD patterns from these materials. The ratio of crystalline Ce phases (c-Ce%, Table 3.2) was calculated using the mole percentage values from $CePO_4$, CeO_2, and $Na_3Ce(PO_4)_2$ (Table B-6).

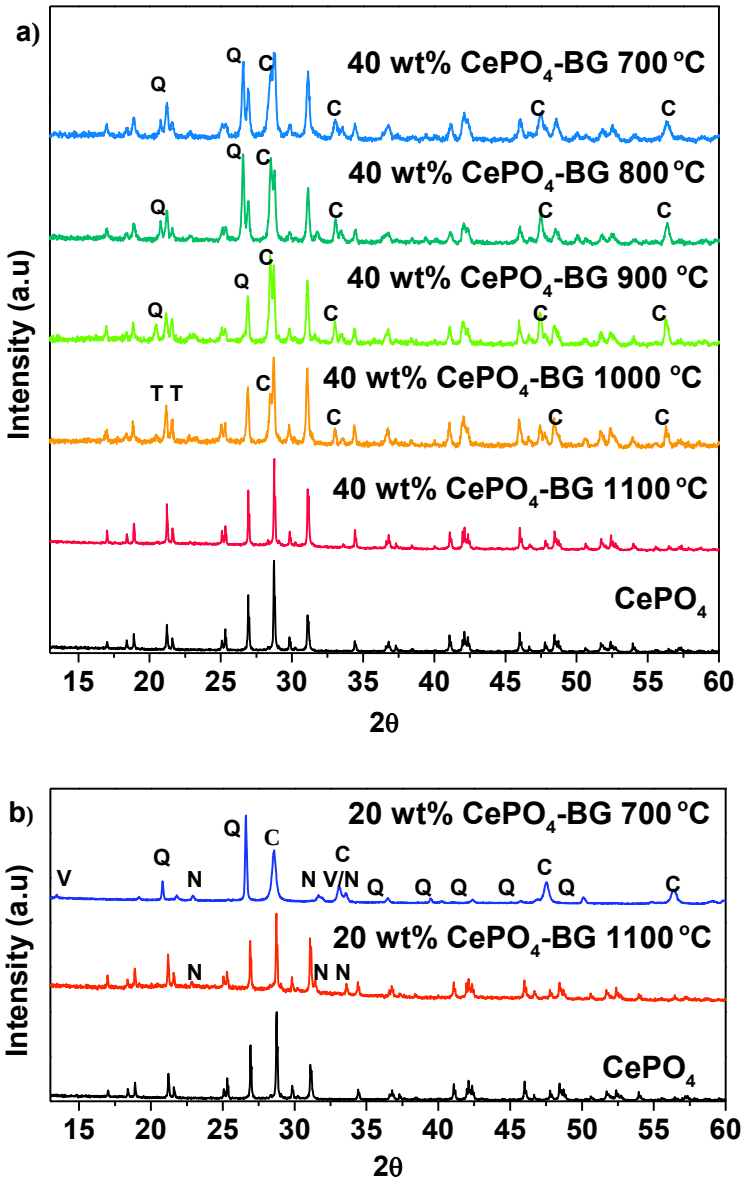

Figure 3.2: a) XRD patterns from $CePO_4$, and 40 wt% $CePO_4$-BG annealed at 1100-700 ºC. b) XRD patterns from $CePO_4$ annealed at 1100 ºC, and 20 wt% $CePO_4$-BG annealed at 700 ºC. All of these materials were made with the Ce^{3+} precursor. C = CeO_2, Q = quartz, V = vitusite, T = tridymite, N = nagelschmidtite.

The relative amount of $CePO_4$ decreased from 100 c-Ce% of the crystalline phase when the annealing temperature was 1100 ^oC to 74 c-Ce% when the annealing temperature was lowered to 900 ^oC. The amount of $CePO_4$ in the 40 wt% $CePO_4$-BG [Ce(III)] composite materials annealed at 700, 800, and 900 ^oC remained similar at 69-74 c-Ce%. In the 20 wt% $CePO_4$-BG [Ce(III)] composite material annealed at 700 ^oC there was 93 c-Ce% CeO_2 and 7 c-Ce% $Na_3Ce(PO_4)_2$. The decrease in the amount of $CePO_4$ and the increase in the amount of CeO_2 as the annealing temperature decreased can be explained by the temperature dependant Ce redox couple ($4Ce^{4+} + 2O^{2-} \rightleftharpoons 4Ce^{3+} + O_2$), which favours Ce^{4+} at lower temperatures.[70,135] CeO_2 would be favoured to form at lower annealing temperatures considering that CeO_2 contains Ce^{4+} while $CePO_4$ contains Ce^{3+}.

3.3.1.3 $CePO_4$-BG [Ce(IV)]

Figure 3.3 shows powder XRD patterns from: 20 and 40 wt% $CePO_4$-BG [Ce(IV)] composite materials annealed at 1100 and 700 ^oC; 40 wt% $CePO_4$-BG [Ce(IV)] composite materials annealed at 1000, 900, and 800 ^oC; and $CePO_4$ [Ce(IV)]. $CePO_4$ adopting the monazite crystal structure was the only major crystalline phase observed in the diffraction patterns from the 20 and 40 wt% $CePO_4$-BG [Ce(IV)] composite materials annealed at 1100 ^oC. $CePO_4$, CeO_2, and crystalline SiO_2 (tridymite; quartz) were observed to form in the 40 wt% $CePO_4$-BG [Ce(IV)] composite materials annealed at 1000 to 800 ^oC. The crystalline phases observed in the 20 wt% composite material by power XRD (Figure 3.3) were vitusite ($Na_3Ce(PO_4)_2$), CeO_2, and crystalline SiO_2 (quartz). The crystalline phases observed in the 40 wt% $CePO_4$-BG [Ce(IV)] composite material were $CePO_4$, vitusite, CeO_2, and quartz (Figure 3.3). Nagelschmidtite ($Ca_{7-x}Na_x(PO_4)_{2+x}(SiO_4)_{2-x}$) was observed as a minor crystal phase in all powder XRD patterns from the $CePO_4$-BG [Ce(IV)] composite materials presented in Figure 3.3. There were no observable changes in the lattice constants of any crystalline phases (Table B-4) and there were no changes in the intensity ratios of the powder XRD peaks.

Table 3.2 shows the ratio of crystalline Ce phases (c-Ce%) calculated using the mole percentages obtained by a phase analysis of the powder XRD patterns (Table B-6). The amount of $CePO_4$ decreased from 100 to 54 c-Ce% while the amount of CeO_2 increased from 0 to 46 c-Ce% in the $CePO_4$-BG [Ce(IV)] composite materials as the annealing temperature was lowered from 1100 to 900 ^oC.

Table 3.2: Ratio of crystalline Ce phases (c-Ce%) in $CePO_4$-BG [Ce(III)] and $CePO_4$-BG [Ce(IV)] composite materials determined by powder XRD.

Composition	Annealing Temperature (°C)	$CePO_4$	CeO_2	$Na_3Ce(PO_4)_2$
40 wt% CePO4-BG [Ce(III)]	1100	100%	0%	0%
20 wt% CePO4-BG [Ce(III)]	1100	100%	0%	0%
40 wt% CePO4-BG [Ce(III)]	1000	86(2)%	14(1)%	0%
40 wt% CePO4-BG [Ce(III)]	900	74(5)%	26(1)%	0%
40 wt% CePO4-BG [Ce(III)]	800	69(1)%	31(1)%	0%
40 wt% CePO4-BG [Ce(III)]	700	73(2)%	27(1)%	0%
20 wt% CePO4-BG [Ce(III)]	700	0%	93(1)%	7(2)%
40 wt% CePO4-BG [Ce(IV)]	1100	100%	0%	0%
20 wt% CePO4-BG [Ce(IV)]	1100	100%	0%	0%
40 wt% CePO4-BG [Ce(IV)]	1000	76(1)%	24(1)%	0%
40 wt% CePO4-BG [Ce(IV)]	900	54(4)%	46(2)%	0%
40 wt% CePO4-BG [Ce(IV)]	800	60(3)%	40(1)%	0%
40 wt% CePO4-BG [Ce(IV)]	700	58(1)%	35(1)%	7(2)%
20 wt% CePO4-BG [Ce(IV)]	700	0%	70(1)%	30(2)%

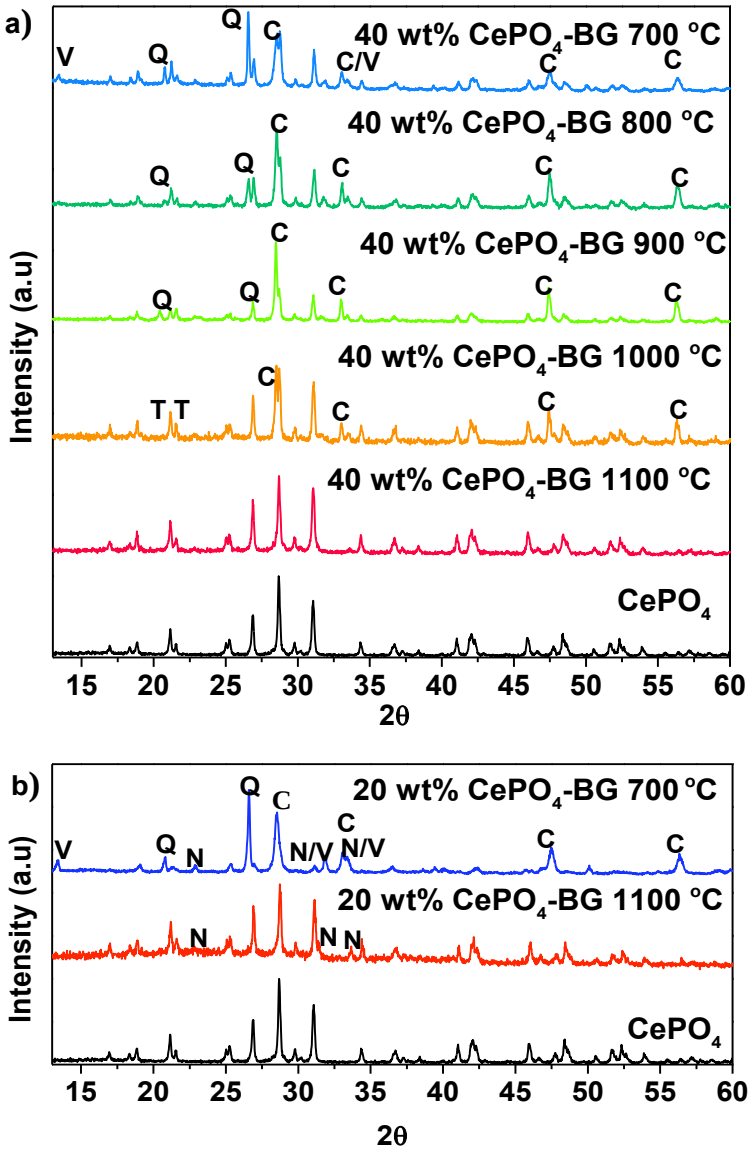

Figure 3.3: a) XRD patterns from $CePO_4$, and 40 wt% $CePO_4$-BG annealed at 1100-700 ºC. b) XRD patterns from $CePO_4$, and 20 wt% $CePO_4$-BG annealed at 1100 and 700 ºC. All of these materials were made with the Ce^{4+} precursor. C = CeO_2, Q = quartz, V = vitusite, T = tridymite, N = nagelschmidtite.

The amount of $CePO_4$, CeO_2, and $Na_3Ce(PO_4)_2$ in the 20 wt% $CePO_4$-BG [Ce(IV)] composite materials annealed at 700 ^oC were 0, 70, and 30 c-Ce%, respectively. This trend suggests that lower annealing temperatures favoured the formation of CeO_2 over $CePO_4$ which has been observed previously.[132] This can once again be explained by the temperature dependant Ce redox couple ($4Ce^{4+} + 2O^{2-} \rightleftharpoons 4Ce^{3+} + O_2$), which favours Ce^{4+} at lower temperatures.[70,133] The relative amount of Ce^{4+} compared to Ce^{3+} is inversely proportional to temperature in the exothermic reduction reaction.[135] CeO_2 would be favoured to form at lower annealing temperatures as CeO_2 contains Ce^{4+} while $CePO_4$ contains Ce^{3+}.

3.3.2 Morphology and Elemental Distribution

3.3.2.1 $LaPO_4$-BG

SEM images and EDX maps of the glass-ceramic composite materials were collected to observe the morphology of the materials and any trends in the elemental distribution that were dependent on the synthesis conditions. Figure 3.4 shows the BSE image collected from the 40 wt% $LaPO_4$-BG composite material annealed at 1100 ^oC. It was observed that the microstructure of the material consists of light grey areas dispersed in a dark matrix. Dark grey areas were also observed in the BSE image (Figure 3.4a). EDX maps of La, P, Si, Na, and Ca are also shown in Figure 3.4. The elemental distribution of La, P, Si, Na, and Ca was able to be observed by comparing the BSE image to the EDX maps (Figure 3.4). The areas on the EDX maps that corresponded to the light grey areas in the BSE image consisted of La and P (Figure 3.4) indicating that these areas were $LaPO_4$ crystallites. The areas on the EDX maps that corresponded to the dark grey areas in the BSE image consisted of Na, Ca, and P (Figure 3.4). The likely identity of this phase is nagelschmidtite ($Ca_{7-x}Na_x(PO_4)_{2+x}(SiO_4)_{2-x}$) and is discussed in Section 3.4.1.1 The areas on the EDX maps that corresponded to the matrix in the BSE image consisted of Si, Na, and Ca (Figure 3.4) which indicates the matrix is borosilicate glass. BSE images and EDX maps were also collected from the 40 wt% $LaPO_4$-BG composite material annealed at 700 ^oC (Figure B-1). No distinct crystallites or domains with high La and P concentrations and a low Si concentration could be observed from this data suggesting the crystallites of $LaPO_4$, which were determined to be present from the powder XRD pattern from this material (Figure 3.1), were too small to be resolved in these images.

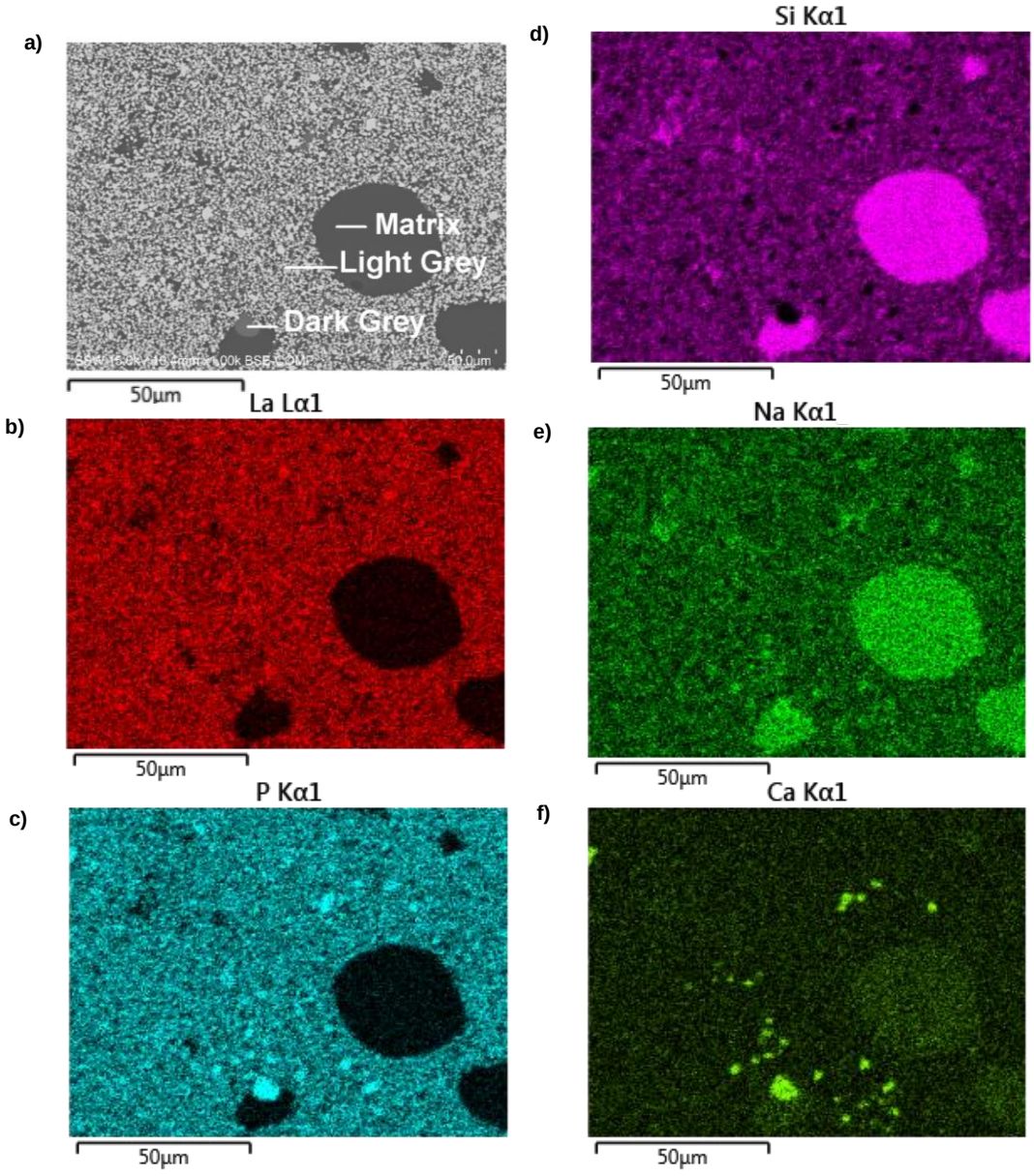

Figure 3.4: a) SEM image of 40 wt% $LaPO_4$-BG composite material annealed at 1100 ^oC, EDX maps of b) La, c) P, d) Si, e) Na, and f) Ca.

3.3.2.2 $CePO_4$-BG [Ce(III)]

Figure 3.5 shows the BSE image collected from the 40 wt% $CePO_4$-BG composite material annealed at 1100 ^oC. Light grey and dark grey areas were observed to be dispersed in a dark matrix in the BSE image. EDX maps of Ce, P, Si, Na, and Ca are shown in Figure B-2. The areas on the EDX maps that corresponded to the light grey areas in the BSE image were determined to contain Ce and P (Figure B-2) which indicates that these areas were $CePO_4$ crystallites. The areas on the EDX maps that corresponded to the dark grey areas in the BSE image consisted of Na, Ca and P (Figure B-2) suggesting these areas are nagelschmidtite ($Ca_{7-x}Na_x(PO_4)_{2+x}(SiO_4)_{2-x}$) crystallites. The areas on the EDX maps that corresponded to the matrix in the BSE image was observed to contain Si, Na, and Ca (Figure B-2). This indicates that the dark matrix is the borosilicate glass.

3.3.2.3 $CePO_4$-BG [Ce(IV)]

The BSE image from the 40 wt% $CePO_4$-BG [Ce(IV)] composite material annealed at 1100 ^oC is shown in Figure 3.5. EDX maps of Ce, P, Si, Na, and Ca are shown in Figure B-3. The BSE image revealed a microstructure that consisted of four areas: light grey areas, dark grey areas, a dark matrix, and bright areas. The areas on the EDX maps that corresponded to the light grey areas in the BSE image were determined to contain Ce and P (Figure B-3) which indicates that these areas were $CePO_4$ crystallites. The areas on the EDX maps that corresponded to the dark grey areas in the BSE image consisted of Na, Ca and P (Figure B-3) indicating that these areas are nagelschmidtite ($Ca_{7-x}Na_x(PO_4)_{2+x}(SiO_4)_{2-x}$) crystallites. The areas on the EDX maps that corresponded to the matrix in the BSE image was observed to contain Si, Na, and Ca (Figure B-3). This indicates that the dark matrix is the borosilicate glass. The areas on the EDX maps that corresponded to the bright areas in the BSE image was observed to only contain Ce. This suggests that CeO_2 crystallites are present in this material.

3.3.3 Local Chemical Environment

XANES spectra were collected from borosilicate glass, $LaPO_4$, $CePO_4$ [Ce(III)], $CePO_4$ [Ce(IV)], and the glass-ceramic composite materials in order to understand the local chemical environment of La, Ce, P, and Si in the composite materials.

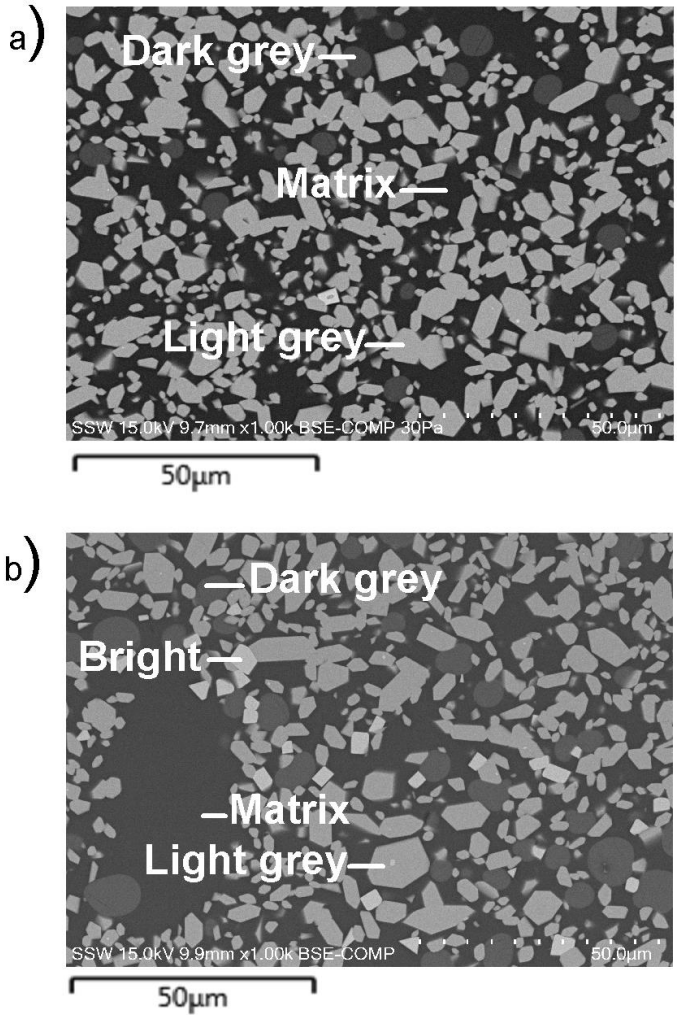

Figure 3.5: SEM images from a) 40 wt% $CePO_4$-BG annealed at 1100 ^oC and synthesized using a Ce^{3+} precursor, and b) 40 wt% $CePO_4$-BG annealed at 1100 ^oC and synthesized using a Ce^{4+} precursor**.**

3.3.3.1 La L_1-edge XANES

The La L_1-edge XANES spectra were collected to observe the local chemical environment of La within the ceramic and glass-ceramic composite materials. The La L_1-edge XANES spectra (Figure 3.6) are comprised of two features. The first is the pre-edge at 6273 eV which is caused by the 2s → 5d quadrupolar transition while the second is the main-edge at 6285 eV which is caused by a 2s → 6p dipolar transition.[109] The La L_1-edge XANES spectrum can be treated as analogous to transition metal K-edge spectra which are used to collect information on the local coordination environment of the metal ion.[91] A less intense main-edge and more intense pre-edge would, generally, indicate a lowering of the coordination number.[109] This is due to greater overlap of the 6p and 5d orbitals leading to the pre-edge transition possessing more dipolar character at lower coordination numbers.[109] In $LaPO_4$, La is 9-coordinate while in borosilicate glass the coordination number of La is lower.[136] As such, if a change in the intensity of the main-edge and pre-edge features was observed in any of the La L_1-edge XANES spectra from the $LaPO_4$-BG composite materials compared to the $LaPO_4$ ceramic then it could be suggested to be caused by La^{3+} ions being present in the glass phase.

Figure 3.6 presents the La L_1-edge XANES spectra from: 40 wt% $LaPO_4$-BG composites annealed at 1100, 800 and 700 ^oC; 20 wt% $LaPO_4$-BG composite annealed at 1100 ^oC; and $LaPO_4$ annealed at 1100 and 700 ^oC. There were no observable changes when the La L_1-edge spectra from the ceramic $LaPO_4$ materials were compared to the La L_1-edge XANES spectra from the $LaPO_4$-BG composite materials. This confirms little to no dissolution of $LaPO_4$ within the glass matrix.

3.3.3.2 Ce L_1-edge XANES

Ce L_1-edge XANES spectra were collected to probe the local chemical environment of Ce. The L_1-edge XANES spectra of rare-earth elements are all similar in terms of line shape and transitions.[91,137] The Ce L_1-edge can be interpreted similarly to the La L_1-edge where information on the coordination number of the rare-earth can potentially be observed.[91] The Ce L_1-edge XANES spectra are also affected by changes in the average oxidation state of Ce.[138] The effect from changes in the oxidation state will dominate the spectra over changes in coordination environment. Such changes are not observed in the La L_1-edge XANES spectra as La^{3+} is the only stable cation.

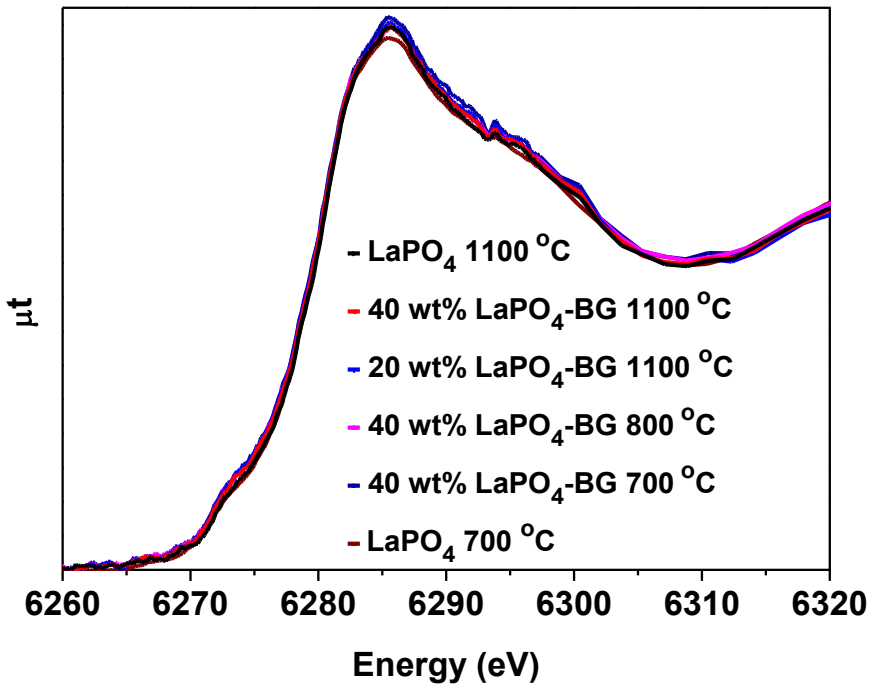

Figure 3.6: La L_1-edge XANES spectra from $LaPO_4$ annealed at 1100 and 700 ºC, 40 wt% $LaPO_4$-BG annealed at 1100, 800 and 700 ºC, 20 wt% $LaPO_4$-BG annealed at 1100 ºC.

A linear combination fitting can be performed to determine the relative amounts of Ce^{3+} and Ce^{4+} present. This is done by using spectra from $CePO_4$ [Ce(III)] (Ce^{3+}) and CeO_2 (Ce^{4+}) as standards due to the experimental spectrum being a convolution of the individual Ce^{3+} and Ce^{4+} spectra. Information of the local chemical environment of Ce was not able to be determined accurately due to changes in the oxidation state also affecting the spectra.

3.3.3.2.1 $CePO_4$-BG [Ce(III)]

Figure 3.7 shows the Ce L_1-edge XANES spectra from: CeO_2; $CePO_4$ [Ce(III)]; 40 wt% $CePO_4$-BG [Ce(III)] composites annealed at 1100, 1000, 900, 800, and 700 ^oC; and 20 wt% $CePO_4$-BG [Ce(III)] composites annealed at 1100 and 700 ^oC. The results from the linear combination fittings of these spectra are shown in Table 3.3 while the fits for each individual spectrum are shown in Figure B-4. There was more Ce^{3+} observed in the spectrum from the 40 wt% $CePO_4$-BG [Ce(III)] material (90%) than the spectrum from the 20 wt% $CePO_4$-BG [Ce(III)] material (84%) when the annealing temperature was 1100 ^oC (Table 3.3). The amount of Ce^{3+} in the spectra from the 40 wt% $CePO_4$-BG [Ce(III)] composite materials decreased from 90% to 77% when the annealing temperature was lowered from 1100 ^oC to 900 ^oC (Table 3.3). The amount of Ce^{3+} in the spectra from the 40 wt% $CePO_4$-BG composite materials remained similar at ~77% when the annealing temperature was 700 to 900 ^oC (Table 3.3). The amount of Ce^{3+} in the spectrum from the 20 wt% $CePO_4$-BG composite material annealed at 700 ^oC (22%) was much lower than in the rest of the materials (Table 3.3). This trend is expected as the Ce redox couple ($4Ce^{4+} + 2O^{2-} \rightleftharpoons 4Ce^{3+} + O_2$) favours Ce^{4+} at lower temperatures.[70,133]

3.3.3.2.2 $CePO_4$-BG [Ce(IV)]

Figure 3.7 shows the Ce L_1-edge XANES spectra from: CeO_2; $CePO_4$ [Ce(IV)]; 40 wt% $CePO_4$-BG [Ce(IV)] composites annealed at 1100, 1000, 900, 800, and 700 ^oC; and 20 wt% $CePO_4$-BG [Ce(IV)] composites annealed at 1100 and 700 ^oC. The tabulated results from the linear combination fittings are presented in Table 3.3 and the individual fits from each spectrum are shown in Figure B-5. The amount of Ce^{3+} in the spectra from the $CePO_4$-BG [Ce(IV)] composite materials annealed at 1100 ^oC decreased from 93% to 81% when the ceramic loading was lowered from 40 to 20 wt% (Table 3.3). The amount of Ce^{3+} in the spectra from the 40 wt% $CePO_4$-BG [Ce(IV)] composite materials decreased from 93% to 66% when the annealing temperature was lowered from 1100 to 700 ^oC (Table 3.3).

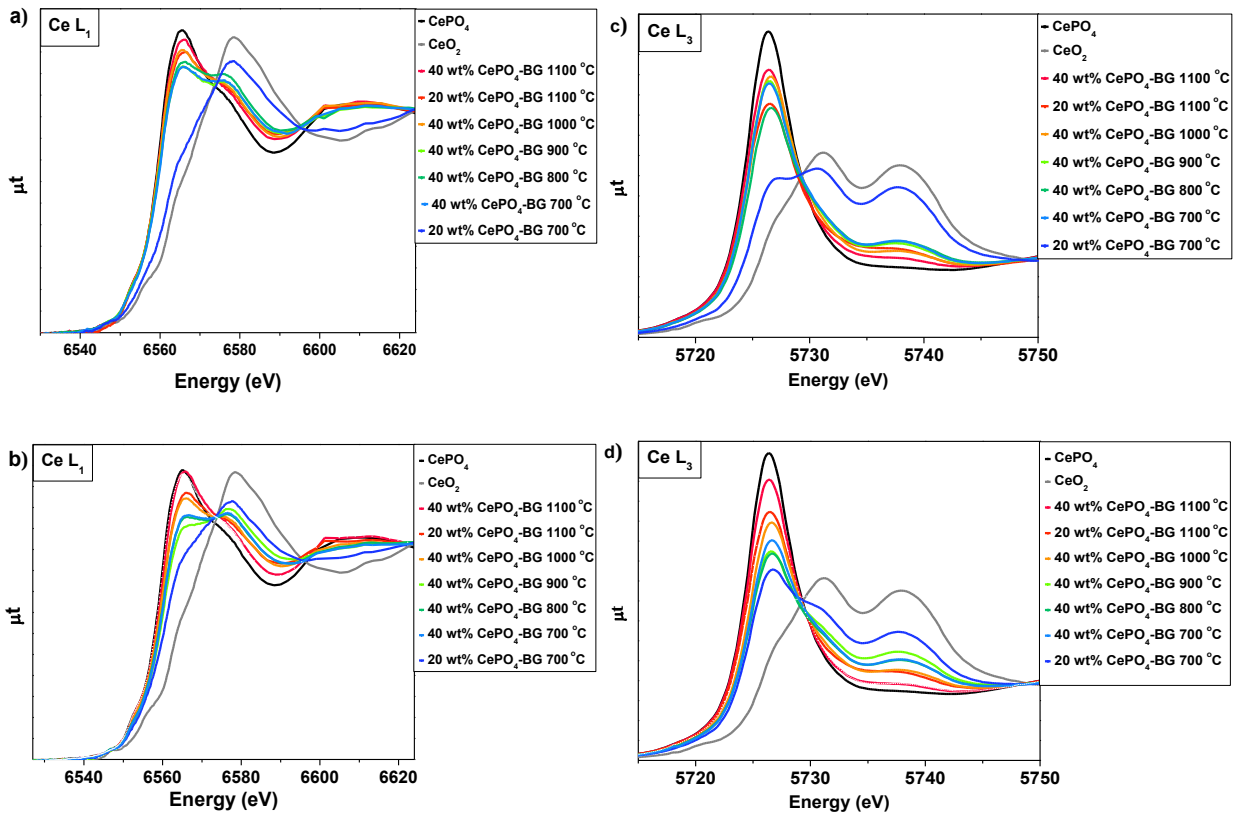

Figure 3.7: a) Ce L_1-edge XANES spectra from $CePO_4$, and 40 wt% $CePO_4$-BG annealed at 1100-700 °C, and $CePO_4$, and 20 wt% $CePO_4$-BG annealed at 1100 and 700 °C. All materials were made with the Ce^{3+} precursor. b) Ce L_1-edge XANES spectra from $CePO_4$, and 40 wt% $CePO_4$-BG annealed at 1100-700 °C, and $CePO_4$, and 20 wt% $CePO_4$-BG annealed at 1100 and 700 °C. c) Ce L_3-edge XANES spectra from $CePO_4$, and 40 wt% $CePO_4$-BG annealed at 1100-700 °C and from 20 wt% $CePO_4$-BG annealed at 1100 and 700 °C. All materials were made with the Ce^{3+} precursor. d) Ce L_3-edge XANES spectra from $CePO_4$ and 40 wt% $CePO_4$-BG annealed at 1100-700 °C and from 20 wt% $CePO_4$-BG annealed at 1100 and 700 °C. All materials in a) and c) were made with the Ce^{3+} precursor. All materials in b) and d) were made with the Ce^{4+} precursor.

Table 3.3: Linear combination fitting results from Ce L_1- and Ce L_3-edge XANES spectra

Composition	Annealing Temperature (°C)	Ce L_1-edge Ce^{3+}	Ce L_1-edge Ce^{4+}	Ce L_3-edge Ce^{3+}	Ce L_3-edge Ce^{4+}
40 wt% CePO4-BG [Ce(III)]	1100	90(3)%	10(3)%	88(3)%	12(3)%
20 wt% CePO4-BG [Ce(III)]	1100	84(3)%	16(3)%	77(5)%	23(5)%
40 wt% CePO4-BG [Ce(III)]	1000	85(3)%	15(3)%	81(1)%	19(1)%
40 wt% CePO4-BG [Ce(III)]	900	77(3)%	23(3)%	77(2)%	23(2)%
40 wt% CePO4-BG [Ce(III)]	800	77(5)%	23(5)%	74(1)%	26(1)%
40 wt% CePO4-BG [Ce(III)]	700	75(2)%	25(2)%	75(2)%	25(2)%
20 wt% CePO4-BG [Ce(III)]	700	22(1)%	78(1)%	24(2)%	76(2)%
40 wt% CePO4-BG [Ce(IV)]	1100	93(3)%	7(3)%	92(2)%	8(2)%
20 wt% CePO4-BG [Ce(IV)]	1100	81(3)%	19(3)%	79(2)%	21(2)%
40 wt% CePO4-BG [Ce(IV)]	1000	78(2)%	22(2)%	73(1)%	27(1)%
40 wt% CePO4-BG [Ce(IV)]	900	59(2)%	41(2)%	58(2)%	42(2)%
40 wt% CePO4-BG [Ce(IV)]	800	67(2)%	33(2)%	61(2)%	39(2)%
40 wt% CePO4-BG [Ce(IV)]	700	66(2)%	34(2)%	64(2)%	36(2)%
20 wt% CePO4-BG [Ce(IV)]	700	41(1)%	59(1)%	44(2)%	56(2)%

3.3.3.3 Ce L_3-edge XANES

Ce L_3-edge XANES spectra were collected to verify the accuracy of the fits obtained in Section 3.3.3.2 because the Ce L_1-edge XANES spectra could be affected by both changes in oxidation state and changes in coordination environment. In addition, any errors in the normalization of Ce L-edge XANES spectra may lead to errors in the fits and data collected at another edge can help verify the results of the fits. The Ce L_3-edge is very sensitive to changes in the oxidation state of Ce and can provide information on the relative amounts of the oxidation states of Ce in a material.[71] This sensitivity is due to the different transitions that can be observed in the Ce L_3-edge XANES spectra.[139] Figure B-6 shows Ce L_3-edge XANES spectra from $CePO_4$ [Ce(III)], a Ce^{3+}-containing material, and CeO_2, a Ce^{4+}-containing material. Only a single transition (feature a_1 in Figure B-6) is observed in the Ce L_3-edge XANES spectrum from Ce^{3+} materials which corresponds to a $2p \rightarrow 5d$ transition.[139] The Ce L_3-edge XANES spectrum from Ce^{4+} materials contains an observable pre-edge feature as well as three main-edge features due to changes in the final state of the Ce^{4+} 4f orbitals ($4f^0$, $4f^1$, and $4f^2$).[71] The pre-edge feature (feature b_1 in Figure B-6) is due to the $2p \rightarrow 4f$ transition.[139] The main-edge features (labelled as b_2 in Figure B-6) are due to $2p \rightarrow 5d$ transitions.[71]

3.3.3.3.1 $CePO_4$-BG [Ce(III)]

Figure 3.7c shows the Ce L_3-edge XANES spectra from: CeO_2; $CePO_4$ [Ce(III)]; 40 wt% $CePO_4$-BG [Ce(III)] composites annealed at 1100, 1000, 900, 800 and 700 ^oC; and 20 wt% $CePO_4$-BG [Ce(III)] composite materials annealed at 1100 and 700 ^oC. The tabulated results from the linear combination fittings are presented in Table 3.3 and the individual fits for each spectrum are shown in Figure B-7. More Ce^{3+} was observed in the spectrum from the 40 wt% $CePO_4$-BG [Ce(III)] material (88%) than the spectrum from the 20 wt% $CePO_4$-BG [Ce(III)] material (77%) when the annealing temperature was 1100 ^oC (Table 3.3). The amount of Ce^{3+} in the spectra from the 40 wt% $CePO_4$-BG [Ce(III)] composite materials decreased from 88% to 77% when the annealing temperature was lowered from 1100 ^oC to 900 ^oC (Table 3.3). The amount of Ce^{3+} in the spectra from the 40 wt% $CePO_4$-BG [Ce(III)] composite materials annealed at temperatures ranging from 900 to 700 ^oC remained similar at 74-77% (Table 3.3). The amount of Ce^{3+} in the 20 wt% $CePO_4$-BG [Ce(III)] composite material annealed at 700 ^oC (24%) was much lower than in the rest of the materials, including the 40 wt% $CePO_4$-BG [Ce(III)] composite materials that were

also annealed at this temperature (Table 3.3). The values derived from fitting the Ce L_3-edge XANES spectra compared favourably to the values derived from fitting the Ce L_1-edge XANES spectra with a maximum difference of 7% being observed.

3.3.3.3.2 $CePO_4$-BG [Ce(IV)]

Figure 3.7d shows the Ce L_3-edge spectra from: $CePO_4$ [Ce(IV)]; CeO_2; 40 wt% $CePO_4$-BG [Ce(IV)] composites annealed at 1100, 1000, 900, 800, and 700 ^oC; and 20 wt% $CePO_4$-BG [Ce(IV)] composite materials annealed at 1100 and 700 ^oC. The tabulated results from the linear combination fittings are presented in Table 3.3 and the individual fits for each spectrum are shown in Figure B-8. The amount of Ce^{3+} in the spectra from the $CePO_4$-BG [Ce(IV)] composite materials annealed at 1100 ^oC decreased from 92% to 79% when the ceramic loading was lowered from 40 to 20 wt% (Table 3.3). The amount of Ce^{3+} in the spectra from the $CePO_4$-BG [Ce(IV)] composite materials decreased from 92% to 58% (Table 3.3) when the annealing temperature was lowered from 1100 to 900 ^oC. The 40 wt% $CePO_4$-BG [Ce(IV)] materials annealed at 900 (58%), 800 (61%) and 700 ^oC (64%) contained similar amounts of Ce^{3+} according to the Ce L_3-edge XANES spectrum from these materials (Table 3.3). The values derived from fitting the Ce L_3-edge XANES spectra compared favourably to the values derived from fitting the Ce L_1-edge XANES spectra with a maximum difference of 6% being observed (Table 3.3).

3.3.3.4 P $L_{2,3}$-edge XANES

P $L_{2,3}$-edge XANES spectra were collected to observe how changes in the composition and annealing temperature affected the local chemical environment of P. The P $L_{2,3}$-edge XANES spectrum is composed of many features due to the high resolution of the spectrum at this low energy (136 eV). These features have been reported to be a result of $2p \rightarrow 3s$ and $2p \rightarrow 3d$ transitions.[58] The 3s and 3d orbitals overlap in energy producing the complicated spectra that are observed.[58] Changes in the conduction states of P caused by distortions in the bond distances and angles in the PO_4 tetrahedra due to changes in the next nearest neighbours can be observed by analysis of P $L_{2,3}$-edge XANES spectra.[58]

3.3.3.4.1 $LaPO_4$-BG

The P $L_{2,3}$-edge XANES spectra for pure $LaPO_4$ annealed at 1100 and 700 ^oC as well as the 40 wt% $LaPO_4$-BG composite materials annealed at 1100, 900 and 700 ^oC are shown in Figure

3.8a. These spectra were all observed to overlap with each other (Figure 3.8) suggesting little to no changes in the local chemical environment of P regardless of annealing temperature or material type (ceramic vs. glass-ceramic composite). These results, in addition to the results from the SEM/EDX analysis, would support the conclusion that P is only located within $LaPO_4$ crystallites in the $LaPO_4$-BG composite materials.

3.3.3.4.2 $CePO_4$-BG [Ce(III)] and $CePO_4$-BG [Ce(IV)]

Figure 3.8b shows the P $L_{2,3}$-edge XANES spectra from: $CePO_4$[Ce(III)] and $CePO_4$ [Ce(IV)], 20 and 40 wt% $CePO_4$-BG [Ce(III)] composites annealed at 1100 ^oC, and 20 and 40 wt% $CePO_4$-BG [Ce(IV)] composites annealed at 1100 ^oC. All spectra were observed to overlap indicating no changes in the local chemical environment of P in these materials. The SEM/EDX analysis of 40 wt% $CePO_4$-BG [Ce(III)] and 40 wt% $CePO_4$-BG [Ce(IV)] suggested some incorporation of Ce and P cations within the glass matrix although no change in local coordination environment of P can be observed based on P $L_{2,3}$-edge XANES spectra from these materials.

Figure 3.8c shows the P $L_{2,3}$-edge XANES spectra collected from the $CePO_4$ [Ce(IV)], 40 wt% $CePO_4$-BG [Ce(III)] and 40 wt% $CePO_4$-BG [Ce(IV)] composite materials annealed at 900 and 700 ^oC. The spectrum from the 40 wt% $CePO_4$-BG [Ce(III)] composite material annealed at 900 and 700 ^oC were observed to possess a more intense peak at ~141.5 eV when compared to the P $L_{2,3}$-edge XANES spectrum from $CePO_4$ [Ce(IV)] (Figure 3.8). This change can suggest more distortion of the PO_4 tetrahedra.[141] The concentration of nagelschmidtite in the 40 wt% $CePO_4$-BG [Ce(IV)] composite materials annealed at 900 and 700 ^oC was not determined to be any higher than what was observed in the 20 wt% $CePO_4$-BG [Ce(III)] composite material annealed at 1100 ^oC which was found to produce a P $L_{2,3}$-edge XANES spectrum that overlapped with a spectrum from $CePO_4$ [Ce(IV)]. Since nagelschmidtite could not be the cause of this change it is likely due to PO_4^{3-} ions incorporated into the glass matrix.

The peak located at 141.5 eV in the P $L_{2,3}$-edge XANES spectra from the 40 wt% $CePO_4$-BG [Ce(IV)] composite materials annealed at 900 and 700 ^oC was more intense than the rest of the spectra (Figure 3.8). These changes can suggest a change in the coordination environment of P.[140] This change is likely to be caused by a change in the coordination environment of P incorporated into the borosilicate glass instead of changes in the coordination environment of P in crystalline phases such as $Na_3Ce(PO_4)_2$.

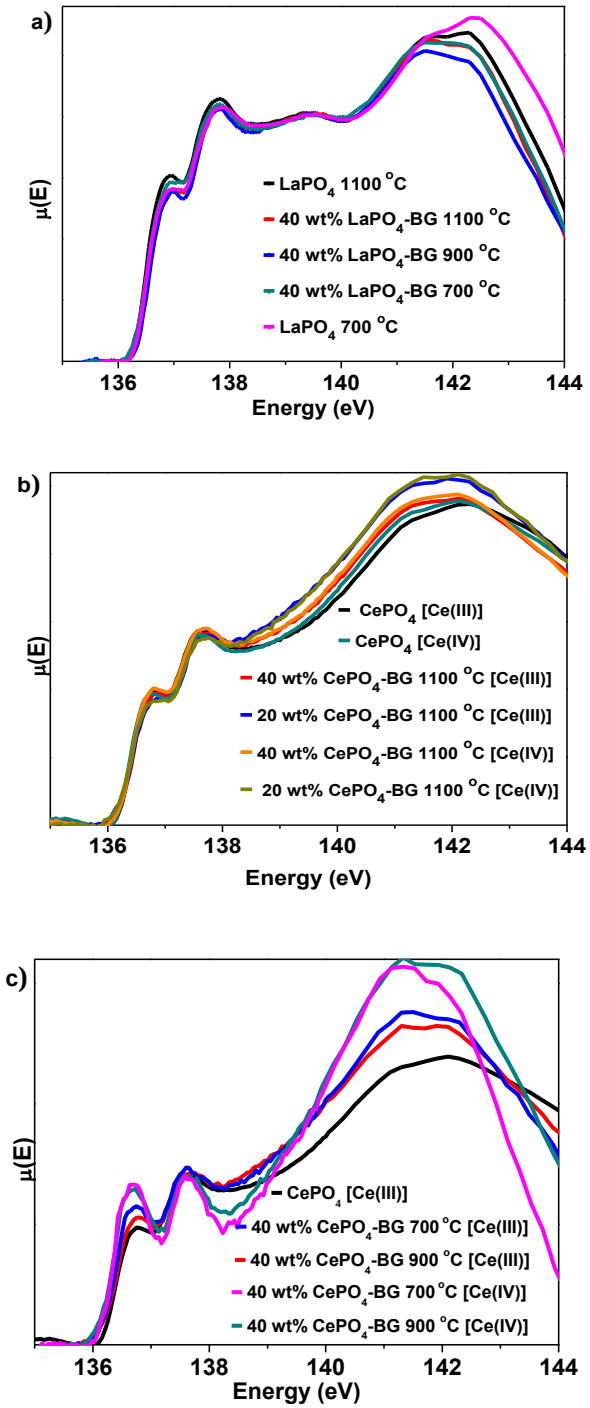

Figure 3.8: a) P $L_{2,3}$-edge XANES spectra from $LaPO_4$ annealed at 1100 and 700 ^oC as well as 40 wt% $LaPO_4$-BG annealed at 1100, 900 and 700 ^oC. b) P $L_{2,3}$-edge XANES spectra from $CePO_4$ annealed at 1100 ^oC as well as 20 and 40 wt% $CePO_4$-BG annealed at 1100 and (c) 40 wt% $CePO_4$-BG composite annealed at 900 and 700 ^oC. These materials were made with a Ce^{3+} or Ce^{4+} precursor.

This is because no new P containing crystalline phases were observed in the powder XRD pattern from the 40 wt% $CePO_4$-BG [Ce(IV)] composite material annealed at 900 ^oC (Figure 3.3) when compared to the powder XRD pattern from the 40 wt% $CePO_4$-BG [Ce(IV)] composite material annealed at 1100 ^oC. Spectra from 20 wt% $CePO_4$-BG [Ce(III)], 40 wt% $CePO_4$-BG [Ce(IV)] and 20 wt% $CePO_4$-BG [Ce(IV)] composite materials annealed at 700 ^oC were also collected; however, these spectra showed no discernable features and could not be interpreted.

3.3.3.5 Si $L_{2,3}$-edge XANES spectra

Si $L_{2,3}$-edge XANES spectra can be used to observe changes in the Si network of the borosilicate glass as a result of differences in synthesis conditions. The Si $L_{2,3}$-edge XANES spectrum consists of two primary features. The lower energy feature is caused by a $2p \rightarrow 3s$ transition while the higher energy feature is caused by a $2p \rightarrow 3d$ transition.[124] The Si $L_{2,3}$-edge XANES spectrum can be used to observe changes in the glass phase of the glass-ceramic composite materials.[2,29] Crystallization of the glass can be observed as a sharpening of the spectra and a shift to higher energy due to more degeneracy in the conduction states that the core electron is promoted.[2] The metal cation can effect the spectra by changing the bond length and covalency of the Si-O bond as a result of the formation of Si-O-M bonds.[2]

3.3.3.5.1 $LaPO_4$-BG

The Si $L_{2,3}$-edge XANES spectra from BG and 40 wt% $LaPO_4$-BG annealed at 1100, 900, and 700 ^oC are presented in Figure 3.9. It can be observed that the spectra from the composite materials overlap with each other and with the spectrum from the borosilicate glass (Figure 3.9). This suggests little interaction between the glass and $LaPO_4$ crystallites in the composite materials. The overlapping Si $L_{2,3}$-edge XANES spectra from 40 wt% $LaPO_4$-BG composite materials annealed at 700, 900, and 1100 ^oC also suggests that the quartz phase that was observed in the XRD pattern from the 40 wt% $LaPO_4$-BG composite material annealed at 700 ^oC (Figure 3.1) did not have a significant effect on the average Si coordination environment.

3.3.3.5.2 $CePO_4$-BG [Ce(III)], $CePO_4$-BG [Ce(IV)]

The spectra collected from $CePO_4$-BG [Ce(III)] and $CePO_4$-BG [Ce(IV)] composite materials contained interference from the Ce $N_{4,5}$-edge.[141]

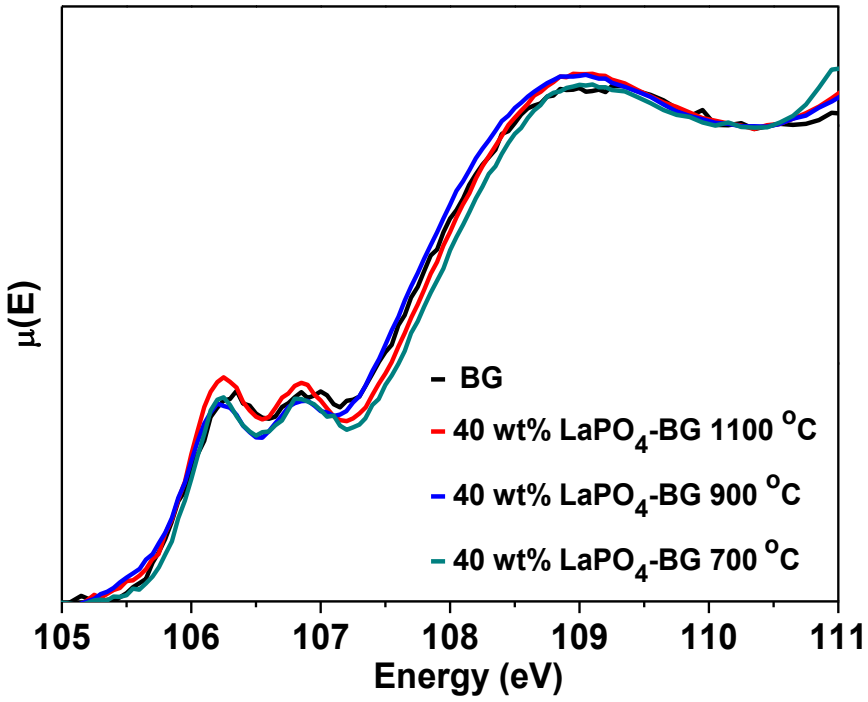

Figure 3.9: Si $L_{2,3}$-edge spectra from borosilicate glass and 40 wt% $LaPO_4$-BG annealed at 1100, 900 and 700 ^oC.

Figure B-9 shows Si $L_{2,3}$-edge spectra from borosilicate glass as well as the 40 wt% $CePO_4$-BG [Ce(III)] composite materials annealed at 1100 and 700 ^oC as examples of this. The Ce $N_{4,5}$-edge edge is composed of a pre-edge region caused by dipole-forbidden transitions below 115 eV and main-edge regions caused by dipole-allowed 4d → 4f transitions.[141] The pre-edge region is composed of many sharp but weak intensity peaks from 102-115 eV.[141] The intensity and sharpness of these peaks are higher for Ce^{3+} than for Ce^{4+}.[141] The Ce $N_{4,5}$-edge features overlap the Si $L_{2,3}$-edge spectrum, which makes normalization and interpretation of the Si $L_{2,3}$-edge XANES spectra from these materials difficult and no conclusions could be reliably drawn.

3.4 Discussion

3.4.1 Crystallization of $REPO_4$-BG Composite Materials

3.4.1.1 $LaPO_4$-BG

$LaPO_4$-BG composite materials were able to be synthesized using the coprecipitation method and annealing temperatures ranging from 1100 to 700 ^oC with limited formation of minor crystalline phases (Figure 3.1). The SEM/EDX analysis showed that the microstructure consisted of $LaPO_4$ crystallites dispersed within a glass matrix (Figure 3.4). Other crystallites were also observed in the SEM image and are likely nagelschmidtite (Figure 3.4). This is because nagelschmidtite was observed to form within $CePO_4$-BG composite materials (Figure 3.5) as well as in $LaPO_4$-BG composite materials synthesized by a one-step ceramic method (Section 2.3.1.1). There was a small amount of nagelschmidtite crystallites observed in the SEM image but no nagelschmidtite peaks were present in the powder XRD pattern from $LaPO_4$-BG composite materials. This shows that this minor crystal phase is present at a concentration that is below the detection limit of powder XRD.

The size of $LaPO_4$ crystallites within the 40 wt% $LaPO_4$-BG composite material annealed at 700 ^oC were found to be smaller than the $LaPO_4$ crystallites that formed within the composite materials annealed at 1100 ^oC (Table B-2). This can be attributed to a combination of factors that affect the glass and ceramic phases. The glass is a liquid at 1100 ^oC, which would aid in the diffusion of La^{3+} and PO_4^{3-} ions.[81,142] However, at 700 ^oC, the annealing temperature is below the melting point of borosilicate glass and so the ions would have less mobility. The crystallinity of monazite-type $LaPO_4$ has been shown to increase as annealing temperature increased from 400-1100 ^oC when $LaPO_4$ was made by the coprecipitation method.[143] This was due to no significant

grain growth taking place up to a temperature of 600 °C.[143] There was minimal effect on the long-range order of $LaPO_4$ (Figure 3.1) or local chemical environment of La (Figure 3.6), P (Figure 3.8) and Si (Figure 3.9) regardless of annealing temperature. Therefore, the annealing temperature used to form the $LaPO_4$-BG composite materials can be used to control the crystallite size without significantly changing the local chemical environment of the ceramic or glass phases.

3.4.1.2 $CePO_4$-BG

$CePO_4$-BG composite materials were able to be successfully synthesized at 1100 °C by a one-step coprecipitation method using either a Ce^{3+} or Ce^{4+} precursor. The long-range order of $CePO_4$ (Figure 3.2 and Figure 3.3) as well as the local chemical environment of P (Figure 3.8) was not affected by ceramic loading or oxidation state of the Ce precursor. Nagelschmidtite and CeO_2 were observed as minor crystal phases in $CePO_4$-BG composite materials annealed at 1100 °C (Figure 3.2 and Figure 3.3). These results show that an annealing temperature of 1100 °C is able to be used to synthesize $CePO_4$-BG composite materials.

CeO_2, crystalline SiO_2 (tridymite, quartz, and cristobalite), and vitusite ($Na_3Ce(PO_4)_2$) formed at annealing temperatures ranging from 1000 to 700 °C (Figures 3 and 4). Formation of CeO_2 was favoured over $CePO_4$ at lower annealing temperatures due to the Ce redox couple which favours Ce^{4+} at lower annealing temperatures.[70,133] More $CePO_4$ and less CeO_2 was observed to be present when the $CePO_4$-BG composite materials were made using a Ce^{3+} precursor compared to when a Ce^{4+} precursor was used (Table 3.2). It has been shown previously that the activation energy for the formation of $CePO_4$ decrease as the amount of Ce^{3+} increases.[135] A maximum amount of Ce^{3+} is present by starting with a Ce^{3+} precursor. This leads to the amount of $CePO_4$ being maximized and the amount of CeO_2 being minimized when a Ce^{3+} precursor is used compared to when a Ce^{4+} precursor is used. Crystalline SiO_2 formed when the annealing temperature was lower than the melting temperature of borosilicate glass (900-1000 °C).[106,142] Vitusite was observed to be present in the 20 wt% $CePO_4$-BG composite materials annealed at 700 °C regardless of if a Ce^{3+} or Ce^{4+} precursor was used (Figures 3.2 and Figure 3.3). Vitusite can form due to an enrichment of Na ions compared to Ce and PO_4 ions as well as the use of lower annealing temperatures.[144] This has been attributed to the similar ionic radii of Na and Ce which allows substitution reactions to take place.[144] The concentration of Na ions compared to Ce and PO_4 ions in $CePO_4$-BG composite materials is higher at lower ceramic loadings and, therefore,

vitusite is favoured to form. Vitusite was also observed to form in the 40 wt% $CePO_4$-BG composite material made using a Ce^{4+} precursor and annealed at 700 ^oC which shows that vitusite can still form at higher ceramic loadings (Figure 3.3). It can be concluded that the most effective way to control the formation of CeO_2, crystalline SiO_2, and vitusite is to increase the annealing temperature since these phases were not observed to form at higher annealing temperatures.

3.4.1.3 Comparison of Crystallization between $LaPO_4$-BG and $CePO_4$-BG Composite Materials

The difference in the observed crystal phases in $LaPO_4$-BG and $CePO_4$-BG composite materials annealed at temperatures ranging from 1000 to 700 ^oC was caused by Ce possessing two stable oxidation states while La only possesses one. Ce^{4+} is favoured over Ce^{3+} at lower annealing temperatures in the $Ce^{3+/4+}$ redox couple and thus crystalline phases containing Ce^{4+} (CeO_2) would be expected to form as the annealing temperature was lowered.[70,133] Crystalline SiO_2 (quartz, tridymite, cristobalite) was observed to form when $CePO_4$-BG composite materials were annealed at 1000 ^oC and when $LaPO_4$-BG composite materials were annealed at 700 ^oC. This difference can be concluded to be caused by the presence of CeO_2. CeO_2 is a known nucleating agent in borosilicate glass and helps to promote crystallization in silicate glass.[145] This is due to crystalline CeO_2 acting as a heterogenous nucleating site for the formation of crystalline SiO_2 and lowering the activation energy for crystallization of the glass network.[145,146] The high temperature at which CeO_2 and crystalline SiO_2 form in $CePO_4$-BG composite materials does not allow $CePO_4$-BG composite materials to be successfully synthesized at low temperatures like the $LaPO_4$-BG composite materials.

Vitusite was not observed to form in $LaPO_4$-BG composite materials even though vitusite can form with La instead of Ce to make $Na_3La(PO_4)_2$ and the Ce-containing version of vitusite was observed to form in $CePO_4$-BG composite materials.[147] The higher chemical stability of $LaPO_4$ over $CePO_4$ at 700 ^oC can be attributed to the distortion of the REO_9 polyhedra.[148] It has been shown previously that the smaller Gd^{3+} ion in $GdPO_4$ had a more distorted REO_9 polyhedra and was less stable than the larger Ce^{3+} ion in $CePO_4$.[148] As La^{3+} is larger than Ce^{3+}, $LaPO_4$ would be expected to be more stable than $CePO_4$ and vitusite would be less likely to form in $LaPO_4$-BG composite materials.

3.4.2 Solubility of $REPO_4$ in Borosilicate Glass

The solubility of Ce ions in the borosilicate glass within the $CePO_4$-BG composite materials can be observed by comparing the results from the powder XRD analysis to the Ce L_1- and L_3-edge XANES analysis. The formal oxidation states of Ce in $CePO_4$, CeO_2, and $Na_3Ce(PO_4)_2$ are Ce^{3+}, Ce^{4+}, and Ce^{3+}, respectively. The presence of $CePO_4$, CeO_2, and $Na_3Ce(PO_4)_2$ can thus be used as indicators for the presence of Ce^{3+} and Ce^{4+} in crystalline phases within $CePO_4$-BG composite materials. The linear combination fittings of Ce L_1- and L_3-edge XANES spectra (Table 3.3) from the $CePO_4$-BG composite materials provide information on the relative amounts of Ce^{3+} and Ce^{4+} present in crystalline as well as amorphous phases within the glass-ceramic composite materials.

No CeO_2 was observed in the powder XRD patterns from the 20 and 40 wt% $CePO_4$-BG composite materials annealed at 1100 ^oC indicating there is little to no crystalline phases containing Ce^{4+} (Figure 3.1 and Figure 3.2). However, Ce^{4+} was observed to be present in the Ce L_1- and L_3-edge XANES spectra collected from the 20 and 40 wt% $CePO_4$-BG composite materials annealed at 1100 ^oC (Table 3.3). These results suggest that Ce^{4+} is incorporated in the borosilicate glass when the annealing temperature is 1100 ^oC. Below 1100 ^oC, the Ce^{4+} crystallizes as CeO_2 in $CePO_4$-BG composite materials. No differences between the powder XRD analysis and Ce L_1- and L_3-edge XANES analysis could be reliably observed; however, it is likely that some Ce was incorporated in the glass when lower annealing temperatures were used.

There was a difference in solubility of La ions in the $LaPO_4$-BG composite materials (Section 3.3.3.1) compared to Ce ions in the $CePO_4$-BG composite materials. This can be explained by the difference in field strength of La and Ce ions. Field strength (FS) is used to predict structural roles and properties of cations within a glass and is calculated by dividing the charge of a cation (z) by the square of the cation-oxygen bond length (a) when the cation six coordinate ($FS = z/a^2$).[64,117,118,122] It has been shown that a phosphate glass containing rare-earth oxides avoids crystallization upon cooling of the glass melt more effectively when the field strength of the rare-earth ion is higher.[149] This was suggested to be caused by the smaller rare-earth ions (higher field strength) being able to modify the glass network to satisfy the local coordination requirements of the rare-earth more successfully than the larger rare-earth ions (lower field strength).[149] Ce^{3+} (a = 2.36 Å, FS = 0.54) and Ce^{4+} (a = 2.22 Å, FS = 0.79) are therefore expected to be able to be more

stable in the glass network than the larger La^{3+} (a = 2.38 Å, FS = 0.50) leading to the difference in solubility.[76,118,150] Since the rare-earth ion can be present in the glass phase as well as the ceramic phase it is important to consider the effect of the rare-earth ion on the composite material as a whole.

3.5 Conclusions

$LaPO_4$-BG and $CePO_4$-BG (made using Ce^{3+} and Ce^{4+} precursors) glass-ceramic composite materials were prepared by a one-step coprecipitation method. The crystallization, morphology, elemental distribution, and local chemical environment of ions within these composite materials was investigated by XRD, SEM, EDX, and XANES. It was concluded through the application of these techniques that it was possible to form $LaPO_4$-BG composite materials at temperatures as low as 700 ^oC and $CePO_4$-BG composite materials at 1100 ^oC with $REPO_4$ as the only RE-containing crystal phase. The difference in the lower limit of annealing temperatures between $LaPO_4$-BG and $CePO_4$-BG was concluded to be caused by the formation of CeO_2. It was also observed that the formation of CeO_2 can increase the temperature at which point crystalline SiO_2 forms in the $CePO_4$-BG composite materials. $CePO_4$ was found to be favoured over CeO_2 or vitusite ($Na_3Ce(PO_4)_2$) when the ceramic loading and/or annealing temperature was higher as well as when starting with a Ce^{3+} precursor. This study has shown that the choice of rare-earth when synthesizing $REPO_4$-BG composite materials can determine the optimal annealing temperature which will be useful for nuclear waste sequestration applications.

Chapter 4 Discussion, Conclusions, and Future Work

4.1 Discussion and Conclusions

Two variations of a one-step method for the synthesis of glass-ceramic composites were developed in this thesis. These synthesis methods were chosen to account for dry and wet synthesis techniques that can both be applicable to nuclear waste sequestration depending on the physical state of the high-level nuclear waste.[151] These synthesis methods provides an alternative way to produce glass-ceramic composite materials that may be more appropriate than methods previously established for certain applications, such as nuclear waste sequestration.

$REPO_4$-BG composite materials containing either $LaPO_4$ or YPO_4 crystallites were synthesized by a one- or two-step ceramic method and discussed in Chapter 2. It was observed by powder XRD that the major crystalline phase in each material was $REPO_4$ (monazite or xenotime). The morphology of $LaPO_4$-BG and YPO_4-BG composite materials synthesized by the one- or two-step ceramic method consisted of $REPO_4$ crystallites dispersed in a glass matrix. The size and shape of the crystallites were observed to change depending on whether the glass-ceramic composite material was made in one step or two steps. This was due to the crystallites forming within the glass phase in the one-step ceramic method while being mechanically ground and mixed to form the composite material in the two-step ceramic method. La L_1-, Y K-, and P $L_{2,3}$-edge XANES spectra revealed that the one-step ceramic method was able to produce composite materials that were chemically similar to the composite materials made by the two-step ceramic method for both $LaPO_4$-BG and YPO_4-BG composite materials. There was a difference in the line shape observed in the Si $L_{2,3}$-edge XANES spectra between $REPO_4$-BG composite materials synthesized by the one-step ceramic method and the composite materials synthesized by the two-step ceramic method. The change in the Si $L_{2,3}$-edge XANES spectra suggested a change in the ordering of the glass. An observed difference in solubility of La cations in $LaPO_4$-BG composite materials and Y cations in YPO_4-BG composite materials was attributed to the differences in the field strength and structural roles of the rare-earth ions. The annealing temperature for $LaPO_4$-BG composite materials synthesized by the one-step ceramic method was found to be able to go as low as 1000 ^oC without partial crystallization of the glass affecting the average coordination

environment of Si. The annealing time for the one-step ceramic method was able to be as low as 1 day.

It was demonstrated in Chapter 3 that $LaPO_4$-BG and $CePO_4$-BG composite materials could be synthesized by a one-step coprecipitation method. All composite materials could be synthesized using an annealing temperature of 1100 ^oC. $LaPO_4$ or $CePO_4$ was the only major crystal phase at 1100 ^oC. The morphology of the composite materials annealed at 1100 ^oC consisted of ceramic crystallites dispersed within a glass matrix. The local chemical environment of La and P in 20 and 40 wt% $LaPO_4$-BG composite materials were observed to be the same as La and P in $LaPO_4$. The local chemical environment of P in 20 and 40 wt% $CePO_4$-BG composite materials was observed to be similar to the local chemical environment of P in $CePO_4$ at 1100 ^oC. There was some Ce^{4+} (~10%) in the 40 wt% $CePO_4$-BG composite materials annealed at 1100 ^oC that was incorporated into the borosilicate glass within the $CePO_4$-BG composite materials. An observed difference in solubility of La^{3+} in $LaPO_4$-BG and $Ce^{3+/4+}$ in $CePO_4$-BG composite materials was attributed to the differences in field strength between the rare-earth ions.

$LaPO_4$-BG composite materials were able to form with only $LaPO_4$ as the major crystalline phase and crystalline SiO_2 (quartz) as a minor crystalline phase at an annealing temperature as low as 700 ^oC. $LaPO_4$ crystallites were determined by powder XRD analysis to be on the nm scale when the annealing temperature was 700 ^oC. The local chemical environment of La and P was found to not change depending on the annealing temperature. $CePO_4$, CeO_2, crystalline SiO_2 (quartz, tridymite, cristobalite), and vitusite were all observed to form in $CePO_4$-BG composite materials annealed at lower annealing temperatures (down to 700 ^oC). More CeO_2 and Ce^{4+} was present as the annealing temperature was lowered which was attributed to Ce^{4+} being favoured at lower annealing temperatures. The maximum amount of $CePO_4$ was found to form when the annealing temperature was high as well as using a Ce^{3+} precursor.

4.2 Comparison and Discussion of the One-Step Ceramic Method and the One-Step Coprecipitation Method

$LaPO_4$-BG composite materials synthesized by the one-step ceramic method presented in Chapter 2 of this thesis were compared to $LaPO_4$-BG composite materials synthesized by the one-step coprecipitation method presented in Chapter 3 of this thesis. This was done in order to compare the effect of wet and dry synthesis methods.

4.2.1 Effect of synthesis method on $LaPO_4$ Crystallites within $LaPO_4$-BG Composite Materials

Few differences were observed in the local chemical environment and long-range order of the target $LaPO_4$ crystal phase when comparing the 20 and 40 wt% $LaPO_4$-BG composite materials that were made by the coprecipitation and ceramic methods using annealing temperatures ranging from 1100 to 800 ^oC. There was no observable difference in peak intensity ratios or peak positions when the powder XRD patterns from the $LaPO_4$-BG composite materials made by the one-step ceramic and coprecipitation methods when compared. The La L_1-edge and P $L_{2,3}$-edge XANES spectra from 20 and 40 wt% $LaPO_4$-BG composite materials made by the one-step ceramic and coprecipitation methods and annealed at 1100 ^oC as well as 900/800 ^oC were observed to possess similar edge energies and line shapes to each other. These results suggest that the long-range order of $LaPO_4$ as well as the local chemical environment of La and P is not dependant on the synthesis method.

The $LaPO_4$ crystallites were observed to be much smaller in the 40 wt% $LaPO_4$-BG composite material made by the coprecipitation method and annealed at 1100 ^oC when compared to the 40 wt% $LaPO_4$-BG composite material made by the ceramic method and annealed at 1100 ^oC. This result is likely linked to the more intimately mixed precursors the coprecipitation-based method allows for.[78] In another study where glass-ceramic composites consisting of magnetite (Fe_3O_4) crystallites in a silicate glass matrix were synthesized the ceramic method also produced larger crystallites than the coprecipitation method.[152] This was attributed to the lower homogeneity and reactivity of the mixed precursor powder prepared by the ceramic method.[152]

The coprecipitation method can use a lower annealing temperature (700 ^oC) when compared to the ceramic method which can allow for smaller crystallites to form. The ceramic method is not able to use this low annealing temperature because of partial crystallization of the glass at 1000-900 ^oC and is discussed more in Section 4.2.2. The smaller crystallites that are formed at 700 ^oC can be beneficial to a glass-ceramic waste form.[46] This is because any changes in crystalline volume as a result of radioactive decay would have smaller effects on the overall waste form.[46] It has been observed in zirconolite glass-ceramics that increasing the Pu loading in the material increased the average size of the zirconolite crystallites.[73] The possibility to lower the

annealing temperature to control for these types of changes in crystallite size can be beneficial if a specific range of crystallite sizes are targeted.

4.2.2 Effect of synthesis method on borosilicate glass

There was far less crystallization of the glass in the composites made by the coprecipitation method at low annealing temperatures (< 1100 ^{o}C). This difference is likely caused by the near atomic level mixing that the coprecipitation method allows.[78] The origin of the formation of crystalline SiO_2 has been investigated previously and was concluded to be initiated by the migration of other cations present such as B, Na, and Ca to produce a Si-rich environment in the glass that is required for crystalline SiO_2 to form.[20] This is because the rate-determining step in the formation of crystalline SiO_2 was found to be the diffusion of the alkali ions away from the Si-rich area.[153] The more intimately mixed precursors present in the coprecipitation method would therefore help to inhibit the partial crystallization of the glass.

There was a slight difference in the edge energy of Si $L_{2,3}$-edge XANES spectra from composite materials made by the coprecipitation method (105.8 eV) and ceramic method (106.1 eV). These results suggest a minor change in the local chemical environment of Si due to the synthesis methods. The edge energy and line shape of the Si $L_{2,3}$-edge XANES spectra from borosilicate glass was more similar to the composite materials made by the coprecipitation method than the ceramic method. This also suggests that the glass matrix in $LaPO_4$-BG composites made by the coprecipitation method is affected by the presence of ceramic crystallites to a lesser extent than the glass in $LaPO_4$-BG composites made by the ceramic method.

4.2.3 Conclusion on the Effect of Synthesis Method on the Formation of $REPO_4$-BG Composite Materials

The results of the comparison presented in Section 4.2 of this thesis suggest that the coprecipitation method is better suited to be used for nuclear waste sequestration. This is supported by the smaller crystallite sizes and lower processing temperatures as a result of using the coprecipitation method.[18,46,80] However, evaluation of additional aspects relevant to the production of nuclear waste forms should be performed in order to support this conclusion. For example, the energy savings that are possible from using a lower annealing temperature in the coprecipitation method may be offset by the more expensive precursors such as tetraethyl orthosilicate over SiO_2.[18]

Also, the benefits of the coprecipitation method might not outweigh the environmental risks of turning the high-level waste into a liquid state if the high-level waste was originally in the solid state.[152] Finally, higher annealing temperatures were required in order to maximize the amount of $CePO_4$ present in $CePO_4$-BG composite materials. This shows that even though the coprecipitation method allowed lower annealing temperatures to be used, those temperatures may not produce the most desirable composition available for a nuclear waste form. This is because ceramic phases such as CeO_2 may form which can have lower chemical stability than the target ceramic phase $CePO_4$. The results and conclusions reported in this thesis provides information that is necessary in order to make an informed decision on the production of glass-ceramic composite nuclear waste forms.

4.3 Significance of Results

The results of this thesis are promising for the use of glass-ceramic composites in nuclear waste sequestration. The one-step ceramic method has proven to be a promising replacement for the two-step ceramic method as few differences were observed in the composite materials made by the ceramic method. The results demonstrate that a glass-ceramic composite waste form can be made as simply as a glass waste form with no extra processing steps.[51] These results also suggest that the high-level nuclear waste does not need to be handled multiple times or for as long of a time to produce a glass-ceramic composite material while still yielding a homogenous distribution of crystallites in a glass matrix.

The results from Chapter 3 demonstrate that a one-step coprecipitation method can be used for the synthesis of $REPO_4$-BG composite materials. The procedure used for this synthesis method is comparable to the AVH process developed in France (described in Section 1.1) which is currently being used to produce borosilicate glass waste forms from reprocessed high-level waste.[1] Both the AVH process and the one-step coprecipitation method dissolves the precursors in a suitable solvent followed by a heat treatment at 500 ^{o}C to obtain the precursor powder.[1] The powder is then annealed at high temperatures to obtain the waste form.[1] This validates the potential applicability of this synthesis method to industry.

Some conclusions on the sequestration of Pu can also be drawn based on Chapter 3. Plutonium is added to a nuclear waste form as PuO_2 which is tetravalent.[135] By comparison with the Pu surrogate Ce, it was found that the Ce^{3+} precursor is preferable over the Ce^{4+} precursor to

form $REPO_4$-BG composite materials. However, the differences in the final composite material caused by the oxidation state of the Ce precursor is minimized at high annealing temperatures (1100 ^oC). If Pu was used instead of Ce differences would be expected. One difference is that $PuPO_4$ decomposes into PuO_2 and P_4O_{10} above 1100 ^oC.[154] The decomposition temperature can be raised by incorporating Pu into a solid solution such as $La_{1-x}Pu_xPO_4$ ($x < 0.15$).[156] Another difference would be the temperature dependence of the Pu redox couple with O relative to the Ce redox couple with O. Over 90% of the Pu was observed to be Pu^{4+} in a borosilicate glass sample annealed at 1200 ^oC.[69] This was in stark contrast to the amount of Ce^{4+} which was observed to decrease from 46.2 to 21.9% when the annealing temperature was increased from 1100 to 1400 ^oC.[69]

The aim to further decrease the annealing temperature using a coprecipitation method was realized in $LaPO_4$-BG composite materials and can potentially have significant implications for the fabrication of nuclear waste forms. By lowering the annealing temperature there can be fewer volatile species present during the synthesis of the waste form.[155] In addition, lowering the annealing temperature can reduce the energy required to form these materials the energy required to reach high annealing temperatures.[18,80]

4.4 Future Work

4.4.1 Follow-Up Studies

There are aspects concerning the one-step ceramic and coprecipitation methods developed in Chapter 2 and Chapter 3 that can be further studied. Changes in the glass ordering was concluded to be present by observing the Si $L_{2,3}$-edge XANES spectra from $LaPO_4$-BG and YPO_4-BG composite materials made by the one- and two-step ceramic methods. The change in the glass ordering could be further explored using solid state NMR to obtain more information. [66] The results from that study can be compared to what was found in this thesis. Another aspect that can be further studied is that the composite materials made by the one-step method consistently contained more air bubbles than the composite materials made by the two-step method. Bubbles can be detrimental to the long-term stability of a waste form by providing a surface for uncontrolled crystallization of the glass which can produce internal stress and cracking in the waste form so this needs to be addressed.[9]

4.4.2 Future Research Directions

Changes in the synthetic method can change the chemistry of the material as was observed in Chapter 2 and Chapter 3. This can lead to changes in the properties of the materials. There are many properties that need to be studied before the one-step synthesis method can be implemented to sequester high-level waste. It is imperative that nuclear waste forms are resistant to both radiation damage and leaching by water since the waste form needs to withstand the radioactive decay of the high-level waste and retain the radioisotopes in the event of contact with ground water.[7,14,28,48,67,74,112] The effect of the one-step synthesis method on these properties should therefore be studied.

Radiation resistance can be simulated and studied using ion implantation. Ions such as 2 MeV Au ions or 90 MeV Xe ions can be used to simulate radiation damage.[46] The higher energy ions have a larger penetration depth which can be useful in probing a heterogenous material such as glass-ceramic composites although the lower energy ions have a more comparable energy to what is expected during radioactive decay.[46] Radiation resistance has been shown to be improved in nanomaterials.[14] This can potentially be utilized by synthesizing $REPO_4$-BG composite materials by the one-step coprecipitation method at low temperatures since that has shown to form crystallites on the nm scale in $LaPO_4$-BG composite materials. This study can be expanded upon by observing any differences in radiation resistance in monazite-type and xenotime-type $REPO_4$ crystallites. Characterization techniques such as XRD and glancing angle XANES can be used to characterize the effect of ion implantation on the long-range order and local chemical environment of the glass-ceramic composite materials.[14,28,112] SEM can be used to observe any changes in the morphology.[28] Differential scanning calorimetry can be used to characterize the thermal stability (defined as the crystallization temperature – the glass transition temperature) of the glass-ceramic composite material.[18] Thermal stability of a glass is the resistance of the glass to crystallization when heated.[18] This is an important measurement to take when studying the radiation resistance of glass-ceramic materials as radioactive decay produces heat which may cause unwanted crystallization of the glass if the thermal stability is too low.[14,18]

Leaching experiments can be performed to study the chemical durability of $REPO_4$-BG composite materials made by one-step methods. The leaching experiments are performed according to standardized methods and use either static conditions where the leachant solution is

not replaced during the experiment whereas in dynamic conditions the leachant solution is replaced periodically.[48] The leaching behaviour of $REPO_4$-BG composite materials made by one-step methods can be characterized by determining the concentration of different ions in the leachant solution by ICP-MS.[48] Once again powder XRD and XANES can be used to determine the affect of leaching on the long-range and local order of the glass-ceramic composite materials. SEM can be used to observe any changes in the morphology.

Further studies on the one-step synthesis method can focus on showing the capabilities of this synthetic method by building upon previous results to work towards more complex and realistic synthesis conditions for synthesizing glass-ceramic composite nuclear waste-forms. A preliminary step could include targeting a solid solution crystalline phase such as $La_{1-x}Gd_xPO_4$. This would test whether $LaPO_4$ and $GdPO_4$ forms or $La_{1-x}Gd_xPO_4$ forms. Building up the complexity of the glass phase is just as important as the ceramic phase. This research can investigate the commonly used oxides in nuclear glass compositions such as Al_2O_3, ZnO, and ZrO_2.[1] Al_2O_3, ZnO, and ZrO_2 are added to decrease the tendency of the glass to crystallize and improve leaching resistance.[1] A final step to this line of research would be to add high-level nuclear waste in the production of $REPO_4$-BG composite materials.

All the potential work described above deals with synthesizing $REPO_4$-BG composite materials for the application of nuclear waste sequestration; however, the potential for the one-step synthesis method goes beyond that one composition and application. For example, in Chapter 3, $LaPO_4$-BG composite materials were observed to be able to be produced with crystallites on the nm scale by lowering the annealing temperature to 700 ^oC. This could potentially be exploited for the synthesis of transparent luminescent materials where nanometer sized crystallites are required.[156] A study to determine maximum ceramic loading before loss of transparency using the one-step synthesis method can be performed in order to maximize the optical properties of the glass-ceramic composite. This can then be compared to glass-ceramic composite materials synthesized by other methods. The one-step method can also be potentially used to synthesize glass-ceramic composite materials with a wide variety of ceramic and glass phases that can be studied as well.

One-step methods for the synthesis of various rare-earth phosphate-borosilicate glass composites were developed within this thesis. The results of using this synthesis method for the

sequestration of high-level nuclear waste is promising and should continue to be studied to further develop and characterize this synthetic method. Proposed studies have been described as potential ways to study the affect of the one-step method on the stability of the waste form. These studies include testing the radiation stability and leaching resistance of the composite materials. This would gather the data necessary in order to further evaluate the one-step method to produce glass-ceramic composite materials for the application of sequestering high-level nuclear waste.

References

1 D. Caurant, P. Loiseau, O. Majérus, V. Aubin-Chevaldonnet, I. Bardez and A. Quintas, *Glasses, Glass-Ceramics and Ceramics for Immobilization of Highly Radioactive Nuclear Wastes*, Nova Science Publishers, Paris, 2009.

2 E. R. Aluri and A. P. Grosvenor, *RSC Adv.*, 2015, **5**, 80939–80949.

3 S. Bahl, S. Peuget, I. Pidchenko, T. Pruessmann, J. Rothe, K. Dardenne, J. Delrieu, D. Fellhauer, C. Jégou, H. Geckeis and T. Vitova, *Inorg. Chem.*, 2017, **56**, 13982–13990.

4 E, De Sanctis, S. Monti, M. Ripani, *Energy from Nuclear Fission*, Springer, Cham 2016.

5 K. V. Wong and S. Dia, *J. Energy Resour. Technol.*, 2017, **139**, 062001.

6 G. S. Duffó, E. A. Arva, F. M. Schulz and D. R. Vazquez, *MRS Proc.*, 2012, **1475**, imrc11-1475-nw35-o20.

7 R. C. Ewing, W. J. Weber and F. W. Clinard, *Prog. Nucl. Energy*, 1995, **29**, 63–127.

8 R. C. Ewing, W. J. Weber and J. Lian, *J. Appl. Phys.*, 2004, **95**, 5949–5971.

9 I. W. Donald, B. L. Metcalfe and R. N. J. Taylor, *J. MATE RIALS Sci.*, 1997, **32**, 5851–5887.

10 M. V. Ramana, *Energy Policy*, 2013, **61**, 196–206.

11 P. Vishnu Anand, R. Rajeev, P. Velavendan, N. K. Pandey and U. Kamachi Mudali, *Prog. Nucl. Energy*, 2018, **104**, 359–367.

12 S. Mishra, A. K. Soda, M. Sridhar, C. Mallika, N. K. Pandey and U. K. Mudali, *Solvent Extr. Ion Exch.*, 2018, **36**, 54–65.

13 W. E. Lee, M. I. Ojovan, M. C. Stennett and N. C. Hyatt, *Adv. Appl. Ceram.*, 2006, **105**, 3–12.

14 M. R. Rafiuddin and A. P. Grosvenor, *J. Alloys Compd.*, 2015, **653**, 279–289.

15 S. Lucas, E. Champion, D. Bregiroux, D. Bernache-Assollant and F. Audubert, *J. Solid State Chem.*, 2004, **177**, 1302–1311.

16 M. Qian, L. Li, H. Li and D. M. Strachan, *J. Non. Cryst. Solids*, 2004, **333**, 1–15.

17 E. D. Zanotto and J. C. Mauro, *J. Non. Cryst. Solids*, 2017, **471**, 490–495.

18 J. E. Shelby, *Introduction to Glass Science and Technology*, The Royal Society of Chemistry, Cambridge, 2005.

19 R. K. Chinnam, A. R. Boccaccini, E. Bernardo and H. Epstein, *Int. J. Appl. Ceram. Technol.*, 2015, **12**, E19–E27.

20 T. K. Gupta and J. H. Jean, *J. Mater. Res.*, 1994, **9**, 999–1005.

21 M. Dapiaggi, L. Pagliari, A. Pavese, L. Sciascia, M. Merli and F. Francescon, *J. Eur. Ceram. Soc.*, 2015, **35**, 4547–4555.

22 J. E. McMurray, R. C. Fay and J. Fantini, *Chemistry*, Pearson Prentice Hall, Upper Saddle River, sixth edit., 2012.

23 W. J. Weber, R. C. Ewing, C. R. A. Catlow, T. D. de la Rubia, L. W. Hobbs, C. Kinoshita, H. Matzke, A. T. Motta, M. Nastasi, E. K. H. Salje, E. R. Vance and S. J. Zinkle, *J. Mater. Res.*, 1998, **13**, 1434–1484.

24 R. C. Ewing and W. Lutze, *Ceram. Int.*, 1991, **17**, 287–293.

25 A. Bohre, K. Avasthi and V. I. Pet'kov, *J. Ind. Eng. Chem.*, 2017, **50**, 1–14.

26 J. Amoroso, J. C. Marra, M. Tang, Y. Lin, F. Chen, D. Su and K. S. Brinkman, *J. Nucl. Mater.*, 2014, **454**, 12–21.

27 A. K. De, B. Luckscheiter, W. Lutze, G. Malow and E. Schiewer, *Am. Ceram. Soc. Bull.*, 1976, **55**, 500–503.

28 E. Paknahad and A. P. Grosvenor, *Solid State Sci.*, 2017, **74**, 109–117.

29 E. Paknahad and A. P. Grosvenor, *Can. J. Chem.*, 2017, **95**, 1110–1121.

30 A. A. Ahmed, A. A. Ali and A. El-Fiqi, *J. Mater. Res. Technol.*, 2019, **8**, 1003–1013.

31 Y. Hu and X. Miao, *Ceram. Int.*, 2004, **30**, 1787–1791.

32 Y. Deng, Q. Liao, F. Wang and H. Zhu, *J. Nucl. Mater.*, 2018, **499**, 410–418.

33 S. D. Stookey, *Ind. Eng. Chem.*, 1959, **51**, 805–808.

34 E. D. Zanotto, *Am. Ceram. Soc. Bull.*, 2010, **89**, 19–27.

35 E. Paknahad, University of Saskatchewan, 2017.

36 P. W. McMillan, *J. Non. Cryst. Solids*, 1982, **52**, 67–76.

37 V. M. Fokin, E. D. Zanotto, N. S. Yuritsyn and J. W. P. Schmelzer, *J. Non. Cryst. Solids*, 2006, **352**, 2681–2714.

38 H. Demirkiran, Y. Hu, L. Zuin, N. Appathurai and P. B. Aswath, *Mater. Sci. Eng. C*, 2011, **31**, 134–143.

39 S. Yamaguchi, K. Moriyama, K. Kajihara and K. Kanamura, *J. Mater. Chem. C*, 2015, **3**, 9894–9901.

40 J. Massera, B. Sevrette, L. Petit, J. Koponen, B. Törngren, B. Glorieux, L. Hupa and M. Hupa, *Mater. Chem. Phys.*, 2014, **147**, 1099–1109.

41 J. S. McCloy and A. Goel, *MRS Bull.*, 2017, **42**, 233–238.

42 P. Loiseau, D. Caurant, I. Bardez, O. Majerus, N. Baffier and C. Fillet, in *Mat. Res. Soc. Symp. Proc. Vol.*, 2002, **757**, 116.8.1-116.8.7.

43 E. R. Vance, S. Moricca, B. D. Begg, M. W. A. Stewart, Y. Zhang and M. L. Carter, *Adv. Sci. Technol.*, 2010, **73**, 130–135.

44 E. Maddrell, S. Thornber and N. C. Hyatt, *J. Nucl. Mater.*, 2015, **456**, 461–466.

45 C. W. Kim and B. Gwan Lee, *J. Nucl. Fuel Cycle Waste Technol.*, 2013, **11**, 1–9.

46 N. Chouard, D. Caurant, O. Majérus, J. L. Dussossoy, P. Loiseau, C. Grygiel and S. Peuget, *J. Nucl. Mater.*, 2019, **516**, 11–29.

47 R. U. Farooqi and P. Hrma, *J. Nucl. Mater.*, 2017, **487**, 210–219.

48 M. R. Rafiuddin and A. P. Grosvenor, *J. Nucl. Mater.*, 2018, **509**, 631–643.

49 S. V. Stefanovsky, O. I. Stefanovsky and I. L. Prusakov, *MRS Adv.*, 2018, **3**, 1073–1083.

50 R. Asuvathraman, K. Joseph, R. Raja Madhavan, R. Sudha, R. Krishna Prabhu and K. V.

Govindan Kutty, *J. Eur. Ceram. Soc.*, 2015, **35**, 4233–4239.

51 F. Wang, Q. Liao, K. Chen, S. Pan and M. Lu, *J. Non. Cryst. Solids*, 2015, **409**, 76–82.

52 J. Deubener, M. Allix, M. J. Davis, A. Duran, T. Höche, T. Honma, T. Komatsu, S. Krüger, I. Mitra, R. Müller, S. Nakane, M. J. Pascual, J. W. P. Schmelzer, E. D. Zanotto and S. Zhou, *J. Non. Cryst. Solids*, 2018, **501**, 3–10.

53 V. V Frolkis, V. V Bezrukov and V. G. Shevchuk, *Exp. Gerontol.*, 1975, **10**, 251–271.

54 N. Clavier, R. Podor and N. Dacheux, *J. Eur. Ceram. Soc.*, 2011, **31**, 941–976.

55 R. S. Hay, P. Mogilevsky and E. Boakye, *Acta Mater.*, 2013, **61**, 6933–6947.

56 L. A. Boatner, *Rev. Mineral. Geochemistry*, 2002, **48**, 87–121.

57 A. Hirsch, P. Kegler, I. Alencar, J. Ruiz-Fuertes, A. Shelyug, L. Peters, C. Schreinemachers, A. Neumann, S. Neumeier, H. P. Liermann, A. Navrotsky and G. Roth, *J. Solid State Chem.*, 2017, **245**, 82–88.

58 M. R. Rafiuddin, E. Mueller and A. P. Grosvenor, *J. Phys. Chem. C*, 2014, **118**, 18000–18009.

59 M. R. Rafiuddin and A. P. Grosvenor, *Inorg. Chem.*, 2016, **55**, 9685–9695.

60 P. Crespo, V. Choque, I. Luna, O. Prieto, S. Cabrera, M. Blanco, G. Callejas, *Revista Boliviana de Quimica*, 2000, **17**, 22 – 27.

61 L.A. Boatner, G.W. Beall, D.F. Mullica, W.O. Milligan, *Inorganica Chimica Acta*, 1982, **60**, 39 – 43.

62 Y. Ni, J. M. Hughes and A. N. Mariano, *Am. Mineral.*, 1995, **80**, 21–26.

63 S. V. Stefanovsky, A. A. Shiryaev, J. V. Zubavitchus, A. A. Veligjanin and J. C. Marra, *Glas. Phys. Chem.*, 2009, **35**, 141–148.

64 J. Wu and J. F. Stebbins, *J. Am. Ceram. Soc.*, 2014, **97**, 2794–2801.

65 D. Manara, A. Grandjean and D. R. Neuville, *J. Non. Cryst. Solids*, 2009, **355**, 2528–

2531.

66 M. Edén, *Annu. Rep. Prog. Chem., Sect. C:Phys. Chem.* 2012, **108**, 177–221.

67 E. Nicoleau, F. Angeli, S. Schuller, T. Charpentier, P. Jollivet and M. Moskura, *J. Non. Cryst. Solids*, 2016, **438**, 37–48.

68 C. P. Royall, F. Turci, S. Tatsumi, J. Russo and J. Robinson, *J. Phys: Condens. Mat.*, 2018, **30**, 2-43

69 C. Lopez, . X. Deschanels, C. Den Auwer, J. N. Cachia and S. Peuget, J. M. Bart, *Phys. Scr.*, 2005, **2005**, 342.

70 C. Lopez, X. Deschanels, J. M. Bart, J. M. Boubals, C. Den Auwer and E. Simoni, *J. Nucl. Mater.*, 2003, **312**, 76–80.

71 R. Sifat, J. C. Beam and A. P. Grosvenor, *Inorg. Chem.*, 2019, **58**, 2299–2306.

72 C. Z. Liao, C. Liu, M. Su and K. Shih, *Inorg. Chem.*, 2017, **56**, 9913–9921.

73 Y. Zhang, D. J. Gregg, L. Kong, M. Jovanovich and G. Triani, *J. Nucl. Mater.*, 2017, **490**, 238–241.

74 W. Li, X. Ding, C. Meng, C. Ren, H. Wu and H. Yang, *J. Mater. Sci.*, 2018, **53**, 6366–6377.

75 Y. Huang, H. Zhang, X. Zhou and S. Peng, *J. Nucl. Mater.*, 2017, **485**, 105–112.

76 B. Y. R. D. Shannon, M. H, N. H. Baur, O. H. Gibbs, M. Eu and V. Cu, *Acta Cryst.*, 1976, **A32**, 751–767.

77 J. Yeomans, *Powder Technol.*, 1992, **73**, 192.

78 S. McCaugherty and A. P. Grosvenor, *J. Mater. Chem. C*, 2019, **7**, 177–187.

79 I. Ebinumoliseh and A. P. Grosvenor, *Inorg. Chem.*, 2018, **57**, 14353-14361.

80 L. E. Smart and E. A. Moore, *Solid State Chemistry*, Taylor & Francis Group, Boca Raton , 2005.

81 R. M. German, P. Suri and S. J. Park, *J. Mater. Sci.*, 2009, **44**, 1–39.

82 M. T. Harrison, *Procedia Mater. Sci.*, 2014, **7**, 10–15.

83 O. Peitl and E. D. Zanotto, *Am. Chem. Soc. Bull.*, 2019, **98**, 30–33.

84 I. Morad, X. Liu and J. Qiu, *J. Am. Ceram. Soc.*, 2019, **102,** 5843-5852.

85 J. S. McCloy, J. Marcial, D. Patil, M. Saleh, M. Ahmadzadeh, H. Chen, J. V. Crum, B. J. Riley, H. Kamat, A. Bréhault, A. Goel, K. E. Barnsley, J. V. Hanna, P. Rajbhandari, C. L. Corkhill, R. J. Hand and N. C. Hyatt, *MRS Adv.*, 2019, **4**, 1029–1043.

86 Y. Waseda, E. Matsubara and K. Shinoda, *X-Ray Diffraction Crystallography; Introduction, examples and solved problems*, Springer, Berlin, Heidelberg, 2011.

87 A. A. Bunaciu, E. G. Udriştioiu and H. Y. Aboul-Enein, *Crit. Rev. Anal. Chem.*, 2015, **45**, 289–299.

88 J. . Goldstein, D. E. Newbury, J. W. Colby, H. Yakowitz, E. Lifshin and J. R. Coleman, *Practical Scanning Electron Microscopy: Electron and Ion Microprobe Analysis*, New York, 1975.

89 G. S. Henderson, F. M. F. De Groot and B. J. A. Moulton, *Rev. Mineral. Geochem.*, 2014, **78**, 75–138.

90 M. Affatigato, *Modern Glass Characterization*, John Wiley & Sons Inc., Hoboken, 2015.

91 H. Asakura, S. Hosokawa, K. Teramura and T. Tanaka, *Chem. Rec.*, 2019, **19**, 1-13.

92 W. Błachucki, J. Czapla-Masztafiak, J. Sa and J. Szlachetko, *J. Anal. At. Spectrom.*, 2019, **34**, 1409-1415.

93 T. Regier, J. Paulsen, G. Wright, I. Coulthard, K. Tan, T. K. Sham and R. I. R. Blyth, *AIP Conf. Proc.*, 2007, **879**, 473–476.

94 P. Willmont, *Introduction to Synchrotron Radiation: Techniques and Applications*, John Wiley & Sons Ltd., Chirchester, 2011.

95 Y. He, Y. Lü and Q. Zhang, *J. Nucl. Mater.*, 2008, **376**, 201–206.

96 E. Malchukova, B. Boizot, D. Ghaleb and G. Petite, *J. Non. Cryst. Solids*, 2006, **352**, 297–303.

97 S. Guo-Malloy, P. F. McMillan and W. T. Petuskey, *J. Non. Cryst. Solids*, 2016, **451**, 77–83.

98 E. Drabarek, T. I. McLeod, J. V. Hanna, C. S. Griffith and V. Luca, *J. Nucl. Mater.*, 2009, **384**, 119–129.

99 R. Kijkowska, *J. Mater. Sci.*, 2003, **38**, 229–233.

100 W. Kraus and G. Nolze, *J. Appl. Crystallogr.*, 1996, **29**, 301–303.

101 S. M. Heald, D. L. Brewe, E. A. Stern, K. H. Kim, F. C. Brown, D. T. Jiang, E. D. Crozier and R. A. Gordon, *J. Synchrotron Radiat.*, 1999, **6**, 347–349.

102 A. C. Thompson, D. T. Attwood, E. M. Gullikson, M. R. Howells, J. B. Kortright, A. L. Robinson, J. H. Underwood, K.-J. Kim, J. Kirz, I. Lindau, P. Pianetta, H. Winick, G. P. Williams and J. H. Scofield, *X-ray data booklet*, University of California, Berkeley, CA, 3rd edn., 2009.

103 B. Ravel and M. Newville, *J. Synchrotron Radiat.*, 2005, **12**, 537–541.

104 D. F. Mullica, D. A. Grossie, W. O. Milligan, G. W. Beall and Boatner, *Inorganica Chim. Acta*, 1984, **95**, 231–236.

105 M. F. Zawrah and E. M. A. Hamzawy, *Ceram. Int.*, 2002, **28**, 123–130.

106 O. A. Alharbi, D. Y. Zaki and E. M. A. Hamzawy, *Silicon*, 2012, **4**, 281–287.

107 M. S. Al-Assiri and M. M. El-Desoky, *J. Mater. Sci. Mater. Electron.*, 2013, **24**, 784–792.

108 R. Widmer, F. Gfeller and T. Armbruster, *J. Am. Ceram. Soc.*, 2015, **98**, 3956–3965.

109 H. Asakura, T. Shishido, K. Teramura and T. Tanaka, *Inorg. Chem.*, 2014, **53**, 6048–6053.

110 A. J. Connelly, N. C. Hyatt, K. P. Travis, R. J. Hand, E. R. Maddrell and R. J. Short, *J. Non. Cryst. Solids*, 2011, **357**, 1647–1656.

111 K. Tanaka, Y. Takahashi and H. Shimizu, *Geochem. J.*, 2009, **43**, 143–149.

112 E. R. Aluri, L. M. Bachiu, A. P. Grosvenor, S. H. Forbes and J. E. Greedan, *Surf. Interface Anal.*, 2017, **49**, 1335–1344.

113 D. Cabaret, Y. Joly, H. Renevier and C. R. Natoli, *J. Synchrotron Radiat.*, 1999, **6**, 258–260.

114 F. Farges, G. E. Brown and J. Rehr, *Phys. Rev. B: Condens. Matter Mater. Phys.*, 1997, **56**, 1809–1819.

115 V. Kumar, Rupali, O. P. Pandey and K. Singh, *Int. J. Hydrogen Energy*, 2011, **36**, 14971–14976.

116 Allen Alper, *Phase Diagrams 6-V*, Academic Press, New York, 1978.

117 T. Charpentier, N. Ollier and H. Li, *J. Non. Cryst. Solids*, 2018, **492**, 115–125.

118 T. Schaller and J. F. Stebbins, *J. Phys. Chem. B*, 1998, **102**, 10690–10697.

119 V. Kumar, K. Singh and O. P. Pandey, Thapar University, 2010.

120 J. Ren and H. Eckert, *J. Phys. Chem. C*, 2014, **118**, 15386–15403.

121 M. Wang, J. Cheng, M. Li, F. He and W. Deng, *Solid State Sci.*, 2012, **14**, 1233–1237.

122 V. Kumar, O. P. Pandey and K. Singh, *Ceram. Int.*, 2010, **36**, 1621–1628.

123 J. Kruse, P. Leinweber, K. U. Eckhardt, F. Godlinski, Y. Hu and L. Zuin, *J. Synchrotron Radiat.*, 2009, **16**, 247–259.

124 L. A. J. Garvie and P. R. Buseck, *Am. Mineral.*, 1999, **84**, 946–964.

125 D. Li, M. Fleet, G. Bancroft, M. Kasrai and Y. Pan, *J. Non. Cryst. Solids*, 1995, **188**, 181–189.

126 C. Ritzberger, E. Apel, V. M. Rheinberger, M. Schweiger and W. Holand, *Phys. Chem. Glas: Eur. J. Glas. Sci. Technol. Part B*, 2013, **54**, 228–231.

127 V. Sandu, E. Cimpoiasu, A. Kuncser and M. S. Nicolescu, *J. Adv. Ceram.*, 2017, **6**, 251–261.

128 O. Bretcanu, S. Spriano, E. Verné, M. Cöisson, P. Tiberto and P. Allia, *Acta Biomater.*, 2005, **1**, 421–429.

129 R. C. Ewing, *Proc. Natl. Acad. Sci.*, 1999, **96**, 3432–3439.

130 T. Degen, M. Sadki, E. Bron, U. König and G. Nénert, *Powder Diffr.*, 2014, **29**, S13–S18.

131 T. Ungar, *Scr. Mater.*, 2004, **51**, 777–781.

132 T. Ungár, *Mater. Sci. Forum*, 2009, **278**–**281**, 151–157.

133 C. M. Harris and S. J. Skinner, *J. Solid State Chem.*, 2019, **271**, 135–143.

134 D. Bregiroux, F. Audubert, T. Charpentier, D. Sakellariou and D. Bernache-Assollant, *Solid State Sci.*, 2007, **9**, 432–439.

135 J.Kim and B. Ryu, *J. Ceram. Soc. Japan*, 2017, **125**, 118–121.

136 A. Kidari, J. Dussossoy, E. Brackx, D. Caurant, M. Magnin and I. Bardez-Giboire, *J. Am. Ceram. Soc.*, 2012, **95**, 2537–2544.

137 J. Chaboy, A. Marcelli and L. Bozukov, *J. Phys. Condens. Matter*, 1995, **7**, 8197–8210.

138 N. Smolentsev, A. A. Guda, O. V. Safonova, M. A. Soldatov, C. Paun, G. Smolentsev, J. A. Van Bokhoven and A. V. Soldatov, *J. Phys. Conf. Ser.*, 2013, **430**, 012062.

139 T. K. Sham, R. A. Gordon and S. M. Heald, *Phys. Rev. B*, 2005, **72**, 035113.

140 S. Yang, D. Wang, G. Liang, Y. M. Yiu, J. Wang, L. Liu, X. Sun and T. Sham, *Energy Environ. Sci.*, 2012, **5**, 7007.

141 S. O. Kucheyev, B. J. Clapsaddle, Y. M. Wang, T. Van Buuren and A. V. Hamza, *Phys. Rev. B.*, 2007, **76**, 235420.

142 I. G. Polyakova, *Phys. Chem. Glas.*, 2000, **41**, 247–258.

143 H. Dong, Y. Shuang, Q. Sun, Q. Ren and W. Ma, *Advanced Functional Materials*, ed. Y. Han, Springer Singapore, Singapore, 2018, pp. 643–649.

144 L. M. Delitsyn, V. A. Sinel'shchikov, V. M. Batenin, G. A. Sychev, T. I. Borodina and G. E. Val'yano, *Dokl. Chem.*, 2018, **483**, 323–327.

145 S. M. Salman, S. N. Salama and E. A. Mahdy, *Bol. la Soc. Esp. Ceram. y Vidr.*, 2019, **58**, 94–102.

146 A. M. Hu, K. M. Liang, F. Zhou, G. L. Wang and F. Peng, *Ceram. Int.*, 2005, **31**, 11–14.

147 M. Xia, X. Wu, Y. Zhong, Z. Zhou and W. Wong, *J. Mater. Chem. C*, 2019, **7**, 2385–2393.

148 X. Zhao, Y. Li, Y. Teng, L. Wu, P. Bi, X. Yang and L. Wan, *J. Eur. Ceram. Soc.*, 2019, **39**, 1555–1563.

149 H. Li, X. Liang, C. Wang, H. Yu, Z. Li and S. Yang, *J. Mol. Struct.*, 2014, **1076**, 592–599.

150 F. Benedetti, P. Luches, S. D'Addato, S. Valeri, V. Nicolini, A. Pedone, M. C. Menziani and G. Malavasi, *J. Am. Ceram. Soc.*, 2017, **100**, 5086–5095.

151 L. P. Santana and T. C. Cordeiro, *Proc. Int. Acad. Ecol. Environ. Sci.*, 2016, **6**, 38–43.

152 O. Bretcanu, E. Verné, M. Cöisson, P. Tiberto and P. Allia, *J. Magn. Magn. Mater.*, 2006, **305**, 529–533.

153 M. V. Ramana, *Wiley Interdiscip. Rev. Energy Environ.*, 2018, **7**, 1–12.

154 K. Popa, P. E. Raison, L. Martel, P. M. Martin, D. Prieur, P. L. Solari, D. Bouëxière, R. J. M. Konings and J. Somers, *J. Solid State Chem.*, 2015, **230**, 169–174.

155 B. C. Childs, F. Poineau, K. R. Czerwinski and A. P. Sattelberger, *J. Radioanal. Nucl. Chem.*, 2015, **306**, 417–421.

156 T. Alizadeh and F. Soleimani, *J. Non. Cryst. Solids*, 2019, **520**, 119465.

Appendix A

Supporting Information for Chapter 2

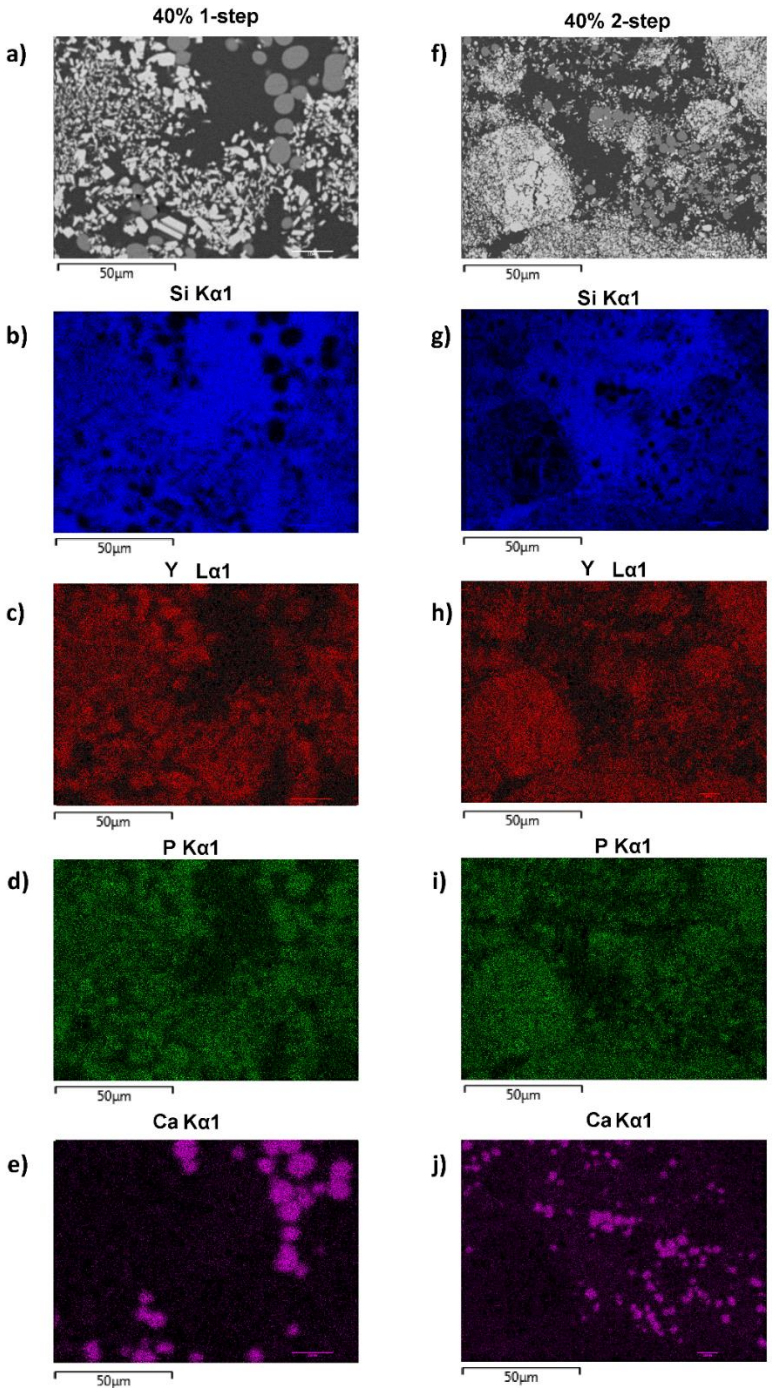

Figure A-1: (a) Backscattered electron image of 40 wt% ceramic YPO_4-BG composite synthesized by the one-step method, (b) Si EDX map of composite made by the one-step method, (c) Y EDX map of composite made by the one-step method (d) P EDX map of composite made by the one-step method, (e) Ca EDX map of composite made by the one-step method, (f) backscattered electron image of 40 wt% ceramic YPO_4-BG composite synthesized by the two-step method, (g) Si EDX map of composite made by the two-step method, (h) Y EDX map of composite made by the two-step method (i) P EDX map of composite made by the two-step method, (j) Ca EDX map of composite made by the two-step method.

Appendix B

Supporting Information for Chapter 3

Table B-1: Lattice Constants determined by powder XRD of $LaPO_4$ in $LaPO_4$-BG and pure $LaPO_4$ materials.

Composition	Annealing Temperature (ºC)	a (Å)	b (Å)	c (Å)	β (º)
40 wt% $LaPO_4$-BG	1100	6.840(1)	7.075(1)	6.512(1)	103.283(5)
20 wt% $LaPO_4$-BG	1100	6.840(1)	7.076(1)	6.512(1)	103.280(1)
40 wt% $LaPO_4$-BG	900	6.838(1)	7.072(1)	6.511(1)	103.307(1)
40 wt% $LaPO_4$-BG	800	6.840(1)	7.072(1)	6.513(1)	103.303(1)
40 wt% $LaPO_4$-BG	700	6.834(1)	7.052(1)	6.507(2)	103.288(4)
20 wt% $LaPO_4$-BG	700	6.835(1)	7.054(1)	6.507(1)	103.321(1)
$LaPO_4$	1100	6.839(1)	7.072(4)	6.518(1)	103.31(4)
$LaPO_4$	700	6.842(1)	7.071(3)	6.514(3)	103.34(3)

Table B-2: Calculated crystallite size and strain determined from powder XRD.

Peak position (2θ)	Crystallite Size only (nm)	Micro Strain only (%)
40 wt% $LaPO_4$-BG annealed at 700 ºC		
21.15	27	0.86
30.89	28	0.62
34.25	34	0.48
47.54	29	0.37
51.44	29	0.39
20 wt% $LaPO_4$-BG annealed at 700 ºC		
21.16	35	0.77
30.90	28	0.62
34.25	31	0.52
47.54	37	0.33
51.44	33	0.33

Table B-3: Phase analysis determined by powder XRD of $LaPO_4$-BG composite materials in wt%.

Composition	Annealing Temperature (ºC)	$LaPO_4$	Quartz
40 wt% LaPO4-BG	700	84(1)%	16(1)%
20 wt% LaPO4-BG	700	85(1)%	15(1)%

Table B-4: Lattice Constants determined by powder XRD for $CePO_4$, CeO_2, and nagelschmidtite in $CePO_4$-BG and pure $CePO_4$ materials synthesized using either a Ce^{3+} or Ce^{4+} precursor.

Composition	**Annealing Temperature (ºC)**	**$CePO_4$**				**CeO_2**
		a (Å)	**b (Å)**	**c (Å)**	**β (Å)**	**a (Å)**
40 wt% $CePO_4$-BG [Ce(III)]	1100	6.795(1)	7.020(1)	6.470(1)	103.472(1)	N/A
20 wt% $CePO_4$ -BG [Ce(III)]	1100	6.795(1)	7.018(1)	6.470(1)	103.477(3)	N/A
40 wt% $CePO_4$-BG [Ce(III)]	1000	6.767(5)	7.017(5)	6.472(5)	103.497(7)	5.415(2)
40 wt% $CePO_4$ -BG [Ce(III)]	900	6.797(1)	7.017(1)	6.472(1)	103.492(3)	5.409(1)
40 wt% $CePO_4$-BG [Ce(III)]	800	6.798(2)	7.019(3)	6.472(1)	103.487(7)	5.412(1)
40 wt% $CePO_4$ -BG [Ce(III)]	700	6.790(1)	7.005(1)	6.464(1)	103.472(1)	5.409(1)
20 wt% $CePO_4$-BG [Ce(III)]	700	N/A	N/A	N/A	N/A	5.409(1)
40 wt% $CePO_4$ -BG [Ce(IV)]	1100	6.795(1)	7.018(1)	6.470(1)	103.484(1)	N/A
20 wt% CePO4-BG [Ce(IV)]	1100	6.794(1)	7.019(1)	6.470(1)	103.477(1)	N/A
40 wt% $CePO_4$ -BG [Ce(IV)]	1000	6.794(1)	7.019(1)	6.470(1)	103.477(1)	5.411(1)
40 wt% $CePO_4$-BG [Ce(IV)]	900	6.794(1)	7.019(4)	6.470(1)	103.477(3)	5.408(2)
40 wt% $CePO_4$ -BG [Ce(IV)]	800	6.794(1)	7.019(2)	6.470(1)	103.479(1)	5.409(2)
40 wt% $CePO_4$-BG [Ce(IV)]	700	6.794(3)	7.011(1)	6.469(2)	103.47(2)	5.410(3)
20 wt% $CePO_4$ -BG [Ce(IV)]	700	N/A	N/A	N/A	N/A	5.408(1)

Table B-5: Phase analysis determined by powder XRD of $CePO_4$-BG [Ce(III)] and $CePO_4$-BG [Ce(IV)] composite materials in wt%.

Composition	Annealing Temperature (ºC)	$CePO_4$	CeO_2	$Na_3Ce(PO_4)_2$	Nagelschmidtite	Tridymite	Quartz	Cristobalite
40 wt% CePO4-BG [Ce(III)]	1100	93(3)%	0%	0%	7(3)%	0%	0%	0%
20 wt% CePO4-BG [Ce(III)]	1100	73(2)%	0%	0%	27(2)%	0%	0%	0%
40 wt% CePO4-BG [Ce(III)]	1000	69(2)%	8(1)%	0%	14(5)%	9(4)%	0%	0%
40 wt% CePO4-BG [Ce(III)]	900	55(5)%	14(1)%	0%	13(3)%	13(3)%	5(2)%	0%
40 wt% CePO4-BG [Ce(III)]	800	37(1)%	12(1)%	0%	15(2)%	0%	36(1)%	0%
40 wt% CePO4-BG [Ce(III)]	700	47(2)%	14(1)%	0%	12(2)%	0%	27(2)%	0%
20 wt% CePO4-BG [Ce(III)]	700	0%	22(1)%	4(2)%	25(1)%	0%	47(3)%	2(1)%
40 wt% CePO4-BG [Ce(IV)]	1100	95(2)%	0%	0%	5(2)%	0%	0%	0%
20 wt% CePO4-BG [Ce(IV)]	1100	86(5)%	0%	0%	14(5)%	0%	0%	0%
40 wt% CePO4-BG [Ce(IV)]	1000	63(1)%	15(1)%	0%	22(1)%	0%	0%	0%
40 wt% CePO4-BG [Ce(IV)]	900	42(4)%	27(2)%	0%	12(5)%	19(1)%	0%	0%
40 wt% CePO4-BG [Ce(IV)]	800	38(3)%	19(1)%	0%	24(7)%	0%	18(3)%	0%
40 wt% CePO4-BG [Ce(IV)]	700	33(1)%	15(1)%	5(2)%	16(7)%	0%	31(4)%	0%
20 wt% CePO4-BG [Ce(IV)]	700	0%	23(1)%	18(2)%	14(4)%	0%	45(7)%	0%

Table B-6: Phase analysis determined by powder XRD of $CePO_4$-BG [Ce(III)] and $CePO_4$-BG [Ce(IV)] composite materials in mol%.

Composition	Annealing Temperature (ºC)	$CePO_4$	CeO_2	$Na_3Ce(PO_4)_2$	Nagelschmidtite	Tridymite	Quartz	Cristobalite
40 wt% CePO4-BG [Ce(III)]	1100	97(3)%	0%	0%	3(3)%	0%	0%	0%
20 wt% CePO4-BG [Ce(III)]	1100	88(2)%	0%	0%	12(2)%	0%	0%	0%
40 wt% CePO4-BG [Ce(III)]	1000	57(2)%	9%	0%	4(5)%	29(4)%	0%	0%
40 wt% CePO4-BG [Ce(III)]	900	37(5)%	13(1)%	0%	3(3)%	34(3)%	13(2)%	0%
40 wt% CePO4-BG [Ce(III)]	800	18(1)%	8(1)%	0%	3(2)%	0%	71(1)%	0%
40 wt% CePO4-BG [Ce(III)]	700	27(2)%	10(1)%	0%	3(2)%	0%	60(2)%	0%
20 wt% CePO4-BG [Ce(III)]	700	0%	13(1)%	1(2)%	4(1)%	0%	79(3)%	3(1)%
40 wt% CePO4-BG [Ce(IV)]	1100	98(2)%	0%	0%	2(2)%	0%	0%	0%
20 wt% CePO4-BG [Ce(IV)]	1100	94(5)%	0%	0%	6(5)%	0%	0%	0%
40 wt% CePO4-BG [Ce(IV)]	1000	69(1)%	22(1)%	0%	9(1)%	0%	0%	0%
40 wt% CePO4-BG [Ce(IV)]	900	27(4)%	23(2)%	0%	3(5)%	47(1)%	0%	0%
40 wt% CePO4-BG [Ce(IV)]	800	27(3)%	18(1)%	0%	6(7)%	0%	49(3)%	0%
40 wt% CePO4-BG [Ce(IV)]	700	18(1)%	11(1)%	2(2)%	3(7)%	0%	66(3)%	0%
20 wt% CePO4-BG [Ce(IV)]	700	0%	14(1)%	6(2)%	2(4)%	0%	78(4)%	0%

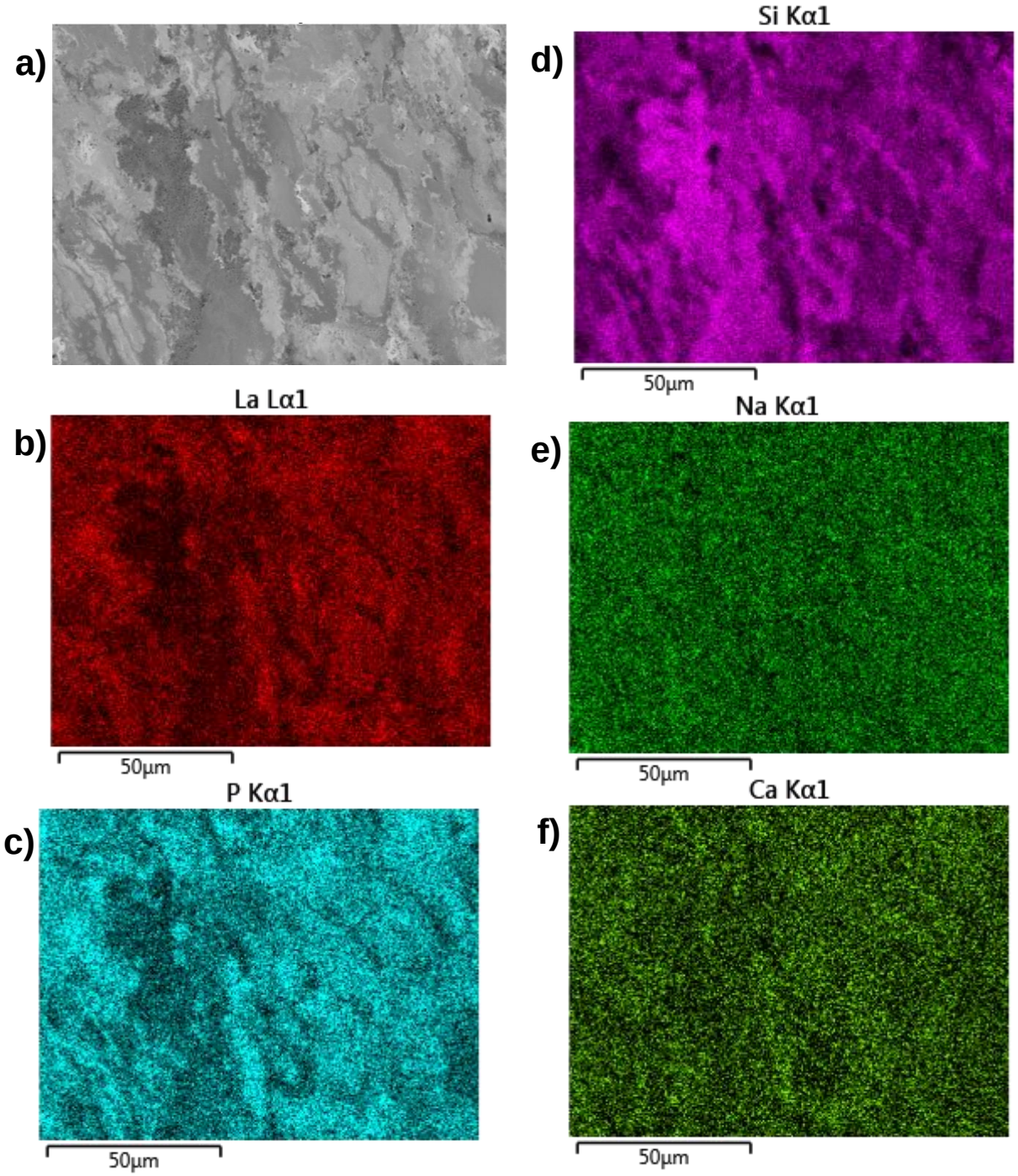

Figure B-1: a) SEM image of 40 wt% $LaPO_4$-BG composite material annealed at 700 ^oC, EDX maps of b) La, c) P, d) Si, e) Na, and f) Ca.

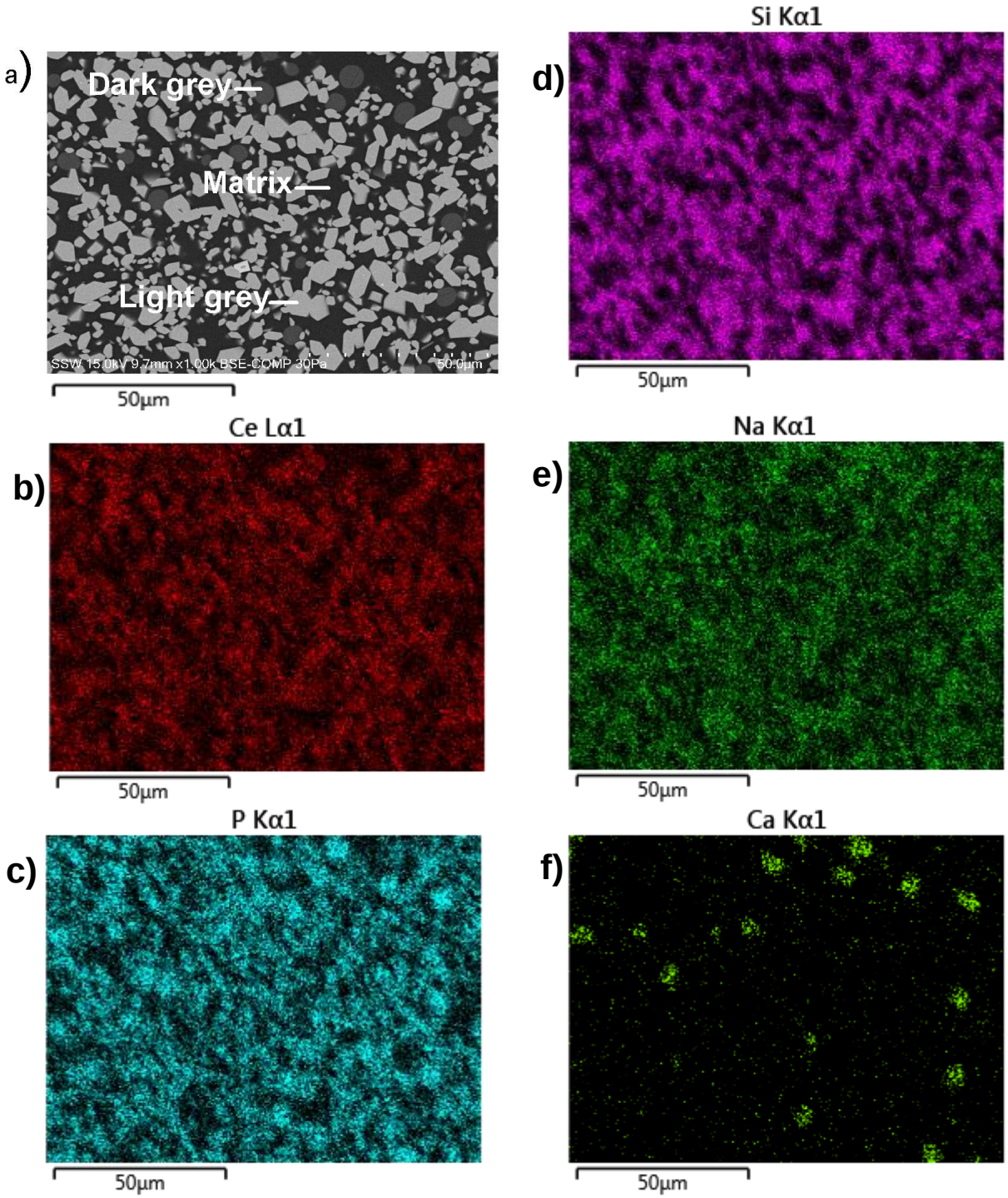

Figure B-2: SEM image of 40 wt% $CePO_4$-BG composite material synthesized with a Ce^{3+} precursor and annealed at 1100 ºC, EDX maps of b) Ce, c) P, d) Si, e) Na, and f) Ca.

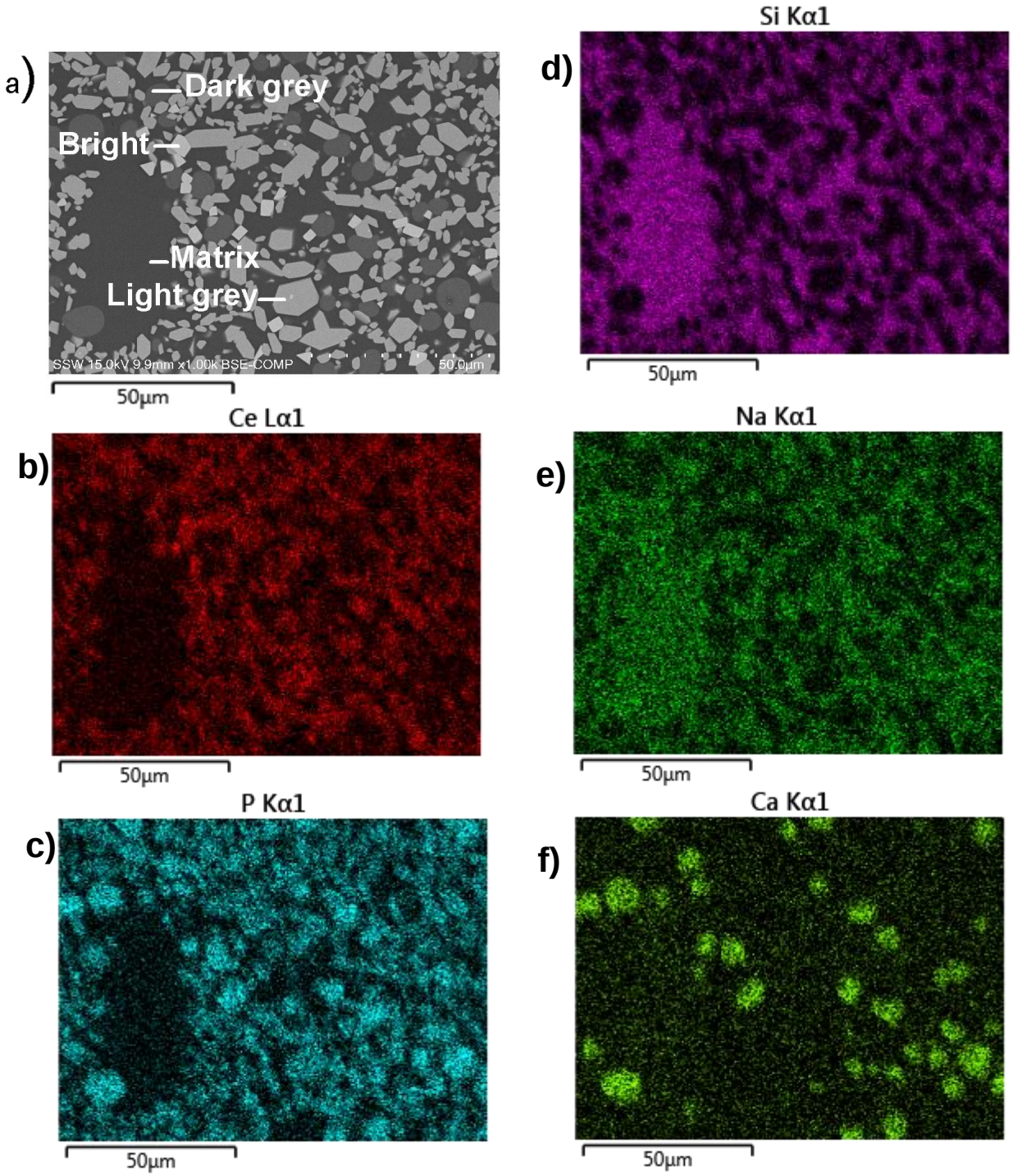

Figure B-3: SEM image of 40 wt% $CePO_4$-BG composite material synthesized with a Ce^{4+} precursor and annealed at 1100 ^oC, EDX maps of b) Ce, c) P, d) Si, e) Na, and f) Ca.

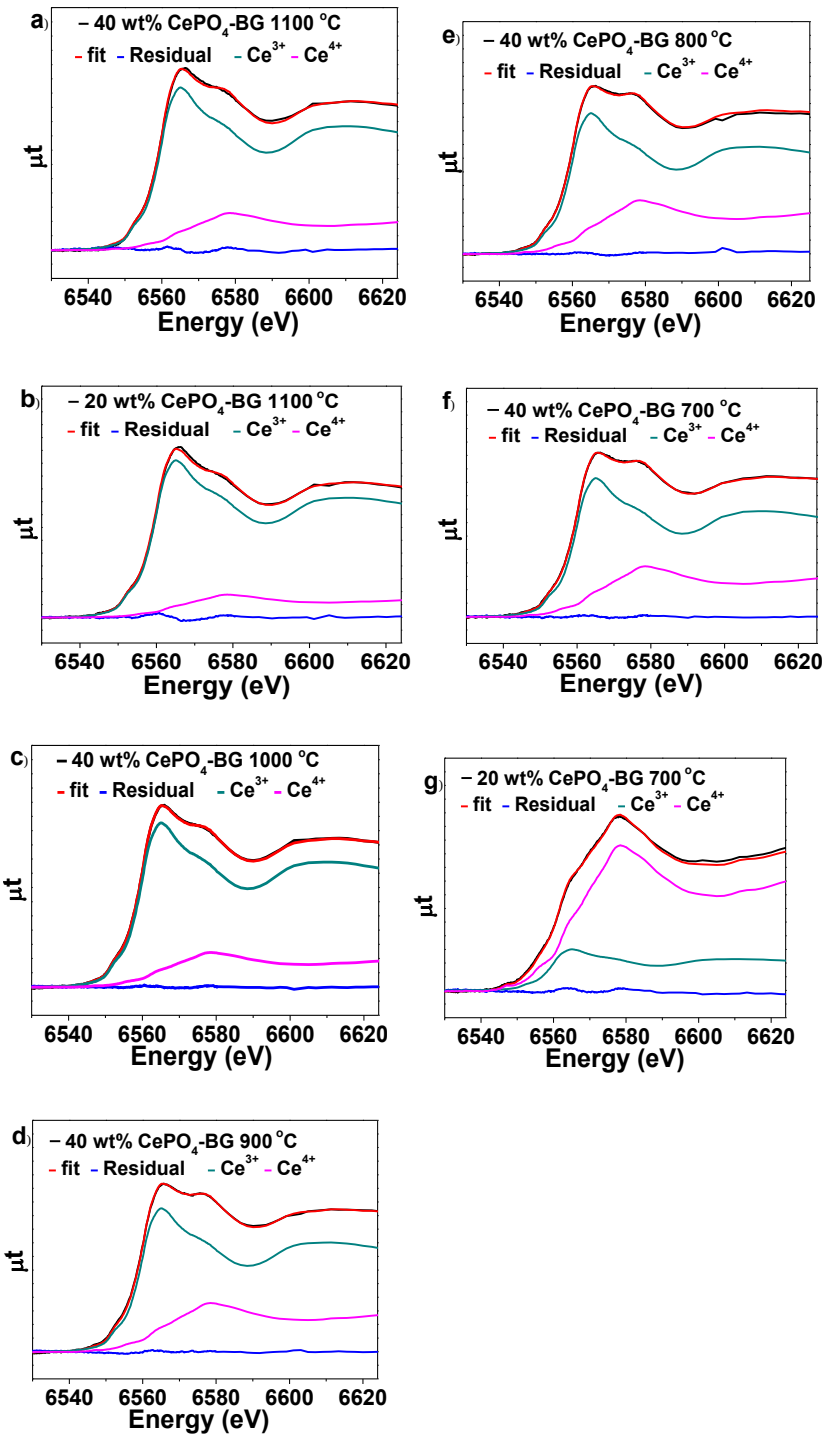

Figure B-4: Linear combination fit results of Ce L_1-edge XANES spectra from a)40 wt% $CePO_4$-BG annealed at 1100 °C, b) 20 wt% $CePO_4$-BG annealed at 1100 °C, c) 40 wt% $CePO_4$-BG annealed at 1000 °C, d) 40 wt% $CePO_4$-BG annealed at 900 °C, e) 40 wt% $CePO_4$-BG annealed at 800 °C, f) 40 wt% $CePO_4$-BG annealed at 700 °C, and g) 20 wt% $CePO_4$-BG annealed at 700 °C. All materials were synthesized using a Ce^{3+} precursor.

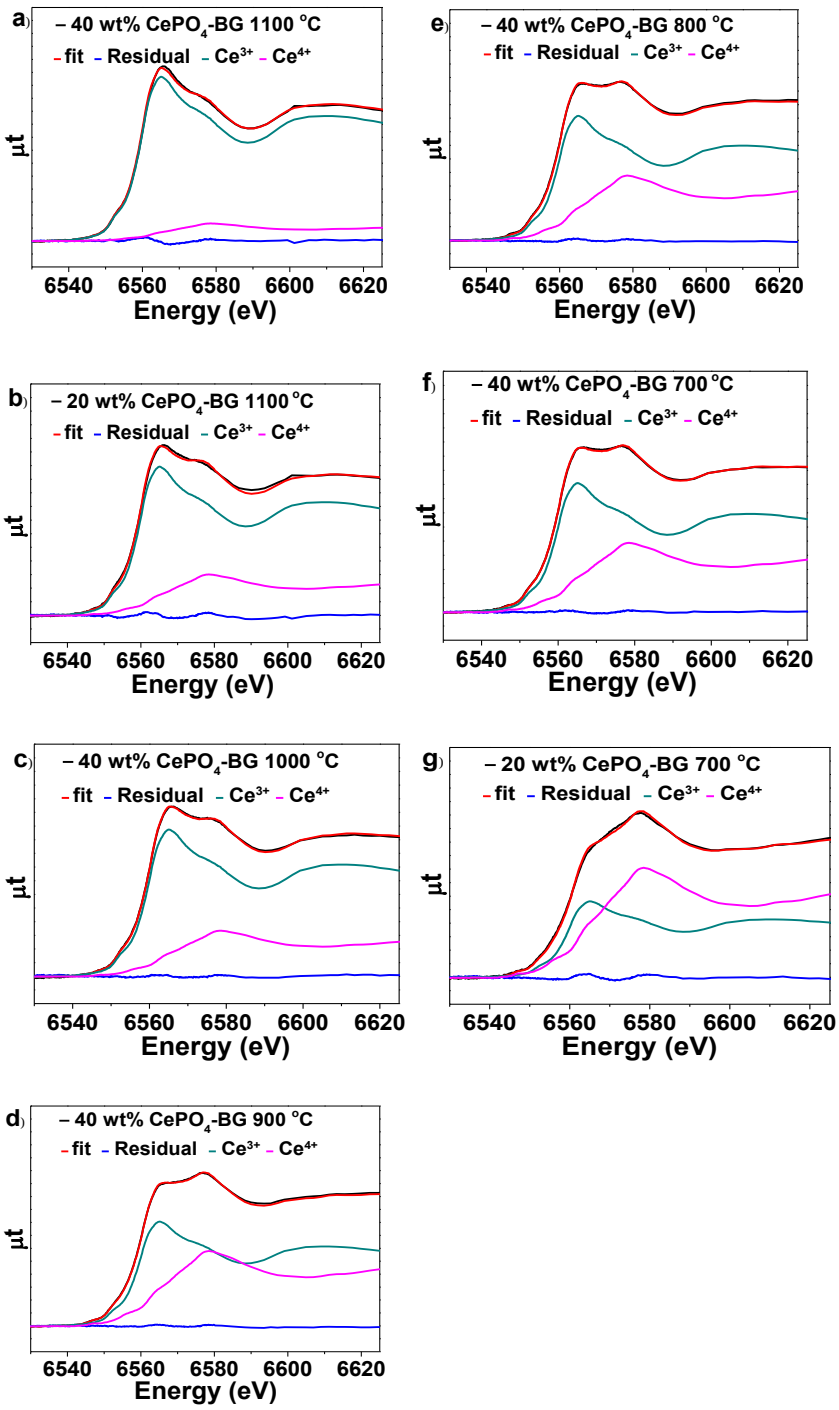

Figure B-5: Linear combination fit results of Ce L_1-edge XANES spectra from a)40 wt% $CePO_4$-BG annealed at 1100 °C, b) 20 wt% $CePO_4$-BG annealed at 1100 °C, c) 40 wt% $CePO_4$-BG annealed at 1000 °C, d) 40 wt% $CePO_4$-BG annealed at 900 °C, e) 40 wt% $CePO_4$-BG annealed at 800 °C, f) 40 wt% $CePO_4$-BG annealed at 700 °C, g) 20 wt% $CePO_4$-BG annealed at 700 °C. All materials were synthesized using a Ce^{4+} precursor.

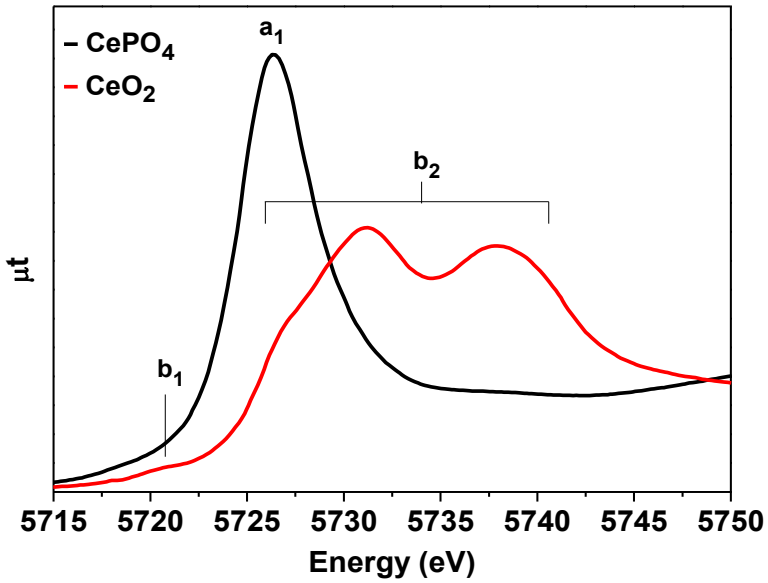

Figure B-6: Ce L_3-edge XANES spectra from$CePO_4$ and CeO_2.

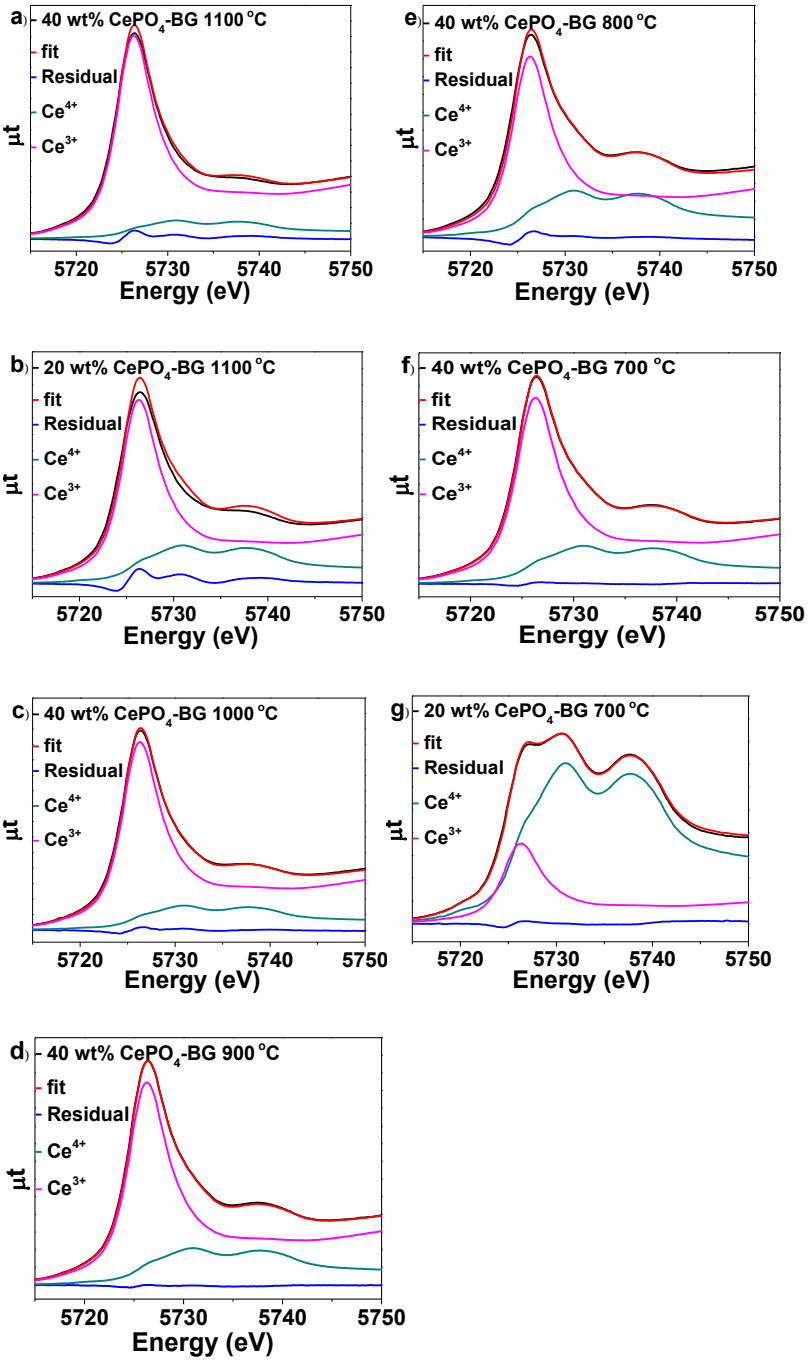

Figure B-7: Linear combination fit results of Ce L_3-edge XANES spectra from a)40 wt% $CePO_4$-BG annealed at 1100 °C, b) 20 wt% $CePO_4$-BG annealed at 1100 °C, c) 40 wt% $CePO_4$-BG annealed at 1000 °C, d) 40 wt% $CePO_4$-BG annealed at 900 °C, e) 40 wt% $CePO_4$-BG annealed at 800 °C, f) 40 wt% $CePO_4$-BG annealed at 700 °C, and g) 20 wt% $CePO_4$-BG annealed at 700 °C. All materials were synthesized using a Ce^{3+} precursor.

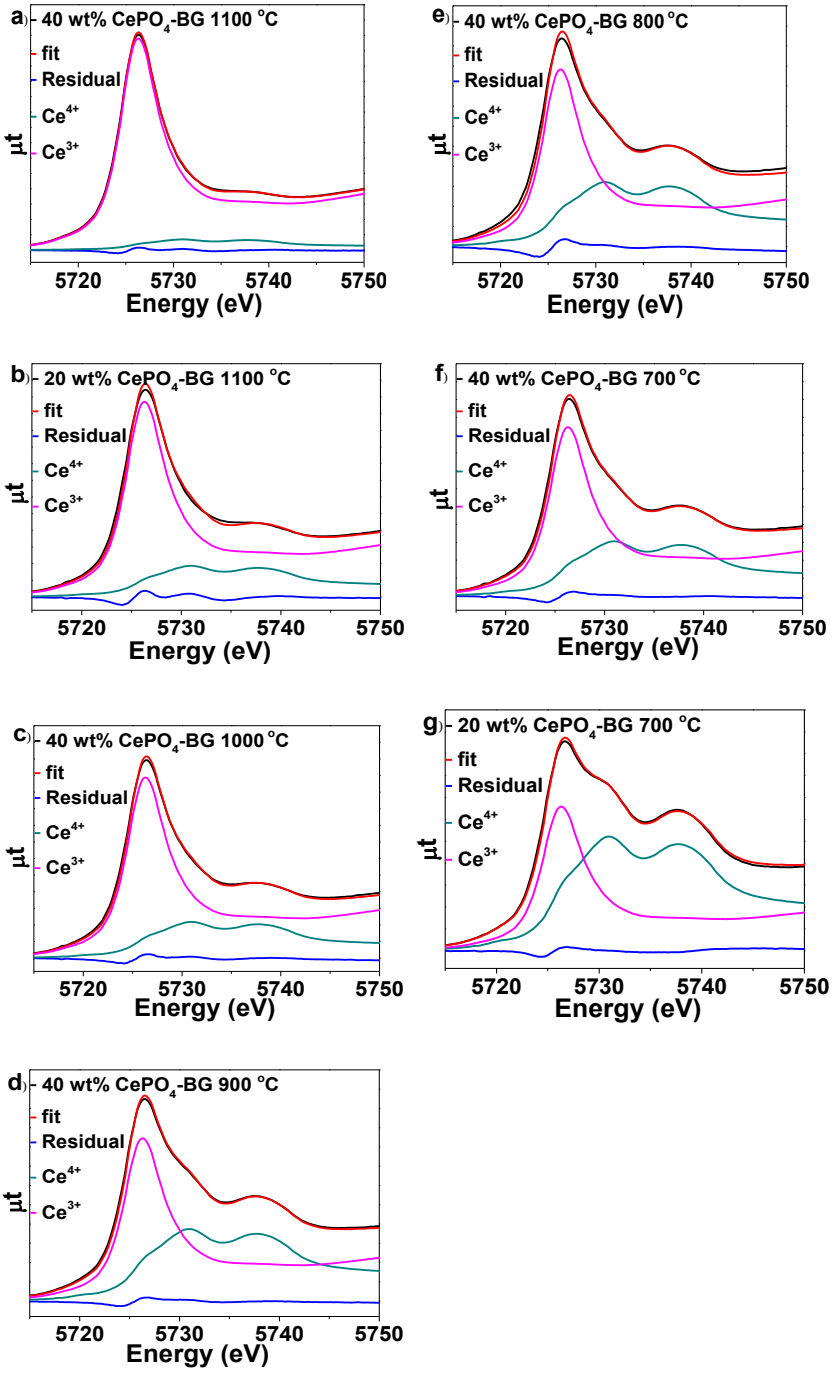

Figure B-8: Linear combination fit results of Ce L_3-edge XANES spectra from a)40 wt% $CePO_4$-BG annealed at 1100 °C, b) 20 wt% $CePO_4$-BG annealed at 1100 °C, c) 40 wt% $CePO_4$-BG annealed at 1000 °C, d) 40 wt% $CePO_4$-BG annealed at 900 °C, e) 40 wt% $CePO_4$-BG annealed at 800 °C, f) 40 wt% $CePO_4$-BG annealed at 700 °C, g) 20 wt% $CePO_4$-BG annealed at 700 °C. All materials were synthesized using a Ce^{4+} precursor.

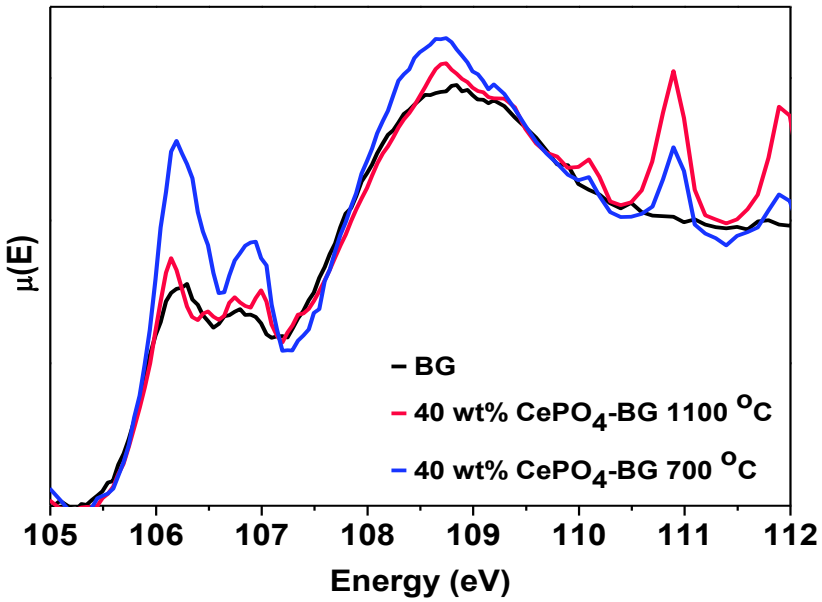

Figure B-9: Si $L_{2,3}$-edge spectra from borosilicate glass as well as 40 wt% $CePO_4$-BG [Ce(III)] annealed at 1100 and 700 °C.